IMPLEMENTATION OF A FAST SIMULATION TOOL FOR THE ANALYSIS OF CONTRAST MECHANISMS IN HMMDI AND ENHANCEMENT OF THE SNR IN THE EXPERIMENTAL SET-UP

A THESIS SUBMITTED TO
THE GRADUATE SCHOOL OF NATURAL AND APPLIED SCIENCES
OF
MIDDLE EAST TECHNICAL UNIVERSITY

BY

ÜMİT İRGİN

IN PARTIAL FULFILLMENT OF THE REQUIREMENTS
FOR
THE DEGREE OF DOCTOR OF PHILOSOPHY
IN
ELECTRICAL AND ELECTRONIC ENGINEERING

SEPTEMBER 2021

Approval of the thesis:

IMPLEMENTATION OF A FAST SIMULATION TOOL FOR THE ANALYSIS OF CONTRAST MECHANISMS IN HMMDI AND ENHANCEMENT OF THE SNR IN THE EXPERIMENTAL SET-UP

submitted by **ÜMİT İRGİN** in partial fulfillment of the requirements for the degree of **Doctor of Philosophy** i**n Electrical and Electronic Engineering, Middle East Technical University** by,

Prof. Dr. Halil Kalıpçılar
Dean, Graduate School of **Natural and Applied Sciences**

Prof. Dr. İlkay Ulusoy
Head of the Department, **Electrical and Electronics Eng.,**

Prof. Dr. Nevzat Güneri Gençer
Supervisor, **Electrical and Electronics Eng., METU**

Dr. Can Barış Top
Co-Supervisor, **ASELSAN Research Center, ASELSAN A.Ş.**

Examining Committee Members:

Prof. Dr. Sencer Koç
Electrical and Electronics Eng., METU

Prof. Dr. Nevzat Güneri Gençer
Electrical and Electronics Eng., METU

Prof. Dr. Ergin Atalar
Electrical and Electronics Eng., Bilkent University

Assoc. Prof. Dr. Yeşim Serinağaoğlu Doğrusöz
Electrical and Electronics Eng., METU

Prof. Dr. Vakur B. Ertürk
Electrical and Electronics Eng., Bilkent University

Date: 06.09.2021

I hereby declare that all information in this document has been obtained and presented in accordance with academic rules and ethical conduct. I also declare that, as required by these rules and conduct, I have fully cited and referenced all material and results that are not original to this work.

Name Last name : Ümit İrgin

Signature :

ABSTRACT

IMPLEMENTATION OF A FAST SIMULATION TOOL FOR THE ANALYSIS OF CONTRAST MECHANISMS IN HMMDI AND ENHANCEMENT OF THE SNR IN THE EXPERIMENTAL SET-UP

İrgin, Ümit
Doctor of Philosophy, Electrical and Electronic Engineering
Supervisor : Prof. Dr. Nevzat Güneri Gençer
Co-Supervisor: Dr. Can Barış Top

September 2021, 123 pages

Clinical method for breast tumor detection is Mammography (X-rays), which have limitations and may yield inaccurate results. Alternative novel techniques are required to characterize the breast tissues and extract accurate information for identification of malignancies in the tissue. Harmonic Motion Microwave Doppler Imaging (HMMDI), which enhances hybridizing microwave signals and ultrasound techniques, has been recently proposed for detection of tumors in the tissue. In HMMDI method, the data is a combination of dielectric, elastic and acoustic properties of the focused volume. The contrast levels in the dielectric and elastic properties of the malignant and normal breast tissues enable the detection of the tumorous tissues. However, the level of the received Doppler signal is not a linear function of the contrast levels, especially for the mechanical properties.

In this study, the effect of contrast in the dielectric and elastic properties between a 3 mm sized inclusion and the surrounding breast as functions of position of the inclusion and vibration frequency (in 10 Hz to 95 Hz range) is analyzed. To solve the forward problem of HMMDI, a Discrete Dipole Approximation (DDA) based simulation method is developed. DDA solver decreased the simulation time by a factor of 146 compared to the Finite Difference Time Domain method. Increasing the dielectric constant by a factor of 3.2 increased the received signal by 5.1 dB in the whole vibration frequency range. On the other hand, increasing the Young’s modulus by a factor of 3.3 resulted in 1 dB and 2.5 dB decrease in Doppler signal level for vibration frequencies of 40 Hz and 95 Hz, respectively. When the focus was moved away from the inclusion, dielectric and\or elastic contrast variation did not change the relative received signal level significantly. The simulation results showed that the received signal level behavior as a function of vibration frequency can provide useful information on the elastic properties of the inclusion.

In the HMMDI experimental set-up there are two main limitations on the sensitivity of the method: i) the phase noise of the transmitter source and ii) the coupling between transmitting and receiving antennas. In this study, a signal cancellation circuit is designed to suppress the coupled signal and to increase the signal to noise ratio (SNR) of the Doppler component. The transmit signal coupled to the receiving antenna was decreased more than 30 dB, enhancing the SNR about 17 dB. Hard inclusions inside a fat phantom were resolved using the HMMDI system with the proposed signal cancellation circuit.

Keywords: Breast Cancer Imaging, Dielectric Properties of Breast, Elastic Properties of Tissues, Discrete Dipole Approximation

ÖZ

HHMDG KONTRAST MEKANİZMALARININ ANALİZİ İÇİN HIZLI BİR SİMÜLASYON ARACININ GERÇEKLEŞTİRİLMESİ VE DENEYSEL ORTAMDA SGO İYİLEŞTİRİLMESİ

İrgin, Ümit
Doktora, Elektrik ve Elektronik Mühendisliği
Tez Yöneticisi: Prof. Dr. Nevzat Güneri Gençer
Ortak Tez Yöneticisi: Dr. Can Barış Top

Eylül 2021, 123 sayfa

Meme tümörlerinin teşhisinde klinik olarak kullanılan (X-ray) Mamografinin bazı limitleri bulunmakta ve yanlış sonuçlar verebilmektedir. Meme dokularını karakterize etmek ve dokudaki malignitelerin tanımlanması için doğru bilgiler elde etmek için, literatürde alternatif yeni teknikler gerekmektedir. Mikrodalga sinyallerini ve ultrason tekniklerini hibridize eden Harmonik Hareketli Mikrodalga Doppler Görüntüleme (HHMDG), dokudaki tümörlerin tespiti için yakın zamanda önerilmiştir. HHMDG yönteminde alınan işaretler, odaklanmış hacmin dielektrik, elastik ve akustik özelliklerinin bir kombinasyonudur. Malign ve normal meme dokularının dielektrik ve elastik özelliklerindeki kontrast seviyeleri, tümörlü dokuların saptanmasını sağlar. Ancak alınan Doppler sinyalinin seviyesi, özellikle mekanik özellikler için kontrast seviyelerinin doğrusal bir fonksiyonu değildir.

Bu çalışmada, 3 mm büyüklüğündeki bir inklüzyon ile inklüzyonu çevreleyen meme arasındaki dielektrik ve elastik özelliklerdeki kontrastın, inklüzyon pozisyonunun etkisi, 10 Hz ila 95 Hz aralığında titreşim frekansı için analiz edilmiştir. HHMDG'nin ileri problemini çözmek için, Ayrık Dipol Yaklaşımı (ADY) tabanlı bir simülasyon yöntemi geliştirilmiştir. ADY çözücüsü, Sonlu Fark Zaman Etki Alanı yöntemine kıyasla simülasyon süresini 146 kat azaltmıştır. Dielektrik sabitinin 3,2 kat artırılması durumunda, alınan sinyali tüm titreşim frekans aralığında 5,1 dB artırmıştır. Öte yandan, elastik parametresi olan Young modülünün 3,3 kat arttırılması, sırasıyla 40 Hz ve 95 Hz titreşim frekansları için Doppler sinyal seviyesinde 1 dB ve 2,5 dB azalma ile sonuçlanmıştır. İnklüzyonun pozisyonu ultrason probunun odağından uzaklaştırıldığında, dielektrik ve/veya elastik kontrast değişimi, alınan sinyal seviyesini önemli ölçüde değiştirmemiştir. Simülasyon sonuçları, titreşim frekansının bir fonksiyonu olarak alınan sinyal seviyesi davranışının, inklüzyonun elastik özellikleri hakkında faydalı bilgiler sağlayabileceğini göstermiştir.

HHMDG deney düzeneğinde, yöntemin duyarlılığı üzerinde iki ana sınırlama vardır: i) verici kaynağının faz gürültüsü ve ii) verici ve alıcı antenler arasındaki bağlantı. Bu çalışmada, gönderme anteninden iletilen sinyalin bağlaşımını bastırmak ve Doppler bileşeninin sinyal-gürültü oranını (SGO) artırmak için bir sinyal yok edici devre tasarlanmıştır. Alıcı antene bağlanan iletim sinyali 30 dB'den fazla azaltılarak SNR yaklaşık 17 dB artmıştır. Bir yağ fantomunun içindeki sert inklüzyonlar, önerilen sinyal iptal devresinin HHMDG sistemine uyarlanması ile görüntülenmiştir.

Anahtar Kelimeler: Meme Kanseri Görüntüleme, Meme Dielektrik Özellikleri, Dokuların Elastik Özellikleri, Ayrık Dipol Yaklaşımı

to Zeynep

ACKNOWLEDGMENTS

I would like to thank my thesis advisor Prof. Dr. Nevzat Güneri GENÇER for his valuable guidance, unfailing support and patience during my studies. I have availed myself especially of his constructive comments and suggestions throughout my thesis. I felt privileged to be a member of the METU BERG group, since Prof. Dr. GENÇER provided us a well-equipped research infrastructure and created a trustworthy family environment that any researcher would desire.

My sincere thanks must also go to Dr. Can Barış TOP, my co-advisor, for his supports and aids at any time. I am forever indebted to his inspiring discussions, suggestions, helps and friendship without which I would not be able to finalize my thesis. With his sincerity and endless support, I managed to complete many difficult steps. He will always be my role model in my future life.

I would like to express my gratitude to the members of my Thesis Monitoring Committee, Prof. Dr. Sencer KOÇ and Prof. Dr. Ergin ATALAR. They generously gave their time to offer me valuable suggestions and comments towards improving my researches.

I would like to show an inexpressible gratitude my dear friend and team mate, Damla ALPTEKİN SOYDAN, who always befriended me even in most despaired times. I really enjoyed working with her in the same project, I learnt very much from her and that gave me new inspirations in my studies.

I am also grateful to Fikret TATAR, for lending me his invaluable experiences in computational studies. I benefited from his deep knowledge on fast computational schemes that eased my computational studies.

I would like to dedicate my profound thanks to my friends that I had chance to work together in METU BERG group, Mahsa KEYKHALI, Gökhan CANSIZ, Gamze

ONUKER, Balkar ERDOĞAN, Reyhan ZENGİN and Azadeh KAMALI TAFRESHI.

I would also like to thank to Dr. Volkan AÇIKEL and Asst. Dr. Gökhan GÜVENSEN for their friendship and support during my studies.

I am grateful to ASELSAN A.Ş. for all facilities it offered me during my thesis studies.

This study was made possible by the grant of The Scientific and Technological Research Council of Turkey (TÜBİTAK), through the main project numbers 114E036 and 117E246. I would like to personally thank TÜBİTAK for its support on my research, as well as its continuous support for all researchers in Turkey.

My endless thanks goes to my biggest supporter, my love, Zeynep. She is my wonderful chance in my life. I would like to thank with the sincerest feelings to her endless love and support that has always inspired me.

Last but not least, my special thanks are for my parents, my sister Müjde and my brother Ufuk. They have always been my supporter throughout of my life. I am proud of all of them.

TABLE OF CONTENTS

ABSTRACT v

ÖZ vii

ACKNOWLEDGMENTS x

TABLE OF CONTENTS xii

LIST OF TABLES xv

LIST OF FIGURES xvi

LIST OF ABBREVIATIONS xxiv

1 INTRODUCTION 1

- 1.1 Motivation of the Thesis 8
- 1.2 Overview of the Thesis 11

2 HARMONIC MOTION MICROWAVE DOPPLER IMAGING (HMMDI): THEORY, EXPERIMENTAL SET-UP AND SIMULATION METHOD 13

- 2.1 Introduction 13
- 2.2 Experimental Set-Up for HMMDI 17
- 2.3 Simulation Method for Solving the Forward Problem of HMMDI 18
  - 2.3.1 Acoustic and Mechanical Simulation Methods 20
  - 2.3.2 Electromagnetic Simulation Method 22
- 2.4 Resolution Analysis of HMMDI 26
  - 2.4.1 The Simulation Model 28
  - 2.4.2 The Simulation Results 30

2.5 Conclusion 35

3 IMPLEMENTATION OF A FAST SIMULATION SCHEME FOR THE FORWARD EM SIMULATION OF HMMDI 37

3.1 Introduction 37

3.2 DDA Based Simulation Method (3-Stage)... 38

3.3 Alternative DDA Based Simulation Method (1-Stage)........................... 43

3.3.1 Semi-Analytical Solution for the Computation of Incident Electrical Field 43

3.3.2 Adding Phase Terms to Polarization Matrix.................................... 46

3.4 Verification of the Proposed Simulation Method.................................... 46

3.4.1 Acoustic and Mechanical Simulations... 47

3.4.1 Electromagnetic Simulations 47

3.4.1 Simulation Results 52

3.5 2D HMMDI Scan Simulations With The 1-stage DDA Based Method .. 55

3.6 3D HMMDI Scan Simulations For Two Different Tumor Sizes With The 3-stage DDA Based Method 59

3.7 Conclusion... 70

4 THE EFFECT OF CONTRASTS IN ELECTRICAL AND MECHANICAL PROPERTIES BETWEEN BREAST TISSUES ON HMMDI..............................71

4.1 Introduction 71

4.2 The Simulation Model... 72

4.3 The Simulation Results 73

4.4 Conclusion... 80

5 ENCHANCING RECEIVED DOPPLER SIGNAL LEVELS IN HMMDI VIA MAIN SIGNAL CANCELLATION CIRCUIT 85

5.1 Introduction 85
5.2 Main Signal Cancellation Circuit 86
5.2.1 Measurement Set-Up 88
5.2.2 Breast Phantom Construction 93
5.3 Experimental Results 93
5.3.1 1D (Line) Scan Results 93
5.3.1 2D Scan results 97
5.4 Conclusion 99
6 CONCLUSION AND FUTURE WORK 107
REFERENCES 112
CURRICULUM VITAE 121

LIST OF TABLES

TABLES

Table 1.1 Summary of experimental results for elastic properties of *ex-vivo* breast tissues [28] 4

Table 1.2 Summary of magnetic resonance elastography results for elastic properties of in-vivo breast tissues [28] 5

Table 2.1 The properties of the FUS Probe (Sonic Concepts, H-102) [52] 20

Table 3.1 Acoustic medium parameters utilized in HITU Simulation program..... 50

Table 5.1 Compositions of one liter of fat and tumor phantom [90]. Abbreviations:, p-tol: p-toluic acid, n-prop: npropanol, forml.:formaldehyde, surf.:Surfactant , Ker: Kerosene 94

Table 5.2 Measured electrical and elastic parameters of the developed phantoms [52] 95

Table 5.3 The amplitude levels of the main signal and the Doppler signal for Cases I to IV 98

LIST OF FIGURES

FIGURES

Figure 1.1. The dielectric properties of breast tissues taken from 100 patients a) real part of the permittivity b) imaginary part of the permittivity of breast tissues [16]. Normal breast tissues are displayed with blues shades and malignant tissues are shown with red shades. The mean values are shown with solid lines. 2

Figure 1.2. The normal breast tissues can be subdivided into three groups regarding to their water and fat (adipose tissue) contents. As the water content increases the density of the breast also increases. The mean dielectric properties of the breast tissues a) real part of the permittivity as a function of microwave frequency b) imaginary part of the permittivity as a function of microwave frequency [16]. 3

Figure 1.3. HMMDI experimental 2D imaging of two cylindrical tumor phantoms inside a homogenous breast phantom for two different ultrasound vibration frequencies in [52]. a) 15 Hz vibration frequency b) 35 Hz vibration frequency. The cross section of the tumors are encircled with dashed red circles. As the vibration frequency is decreased, the tumors are imaged larger than their physical size. 7

Figure 2.1. The simplified block diagram of Harmonic Motion Microwave Doppler Imaging experimental set-up. 14

Figure 2.2. The frequency spectrum of the received signal. ω_m is the (microwave) radiation frequency of transmitter antenna, Δω is the frequency of vibration, K is the phase variation (in radians) of the signal due to vibration. 16

Figure 2.3. The block diagram of the experimental set-up for HMMDI [52] 18

Figure 2.4. The experimental set-up HMMDI with a) the FUS probe mounted on the 3D scanner b) the phantom and the coupling (oil) medium [52] 19

Figure 2.5. The pressure distribution of FUS Probe (Sonic Concepts, H-102) at its a) first resonance frequency b) at third resonance frequency [52] 19

Figure 2.6. Simulation Method for Solving the Forward Problem of HMMDI [49]. 21

Figure 2.7. The volume equivalent current modeling in forward EM simulation of HMMDI [49] a) In the original problem the source of the radiation is the transmitting antenna and the inclusion is present in the simulation b) In the equivalent (reciprocal) problem the tumor is replaced with equivalent volume electric current.. 24

Figure 2.8. The sequential flow of the HHMDI simulation [50]: Four consecutive FDTD simulations are required in order to compute the phase difference of the received signal at two time instants, T_{max} and T_{min}. 25

Figure 2.9. The sub cell method implementation in FDTD grid for the forward EM problem of HMMDI. The field component are displayed in y-z view of the 3D grid a) when there is no displacement b) when the position of tumor is updated with displacement data. E_{zs} is defined in the cells that displacement occurs [50] 27

Figure 2.10. HMMDI simulation model for monitoring effect of vibrating region (a) Top view of the simulation model: The position of 3 mm sized cubic tumor is swept on the grids in a 3D grid volume, (b) Side view of the simulation model: The positions of the FUS probe and transmit (T_X) and receive (R_X) antennas are fixed throughout the simulations... 29

Figure 2.11. Variation of received Doppler signal levels (dBm) in xy plane as a function of different tumor positions (mm) for the case when the FUS probe is focused at 3 cm beneath of the phantom surface level (focus) 31

Figure 2.12. (a) Variation of the Doppler signal levels as a function of tumor positions along A-B cut line (b) Variation of the Doppler signal levels as a function of tumor positions along C-D cut line.. 32

Figure 2.13. (a) Variation of the received Doppler signal levels as a function of different tumor positions along (xz plane) for the case when the FUS probe is focused at 3 cm beneath of the phantom surface level. The projection views of transmit (T_X) and receiving (R_X) antennas are marked with black rectangles and the FUS probe is marked with red cylinder at the center. (b) Variation of the Doppler signal levels as a function of tumor positions along E-F cut. 33

Figure 2.14. (a) Variation of the received signal levels as a function of different tumor positions along (yz plane) for the case when the FUS probe is focused at 3 cm beneath of the phantom surface level. The projection views of transmit (T_X) and receiving (R_X) antennas are marked with black rectangles and the FUS probe is marked with red cylinder at the center. (b) Variation of the Doppler signal levels as a function of tumor positions along G-H cut line. 34

Figure 3.1. DDA model for a cubic inhomogeneity with small dipoles. A cubic inhomogeneous tissue of edge length 3mm is represented via equidistant (12 x 12 x 12) 1728 dipoles 39

Figure 3.2. Formulation of scattering problem is simplified to finding the polarization of diploes from a determined system of 3N linear equations [67]. Once E_{inc} is known, the elements of *A* can be calculated via equations (3.3) and (3.4)... 41

Figure 3.3 Simulation procedure for calculation of the Doppler signal component. In acoustic simulations, FUS intensity is calculated in order to find the acoustic radiation force. In mechanical simulations, displacement distribution of the tumor is obtained at the instances that maximum and minimum tumor displacements occur. In electrical simulations, tumor inside a homogeneous tissue is represented as an array of dipoles. The displacement data is interpolated in order to find the displacement data of each dipole. The positions of dipoles are updated according to the interpolated displacement map for three different time instants. The DDA simulations are done for each case and the Doppler signal is extracted................. 48

Figure 3.4 Simulation procedure for single stage DDA simulation for the calculation of the Doppler signal. Apart from 3-stage DDA method, 1-stage DDA method the displacement data is added as phase term to the elements of the polarization of undisplaced case.. 49

Figure 3.5 Simulation model for the forward mechanical problem a) The tumor is modelled as a cube with 3 mm edge length and breast tissue phantom is modelled as a cube with 60 mm edge length. Position of the FUS transducer is fixed for mechanical simulations, its focus is at the symmetry center of the breast phantom b) In mechanical simulations, position of the tumor is swept by 1 mm grid steps along x axis (A-B line trajectory), then in z axis (C-D line trajectory) for a fixed FUS position. Both A-B and C-D tumor sweep line trajectories are 40 mm long and the lines intersect at the focus of the FUS transducer. 51

Figure 3.6 EM simulation geometry for receiving Doppler signal from a tumor inside breast tissue model a) Perspective view of simulation geometry: Breast tissue is modelled as cube with 60 mm edge length and tumor is modelled as a cube with edge length 3 mm. Transmit and receiving antennas are fixed at the bottom of breast tissue model b) Side view of simulation geometry: The tumor is moved along A-B line in x axis and C-D line in z axis. Both line trajectories are 40 mm long and they intersect at the focus of FUS transducer 53

Figure 3.7 Updating the positions of the dipoles with displacement data obtained in mechanical simulations. This figure illustrates the a) side view of the DDA model of a cubic tumor for the initial position (no vibration) which is represented by equally spaced dipoles. Their initial positions are encircled with dashed red circles. b) Dipoles are reoriented by shifting each dipole according to the interpolated displacement data. New positions of the dipoles are shown with dark grey color and shift from their initial (undisplaced) positions are shown with light grey colored shadow encircled with red dashed circles. 54

Figure 3.8 Comparison of EM simulation results computed from FDTD based code [50] and DDA based proposed EM simulation codes for cubic tumor with 3 mm edge length. For 30 Hz vibration frequency the tumor is swept along a) C-D line (along z axis) b) A-B line (along x axis)... 56

Figure 3.9 Comparison of EM simulation results computed from FDTD based code [50] and DDA based proposed EM simulation codes for cubic tumor with 3 mm edge length. For 60 Hz vibration frequency the tumor is swept along a) C-D line (along z axis) for 60 Hz vibration frequency b) A-B line (along x axis)......... 57

Figure 3.10 2D HMMDI scan simulation model: a small cubic tumor inside a medium adipose content breast tissue phantom (a) 2D scan model for the axial axes (yz), focus of the FUS probe is scanned over Axial scan area with 1 mm grid resolution (b) 2D scan model for the lateral axes (xy), focus of the FUS probe is scanned over Axial scan area with 1 mm grid resolution. 58

Figure 3.11 2D HMMDI scan simulation model: a small cubic tumor inside a medium adipose content breast tissue phantom. Original tumor is represented with red square (a) 2D scan model for the axial axes (yz), focus of the FUS probe is scanned over Axial scan area with 1 mm grid resolution (b) 2D scan model for the lateral axes (xy), focus of the FUS probe is scanned over Axial scan area with 1 mm grid resolution. 60

Figure 3.12 The displacement data of the tumor at Tmax instant when the focus of the FUS probe coincides with the volume center of the tumor is given in a) axial and b) axial directions 61

Figure 3.13 The scanned area for a tumor of fixed position in the HMMDI simulations performed with DDA method a) xz view b) yz view c) xy view. 63

Figure 3.14 The distribution of the normalized received Doppler signal from a 3 mm cubic tumor a) 2D xz view b) variation along A-B line c) variation along C-D line 64

Figure 3.15. The distribution of the normalized received Doppler signal from a 3 mm cubic tumor a) 2D yz view b) variation along A-B line c) variation along C-D line. 65

Figure 3.16. The distribution of the normalized received Doppler signal from a 3 mm cubic tumor a) 2D xy view b) variation along A-B line c) variation along C-D line. 66

Figure 3.17. The distribution of the normalized received Doppler signal from a 6 mm cubic tumor a) 2D xz view b) variation along A-B line c) variation along C-D line. 67

Figure 3.18. The distribution of the normalized received Doppler signal from a 6 mm cubic tumor a) 2D yz view b) variation along A-B line c) variation along C-D line. 68

Figure 3.19. The distribution of the normalized received Doppler signal from a 6 mm cubic tumor a) 2D xy view b) variation along A-B line c) variation along C-D line.. 69
Figure 4.1 Received Doppler signal level as a function of vibration frequency for various CD values (when the tumor is at the focus of the FUS probe) a) Altering the CD of a cubic tumor with 3 mm edge length while keeping CE value fixed as 1.5 b) The difference in the received Doppler signal level when increasing CD from 1.17 to 2.6 and 3.75 while keeping CE as 1.5. 75
Figure 4.2. Received Doppler signal level as function of vibration frequency for various CE values (when tumor is at focus of the FUS probe) a) Altering the CE of a cubic tumor with 3 mm edge length while keeping CD value fixed as 1.17 b) The change in the received Doppler signal level when increasing CE from 1.5 to 2.5 and 5 while keeping CD as 1.17 76
Figure 4.3 The ROD as function of vibration frequency for a 3 mm cubic tumor that located at a) 5 mm and b) 8 mm away from focus of FUS transducer along z axis. The ROD variation is presented for different CD and CE values. 77
Figure 4.4 The ROD as function of vibration frequency for a 3mm tumor that is located at 10 mm away from focus of FUS transducer along z axis. The ROD variation is presented for different CD and CE values. 78
Figure 4.5 The ROD as function of vibration frequency for a 3mm tumor that is moved a) 3 mm, b) 5 mm away from focus of FUS transducer along x axis. ROD variation is plot for different CD and CE values. 79
Figure 5.1. Schematic of the improved HMMDI experimental set-up: main signal 87
Figure 5.2. Simulation results for the spectrum of the received signal at combined output of Wilkinson divider when the phase difference between the ports of the divider is a) 90 degrees b) 135 degrees c) 160 degrees d) 170 degrees................. 89
Figure 5.3. Simulation results for the spectrum of the received signal at combined output of Wilkinson divider when the phase difference between the ports of the divider is a) 176 degrees b) 179 degrees c) 179.5 degrees d) 179.75 degrees........ 90

Figure 5.4. Implementation of MSC circuit on PCB; The 6 bit digital controlled phase shifter and attenuator are controlled with TTL signals. The transmitted RF signal is sampled via 30 dB coupler and the output of the MSC circuit is combined with the output of the receiving antenna. 91

Figure 5.5. Experimental HMMDI set-up. The FUS probe is scanned over the breast phantom. The focus of the FUS probe coincides the center of the breast phantom. 92

Figure 5.6. The breast phantoms tested in HMMDI setup a) one cylindrical homogeneous tumor phantom of size 16 mm (diameter) x 9 mm (height) is placed at the center of 30 mm height x 11 cm diameter breast fat phantom b) two cylindrical homogeneous tumor phantoms of size 15 mm (diameter) x 9 mm (height) and 7 mm (diameter) x 9 mm (height) with about 20 mm separation measured from their edges are placed on a 30 mm height x 11 cm diameter breast fat phantom 94

Figure 5.7. The spectrum of the received signal at the spectrum analyzer a) without MSC circuit and b) with MSC circuit. With the utilization of MSC circuit, the main signal is suppressed by approximately 20 dB and in the spectrum analyzer the Doppler signal become visible. 96

Figure 5.8. 1D line scan in x axis for cylindrical tumor inside a homogeneous fat phantom a) without MSC circuit and b) with MSC circuit. The arrow represents the tumor. 98

Figure 5.9. The spectrum of the received signal without main signal cancellation circuit: a) FUS transducer is OFF, b) FUS transducer is ON. ωm=4.5 GHz, $\Delta\omega$=30 Hz. Marker 1, 2, and 3 are located at the main signal frequency ωm, Doppler signal frequency $\omega m - \Delta\omega$ and the 50 Hz line frequency, respectively......................... 100

Figure 5.10. The spectrum of the received signal with main signal cancellation circuit: a) FUS transducer is OFF, b) FUS transducer is ON. ωm=4.5 GHz, $\Delta\omega$=30 Hz. Marker 1, 2, and 3 are located at the main signal frequency ωm, Doppler signal frequency $\omega m - \Delta\omega$ and the 50 Hz line frequency, respectively......................... 101

Figure 5.11. Experimental 2D scan of the breast phantom containing two cylindrical homogeneous tumor phantoms of size 15 mm (diameter) x 9 mm (height) and 7 mm (diameter) x 9 mm (height) with about 20 mm separation measured from their edges are placed on a 30 mm height x 11 cm diameter breast fat phantom 102

Figure 5.12. 2D imaging of the breast phantom with main signal cancellation circuit for ωm = 4.5 GHz and $\Delta\omega$ =30 Hz. Placement of the antennas and the tumor phantoms are shown on the plot... 103

Figure 5.13. Experimental 2D scan of the breast phantom in shown in Fig 5.11 rotated by 30 degrees.. 104

Figure 5.14. 2D HMMDI image of the fat phantom rotated by 30◦ in axial direction with HMMDI with main signal cancellation circuit for ωm = 4.5 GHz and $\Delta\omega$ =30 Hz. 105

LIST OF ABBREVIATIONS

ABBREVIATIONS	
ARF	Acoustic Radiation Force
FE	Finite Element
MRE	Magnetic Resonance Elastography
DCIS	Ductal carcinoma in situ
IDC	Invasive ductal carcinoma
FDTD	Finite Difference Time Domain method
SBC	Sheet Boundary Conditions
HMMDI	Harmonic Motion Microwave Doppler Imaging
FUS	Focused Ultrasound FUS
SNR	Signal to Noise Ratio
EM	Electromagnetic
DDA	Discrete Dipole Approximation
MI	Microwave Imaging
HMI	Harmonic Motion Imaging
AM	Amplitude Modulated
CW	Continuous Wave
HF	High Frequency
FDA	Food and Drug Administration

WAKZK	Wide-Angle Khokhlov-Zabolotskaya-Kuznetsov
Tx	Transmitting
Rx	Receiving
CG	Conjugate Gradient
Bi-CG	Bi-Conjugate Gradient
Bi-CGSTAB	Bi-Conjugate Gradient Stabilized
GMRES	Generalized Minimal Residual
QMR	Quasi-Minimal Residual
FFT	Fast Fourier Transform
FMM	Fast Multipole Method
ROD	Rate of Decrease
CD	The Contrast Between the Dielectric Properties
CE	The Contrast Between the Elastic Properties
ROD	Rate of Decrease
DRW	Displaced Region Width
MSC	Main Signal Cancellation
PCB	Printed Circuit Board

CHAPTER 1

INTRODUCTION

Breast cancer is one of the most prevalent type of cancers diagnosed among women [1]. The rate of mortality from breast cancer has decreased in two decades by 40% by the virtue of early detection [2]. Even if mammography is considered as a prominent method for breast cancer detection, it has drawbacks such as utilization of ionizing radiation, patient discomfort and false positive results especially for dense breast tissues. These inconveniences in mammography brought about researches on finding alternative, safe, non-invasive, reliable and low-cost methods for screening the early stage breast cancer.

In order to overcome the limitations of X-ray imaging, microwave imaging has emerged as a promising alternative non-invasive breast cancer detection method. Microwave imaging methods make use of the difference (contrast) between the dielectric properties of the normal breast tissues and tumors [3-13]. The dielectric properties of both normal and malignant breast tissues have been experimentally characterized up to 50 GHz [14-20]. Figure1.1 shows the distribution of the dielectric permittivities (real and imaginary part) of the breast tissues obtained from 100 patients (total 330 tissue samples) with ages ranging from 28 to 85 years old [16]. The normal breast tissues exhibit a wide range of permittivity values, and can be subdivided into three groups according to their water and fat (adipose tissue) contents (see Figure 1.2):

- *High adipose content tissues;* healthy breast tissues with low water content (low density) and with high adipose content more than 80 %,

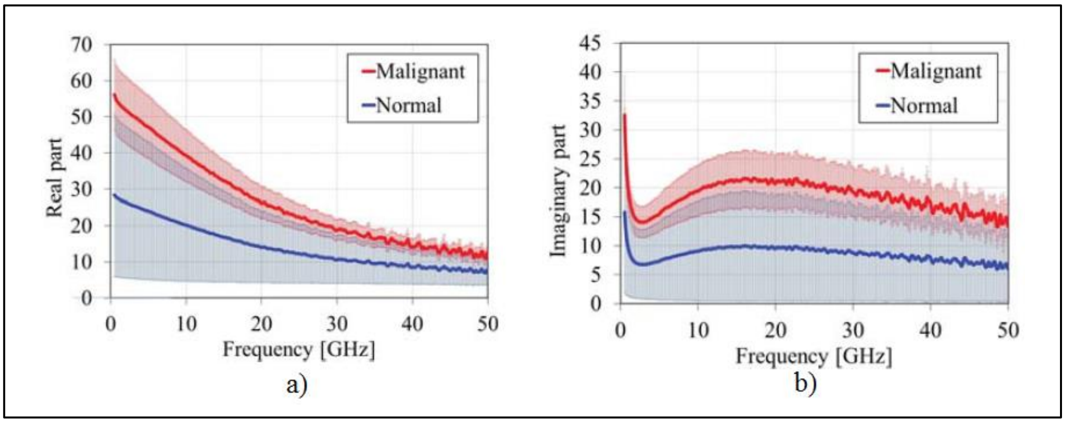

Figure 1.1. The dielectric properties of breast tissues taken from 100 patients a) real part of the permittivity b) imaginary part of the permittivity of breast tissues [16]. Normal breast tissues are displayed with blues shades and malignant tissues are shown with red shades. The mean values are shown with solid lines.

- *Medium adipose content tissues;* healthy breast tissues with moderate water content (medium density) and adipose content between 20 % and 80%,
- *Low adipose content tissues;* healthy breast tissues with high water content (high density) and adipose content less than 20 %.

In microwave imaging, the dielectric distribution inside the breast tissue is reconstructed by solving an inverse problem using the scattered electromagnetic fields. When a high adipose content breast is illuminated by electromagnetic waves, existence of malign tissues inside the breast give rise to high levels of scattered fields due to the large dielectric contrast compared to the surrounding breast tissue [14]. However, in [15-18] it was shown that low adipose content healthy breast tissues may have high dielectric permittivity values similar to that of malign tissues. As a result, discrimination of malign tumors inside low adipose content tissue (e.g. fibroglandular) is challanging.

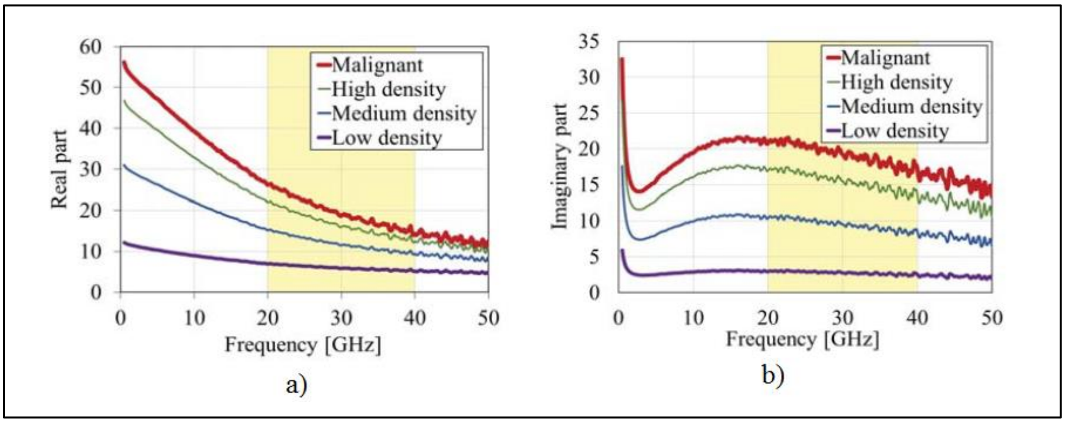

Figure 1.2. The normal breast tissues can be subdivided into three groups regarding to their water and fat (adipose tissue) contents. As the water content increases the density of the breast also increases. The mean dielectric properties of the breast tissues a) real part of the permittivity as a function of microwave frequency b) imaginary part of the permittivity as a function of microwave frequency [16].

Contrast between the elastic properties of the tissues inside the breast has also been utilized in breast imaging, since tumorous tissues are much stiffer than normal tissues due to denser microvascularisation [21] and collagen remodelling [22] during tumor development. The elasticity distribution inside the breast can be obtained by monitoring either the shear waves [23-24] or the local displacement of tissues [25-26] induced by acoustic radiation force (ARF) of ultrasound. In [27], an in-vivo experiment combining the ultrasound elastography and finite element (FE) was carried out in order to predict the tissue displacements. However, the FE model prediction was not accurate for mapping the breast due to its highly nonlinear mechanical behavior under compression and its complex morphology. The Young's modulus (E) is commonly used for quantifying the stiffness and elasticity of the tissues. As seen in Table 1.1, the Young's modulus of tumors were found to be 1.5-16 times higher than normal breast tissues in ex-vivo measurements [28-34]. In *in-vivo* studies using Magnetic Resonance Elastography (MRE), the ratio of the Young's modulus of tumorous tissues to that of normal tissues varied in the range of

Table 1.1 Summary of experimental results for elastic properties of *ex-vivo* breast tissues [28]

		Young's modulus (kPA)			
Study	*Pre-Strain*	*Normal Fat Tissue*	*Normal Glandular Tissue*	*Tumor (DCIS)*	*Tumor (IDC)*
Krouskop et al. [29]	5%	18-22	28-35	22-26	106-112
Wellman et al. [30]	1%	4.8	17.5	71.2	47.1
Samani et al. [31]	5%	3.25	3.24	16.38	19.9
Sarvazyan et al. [32]	Not Given	1	1.05	3.5	10
Matsumura et al. [33]	0-0.2 Stress	0.7	0.8	3.4	11.5
	1-1.2 Stress	17.3	15.4	15.6	27
Umemoto et al. [34]	1-1.2 Stress	19.08	16.99	16.15	30.5

1.1 to 7.8 (Table 1.2) [35-41]. Lower elasticity contrast ratios as measured in the *in-vivo* studies are due to tissue compression during measurement process resulting in stiffened glandular breast tissues [28].In [39], it was shown with a non-compressive MRE setup that the malign tissues are only 1.5 times stiffer than glandular tissues. Moreover, studies showed that the stiffness of fibro glandular tissue increases by aging [41] and even change during menstrual cycle [42]. Therefore, detection of tumor in a stiffened healthy breast tissue via mechanical imaging methods can be hard to realize owing to lower contrast in elastic properties of tissues.

Enhancement of breast imaging via making use of both dielectric and elastic contrast of the tissues was investigated in [43] and [44]. Microwave imaging methods rely on the level of scattered electromagnetic field from the inhomogeneity. When an acoustic or mechanical excitation is applied on a tumor, shape deformations

Table 1.2 Summary of magnetic resonance elastography results for elastic properties of in-vivo breast tissues [28]

		Young's modulus (kPA)		
Study	*Frequency (Hz)*	*Normal Fat Tissue*	*Normal Glandular Tissue*	*Tumor (IDC)*
Kruse et al [35]	100	15-25	30-45	50-75
Sinkus et al [36]	60	0.5-1	2-2.5	3.5-4
McKnight et al [37]	100	3.25	3.24	19.9
Lawrance et al [38]	50-100	0.43	2.45	-
Cheng et al[39]	Not Given	0.41	0.9	1.42
Xydeas et al [40]	65	1.2	1.2	3.1
Srivastava et al [41]	Not Given	4.17	-	16.45

(compression) occur depending on its mechanical properties. In that case, electromagnetic scattering from tumor is also affected from shape deformation on the tumor even if the change in the dielectric properties of the tumor is zero or negligible. This hybrid imaging method enables retrieving data related to elastic properties of tumor via monitoring the change in the scattered electrical fields from initial and deformed shape of tumor (i.e. Doppler component). In [45] and [46] analytical solution for the scattered field from infinitely long cylinders was formulated considering the acousto-EM interactions such as dielectric variations due to shape variation (perturbation). Numerical analysis of the scattered field from vibrating dielectric cylinders was derived via employing the Finite Difference Time Domain (FDTD) method with Sheet Boundary Conditions (SBC) [47].

Harmonic Motion Microwave Doppler Imaging (HMMDI) was recently proposed as an alternative hybrid imaging method for breast cancer detection, which employs simultaneous harmonic excitation of the tissue with a focused ultrasound probe and a microwave antenna [48-52]. In HMMDI ARF of ultrasound waves create local harmonic vibrations inside the tissue, and these vibrations lead to amplitude and phase modulations on the microwave signals scattered from vibrating region. Since maximum vibration amplitude (tissue displacement) is very small in terms of electrical length of the tissue (~0.01λ) [50], the amplitude modulation on the scattered field can be neglected. On the other hand, phase modulation yields a detectable signal at the Doppler frequency. The level of the Doppler signal depends on electrical and mechanical properties of the vibrating tissue as well as the level of maximum vibration during vibration of the tissue. The elasticity of the vibrating tissue, the vibration frequency, and the acoustic properties of the tissue are main parameters affecting the maximum vibration level. The image of the whole breast can be obtained by scanning the position of Focused Ultrasound (FUS) probe over the breast, and collecting the received Doppler signal level at each scan position.

In phantom experiments, HMMDI method was able to discriminate a small tumor inside a fibro glandular tissue availing of difference between tissue elasticities even though both tissues have similar dielectric properties [49], [50]. Since HMMDI method takes advantage of using all the contrast in electrical, mechanical and acoustic properties of the vibrating region with respect to those of the surrounding tissues, the effect of low contrast in these properties for tissue identification can be remedied by a higher contrast in another property. On the other hand, the relation between elastic contrast level and vibration of tissue is not same as the relation between dielectric contrast level and the scattered field, as they are two different mechanisms. Consequently, same amount of increase in contrast ratios either the dielectric or elastic properties of the tissue, does not yield same effect on Doppler signal level.

In HMMDI studies [49-52], during the imaging of large tumors, higher levels of Doppler signal are obtained when modulation (vibration) frequency of the ultrasound is decreased (Figure 1.3). Because modulation of the FUS transducer with lower vibration frequency yields maximum displacement of tissue at the focus in the expen-

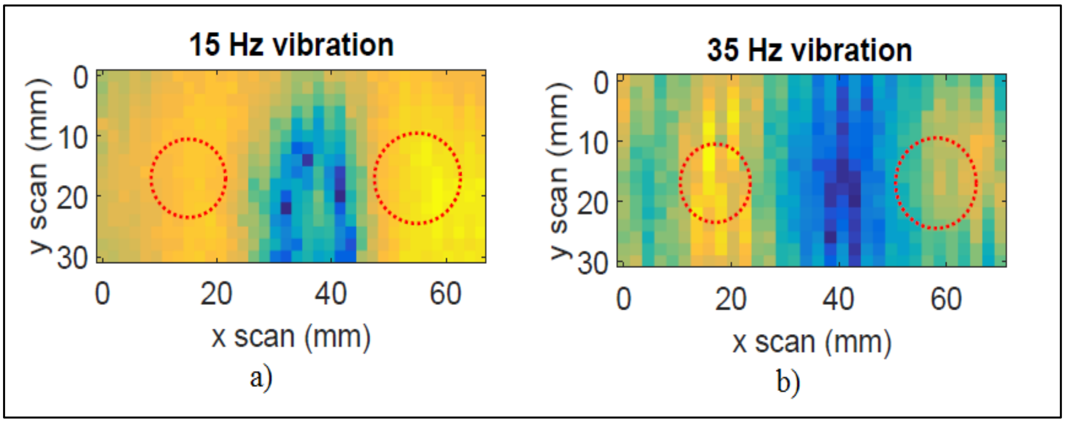

a)

b)

Figure 1.3. HMMDI experimental 2D imaging of two cylindrical tumor phantoms inside a homogenous breast phantom for two different ultrasound vibration frequencies in [52]. a) 15 Hz vibration frequency b) 35 Hz vibration frequency. The cross section of the tumors are encircled with dashed red circles. As the vibration frequency is decreased, the tumors are imaged larger than their physical size.

se of displacing larger volume around its focal region. Vibration in larger volume may provoke unintended vibration of tissues outside the focal region of FUS, leading to contributions of Doppler signals coming from neighboring tissues while imaging.

As a consequence, the resolution of HMMDI can deteriorate and image of tumors can be viewed larger than their respective physical size or two small neighboring tumors can be imaged as a one big tumor [52]. On the other hand, an increase in the vibration frequency results in a decrease in the Doppler signal level in HMMDI, due to lower displacements at higher vibration frequencies. For low Signal-to-Noise Ratio (SNR) (owing to low level of Doppler signal) cases, detection of small stiff tumors via HMMDI may fail. In the previous experimental studies, the optimal vibration frequency for detection was limited to 25-30 Hz. In the spectrum, the frequency of the Doppler signal is away from transmitted microwave signal only by the frequency of vibration, which is on the order of Hz’s. Consequently, the phase noise of the transmitter becomes crucial for the SNR.

1.1 Motivation of the Thesis

HMMDI comes forward in breast cancer imaging since it employs both electrical and mechanical properties of breast tissue. The contrast levels in dielectric and elastic properties of malignant and normal breast tissues enable the detection of the tumorous tissues. However, the level of the received Doppler signal is not a linear function of the contrast levels, especially for the mechanical properties. The vibration of the tissue has a complex dependency on acoustic and elastic properties of the breast tissue as well as its size. The effect of both mechanisms are required to be studied separately.

Simulation of the HMMDI was previously implemented in [49-50] using FDTD method by solving the displacement of the tissue under ultrasound excitation and the scattered electromagnetic field from the displaced region, sequentially. The forward problem of solving electromagnetic problem requires repeating the electromagnetic (EM) simulation for three cases; a) computation of scattered electric field when maximum displacement occurs, b) computation of electrical field when minimum displacement occurs, c) computation of electrical field when there is no displacement. Three consecutive FDTD electromagnetic (EM) simulations are required for the computation of Doppler signal component for a single scan point. The 3D Scan simulation of a breast model takes long time. Considering the duration of forward EM simulation, it becomes unpractical to analyze the effect of different contrast levels thoroughly via FDTD method. A fast EM simulation method is required to perform 3D scans for various contrast levels in the breast tissue.

The ultrasound excitation in HMMDI is applied by a FUS probe. The beamwidth of the FUS directly affects the displaced region, as the FUS has wider beamwidth of the acoustic radiation in the lateral axis than its axial axes [49]. Consequently, the resolution of HMMDI has more limitations while scanning in the axial direction. The effect of acoustic radiation intensity on HMMDI resolution in lateral and axial scans has not been studied yet.

In the experimental studies [50-52], it was observed that the phase noise of the transmitter directly affects the SNR of the received Doppler imaging. The coupling between the transmitter and receiver antennas are high for certain transmitting microwave frequencies. The SNR must be increased by vitiation of the phase noise of the transmitter signal so that better imaging in HMMDI can be achieved.

In this thesis, in order to overcome the problems mentioned above, the goals of this study are listed as follows;

1) Investigating the effects of unintended vibrations of the neighboring tissues off the focal region of the FUS probe:
   In a FDTD simulation scheme, a small cubic tumor with 3 mm edge is swept in a homogenous breast phantom. The position of transmitting and receiving antennas and FUS are kept fixed throughout the simulation.

2) Implementation of an efficient EM simulator:
   In this study, an alternative simulation scheme is implemented for solving the forward EM problem of HMMDI more efficiently than solving with FDTD method implemented in [49] and [50]. In the proposed method, DDA based method is utilized for the EM simulations since DDA provides a general solution handling the scattering from an arbitrary geometry [53-54], which enables accurately modeling shape deformed tissue due to vibration.

3) To study the impact of contrasts in dielectric and elastic properties of the breast tissues:
   Utilizing the DDA based fast simulation scheme, the dielectric and elastic properties of a small tumor model are parametrized keeping the dielectric and elastic properties of the homogeneous breast phantom surrounding the tumor model fixed throughout the simulations. The effect of dielectric contrast is explored as a function of vibration frequency for three different tumor dielectric constant values, while keeping elastic properties of the tumor fixed. Similarly, the effect of elastic contrast is obtained as a function of vibration

frequency for various tumor elasticity values while keeping the dielectric properties of the tumor fixed.

4) Investigating the effect of contrasts in dielectric and elastic properties of the breast tissues on HMMDI resolution due to off-focal vibrations:
   Similar to the item (1) listed above, position of a small cubic tumor is swept over 1 mm grids while keeping the position of the transmitting and receiving antennas and the FUS probe fixed. DDA based simulation method enabled investigation of off-focus vibrations as a function of vibration frequency for different dielectric and elastic contrast values.

5) Enhancing the SNR of the HMMDI experimental set-up:
   If the transmitted signal has high phase noise, the Doppler signal component may not be extracted from the spectrum. Moreover, direct coupling of the transmitted signal to the receiving antenna increases the main signal component, resulting the deterioration of SNR of the Doppler signal component. In this study, the level of coupling of main transmitted signal to the receiving antenna is minimized via implementing a coupling signal cancellation circuit. This circuit enhanced the SNR of the Doppler signal independent of the medium between (transmitting and receiving) antennas and the distance between antennas.

6) Effect of size of the inclusion (tumor) on HMMDI detection:
   The size of tumor is also an important parameter for HMMDI imaging. As the vibration frequency increases the displaced volume also decreases as the beam width of the acoustic radiation intensity decreases. In this study, the effect of size on the received HMMDI signal is analyzed as a function of vibration frequency.

1.2 Overview of the Thesis

This thesis consists of six chapters as follows;

In chapter 2, HMMDI method and its experimental set-up and FDTD simulation model are explained. By utilizing the FDTD code for solving the forward mechanical and EM problem [49], the effect of unintended vibrations of the neighboring tissues off the focal region of the FUS probe is studied. In the simulations, positions of antennas and the FUS are kept in a fixed position and the position of the tumor is swept.

In chapter 3, a DDA based alternative simulation method is proposed in order to solve the forward EM problem of HMMDI efficiently. New simulation method is verified by the FDTD code implemented in [49].

In Chapter 4, by employing the proposed method presented in chapter 3, the effect of contrast in dielectric and elastic properties of tumor on HMMDI is investigated as a function of vibration frequency. Moreover, similar to the simulation studies performed in chapter 2, the size and positions of the tumor are parametrized. Thus, the effect of contrasts in dielectric and elastic properties of the breast tissues on HMMDI resolution due to off-focal vibrations are investigated.

In chapter 5, in order to increase the SNR of HMMDI, a main signal cancellation circuit is proposed and implemented. The direct coupling of the main signal is reduced more than 15 dB, providing a 15-20 dB increase in the received HMMDI signal. As a result, in experimental set-ups vibration frequencies higher than 20 Hz can be utilized in HMMDI.

In chapter 6, the conclusions of this dissertation and the possible future studies for enhancing the HMMDI method are expressed.

CHAPTER 2

HARMONIC MOTION MICROWAVE DOPPLER IMAGING (HMMDI): THEORY, EXPERIMENTAL SET-UP AND SIMULATION METHOD

2.1 Introduction

The HMMDI method is a hybrid combination of Microwave Imaging (MI) and ultrasound based Harmonic Motion Imaging (HMI) [49-51]. This method aims to obtain a raster scan image of the breast tissue by measuring the level of the received Doppler signal at each scan position. The Doppler signal level strongly depends on electrical and mechanical properties of the tissue.

The basic block diagram of HMMDI set-up is shown in Fig. 2.1. In the HMMDI method, a FUS transducer is driven by an amplitude modulated (AM) signal to induce local oscillations at its focal region. The sinusoidally modulated acoustic radiation force (ARF) of the ultrasound waves generates local vibrations at the focus of the FUS transducer. Concurrently, electromagnetic waves are applied from a microwave transceiver system which has separate transmitting and receiving antennas.

The ARF exposed on the breast tissue is given by [55];

$$F = \frac{2\alpha I}{c_s} \tag{2.1}$$

where F is the acoustic radiation force per unit volume (kg/s^{2}cm^2), α (1/cm) is the absorption constant of the tissue, I (W/cm^2) is the acoustic beam intensity, and c_s (cm/s) is the speed of ultrasound inside the tissue. The short-term time average intensity of ultrasound (acoustic) beam can be written as [56];

$$\mathrm{I} = \frac{P_0^2}{4\rho c_s}\left(1 + cos(\Delta\omega t)\right) \tag{2.2}$$

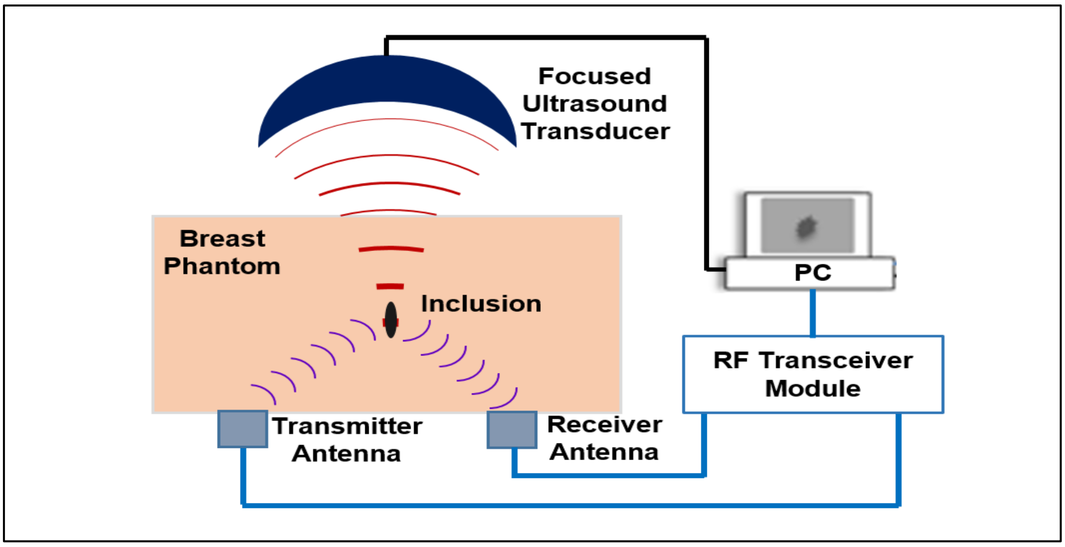
Focused
Ultrasound
Transducer
Breast
Phantom
Inclusion
PC
RF Transceiver
Module
Transmitter
Antenna
Receiver
Antenna

Figure 2.1. The simplified block diagram of Harmonic Motion Microwave Doppler Imaging experimental set-up.

where P_0 (Pa) is the pressure wave amplitude, $\Delta\omega$ (rad/s) is the vibration frequency of the tissue, and ρ (kg/m3) is the density of tissue. The local displacement of the tissue at the focus of FUS for a sinusoidal excitation can be obtained from [56];

$$\mathrm{X}(t) = \frac{F_0 cos(\Delta\omega t)}{\Delta\omega Z} = X_0 cos(\Delta\omega t + \varphi) \qquad (2.3)$$

where F_0 is the peak amplitude of the applied force on the local tissue, Z is the mechanical impedance of the tissue, and X_0 is the peak value of the local displacement, which depends on the elastic (mechanical) properties of the tissue.

When a monochromatic microwave signal is applied from a transmitting antenna to the vibrating tissue at the focus of a FUS transducer, the vibration yields phase modulation in the microwave signal scattered from the vibrating region. For a transmitted continuous wave (CW) microwave signal,

$$S_{TX}(t) = A\cos(\omega_m t) \qquad (2.4)$$

The scattered microwave signal observed by the receiving antenna can be expressed as [49]

$$S_{RX}(t) = B\cos\left(\omega_m t + \tfrac{4\pi R}{\lambda} + K\sin(\Delta\omega t) + \emptyset\right) \qquad (2.5)$$

where, B is the amplitude of the signal when there is no vibration, ω_m is the (microwave) radiation frequency of transmitter antenna, λ is wavelength of electromagnetic wave inside the tissue, R is the distance of the focus of the FUS transducer to the antennas (here, it is assumed that the vibrating region is equidistant to both transmitting and receiving antennas), $\Delta\omega$ is the frequency of vibration, K is the phase variation (in radians) of the signal due to vibration, and $\emptyset$ is constant phase difference resulting from total travel distance of the wave.

The cosine term of the received signal can be rewritten as;

$$\cos\left(\omega_m t + \frac{4\pi R}{\lambda} + K\sin(\Delta\omega t) + \emptyset\right) =$$

$$\cos\left(\omega_m t + \tfrac{4\pi R}{\lambda} + \emptyset)\ \right)\cos(K\sin(\Delta\omega t) - \qquad (2.6)$$

$$\sin\left(\omega_m t + \tfrac{4\pi R}{\lambda} + \emptyset)\ \right)\sin(K\sin(\Delta\omega t)$$

Since the practical displacement metrics of HMMDI is in the order of micrometers (μm) which is much smaller than the wavelength of the transmitted microwave signal (that is in the order of centimeters), K<<1 and the sine and cosine terms can be simplified as;

$$\cos(K\sin(\Delta\omega t) \approx 1 \qquad (2.7)$$

$$\sin(K\sin(\Delta\omega t) \approx K\sin(\Delta\omega t) \qquad (2.8)$$

Then, Equation (2.5) can be rewritten as;

$$\cos\left(\omega_m t + \tfrac{4\pi R}{\lambda} + K\sin(\Delta\omega t) + \emptyset\right) =$$

$$\cos\left(\omega_m t + \tfrac{4\pi R}{\lambda}\right) - \sin\left(\omega_m t + \emptyset + \tfrac{4\pi R}{\lambda}\right).K\sin(\Delta\omega t) \qquad (2.9)$$

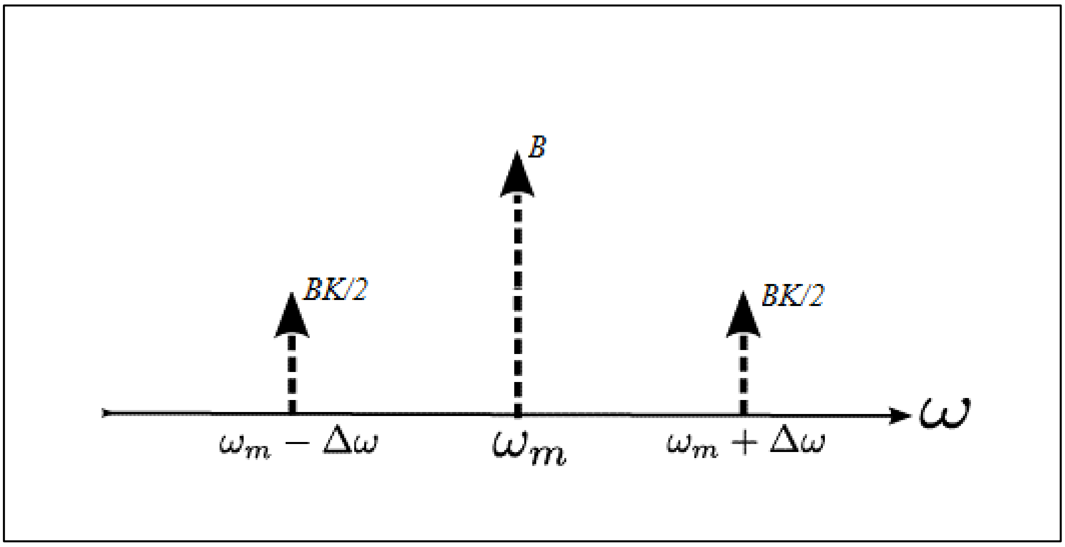

Figure 2.2. The frequency spectrum of the received signal. ω_m is the (microwave) radiation frequency of transmitter antenna, Δω is the frequency of vibration, K is the phase variation (in radians) of the signal due to vibration.

Using the trigonometric identities, the received signal can be re-expressed as;

$$S_{RX}(t) = B\cos\left(\omega_m t + \frac{4\pi R}{\lambda} + \emptyset\right) + B\frac{K}{2}[\sin(\omega_m t + \Delta\omega t + \emptyset_1) \\ + \sin(\omega_m t - \Delta\omega t + \emptyset_1)] \qquad (2.10)$$

The spectrum of the received signal is composed of three signals (Figure 2.2); one microwave signal at the main frequency component of the transmitted signal ω_m, and two Doppler signals at $\omega_m + \Delta\omega$ and $\omega_m - \Delta\omega$ frequencies. As seen in (2.10) the Doppler signal level is a function of displacement during vibration, where parameter K is related to vibration and elastic properties of the vibrating tumor, and parameter B is related to dielectric contrast between tumor and background tissue. Since the level of the received Doppler component is an indicator of both electrical (dielectric contrast) and mechanical (elasticity) properties of the vibrating tissues, tissues with similar dielectric properties inside the breast can be discriminated from each other due to their distinct elastic properties [50].

2.2 Experimental Set-Up for HMMDI

The verification of the proposed HMMDI method has been carried out with experiments [49-52]. In [50] detection of a tumor phantom inside a fibro-glandular phantom was achieved experimentally. In [52], multiple tumor phantoms inside a fatty breast phantom were imaged for different vibration frequencies. Moreover, in [52], a tumor inside a fibroglandular phantom was successfully imaged via time domain method that enabled faster breast scanning.

The block diagram of HMMDI set-up, and the experimental set-up with 3D scanner are shown in Fig. 2.3 and Fig. 2.4, respectively. The ultrasound waves are generated with a waveform generator and second waveform generator is utilized for AM modulation of the ultrasound signal in order to create displacement inside the phantom. The AM modulated signal is gated in burst mode and the burst signal is amplified via an HF power amplifier (Amplifier Research, model:150100B) feeding the FUS probe (Sonic Concepts, Model: H-102). The FUS probe is driven in its third harmonic in order to obtain a narrow ultrasound beam with high gain. The pressure profile of the FUS probe and its properties are given in Fig. 2.5 and Table 2.1, respectively. As the modulated ultrasound excitation is applied to the phantom, a single tone microwave signal is also transmitted from an open-ended waveguide antenna fed by a microwave signal generator (Agilent, Model: E8257C). The scattered electromagnetic field is received by a receiving antenna that is identical to the transmitting antenna. The physical dimensions (aperture) of the open-ended waveguide antennas are (22.5 mm x 10.3 mm). The cut-off frequency for the fundamental frequency (TE_{10}) is 4.07 GHz and next higher order mode (TE_{20}) starts at 8.1 GHz. The antennas are filled with vegetable oil ($\epsilon_R = 3.15, \sigma = 0.05$ [52]) in order to minimize the antenna aperture size and to conform to the phantom (i.e. practical breast size) geometry.

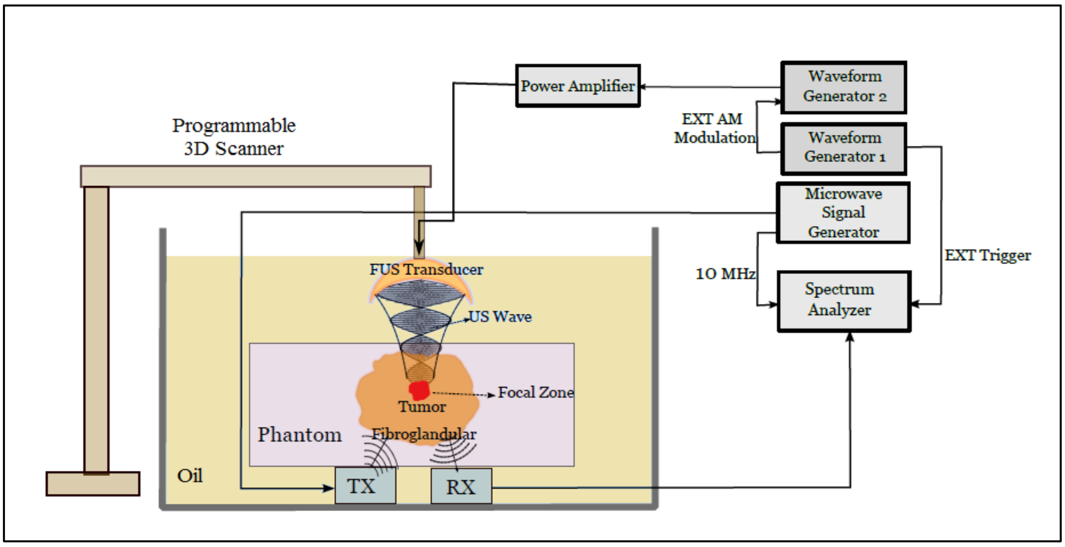
Power Amplifier
Waveform Generator 2
EXT AM Modulation
Waveform Generator 1
Programmable 3D Scanner
Microwave Signal Generator
EXT Trigger
10 MHz
Spectrum Analyzer
FUS Transducer
US Wave
Focal Zone
Tumor
Phantom
Fibroglandular
Oil
TX
RX

Figure 2.3. The block diagram of the experimental set-up for HMMDI [52]

The received signal is measured with spectrum analyzer (Agilent, Model: E446A). The waveform generator utilized for the modulation of the ultrasound signal triggers the spectrum analyzer in order to synchronize the sweep start time of the spectrum analyzer with the AM signal. To achieve phase coherence between microwave signal generator and spectrum analyzer, their 10 MHz references are matched.

2.3 Simulation Method for Solving the Forward Problem of HMMDI

The forward problem of HMMDI consists of sequential solving of acoustic, mechanical and EM problems and the sequential flow for calculation of the Doppler signal are given in Figure 2.6 [49]. In the acoustic problem, the acoustic distribution intensity inside the breast tissue is calculated by a simulator tool and the ARF is calculated using equation (2.1). In the mechanical simulations, in order to obtain the displacement map, the ARF calculated using the acoustic simulations is applied to the simulation model. During mechanical simulations, the displacement distribution

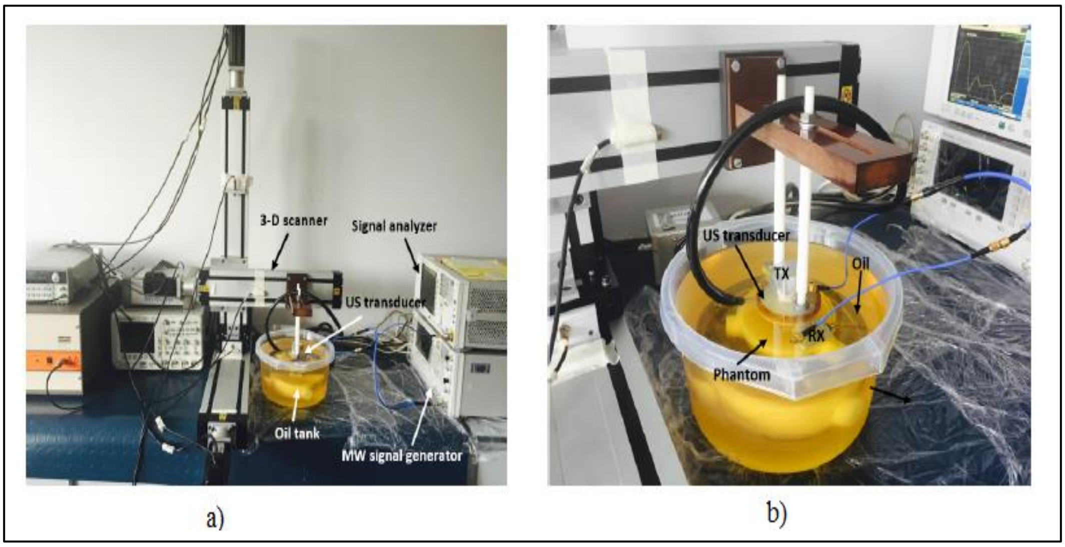
3-D scanner
Signal analyzer
US transducer
Oil tank
MW signal generator
US transducer
TX
Oil
RX
Phantom
a)
b)

Figure 2.4. The experimental set-up HMMDI with a) the FUS probe mounted on the 3D scanner b) the phantom and the coupling (oil) medium [52]

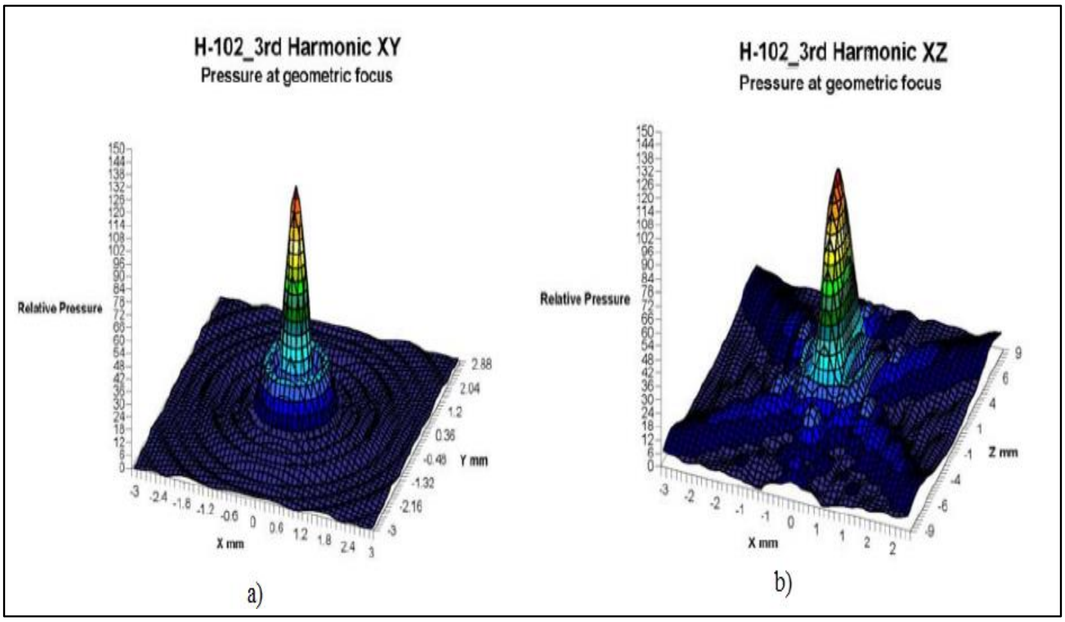

Figure 2.5. The pressure distribution of FUS Probe (Sonic Concepts, H-102) at its a) first resonance frequency b) at third resonance frequency [52]

Table 2.1 The properties of the FUS Probe (Sonic Concepts, H-102) [52]

Frequency	1.1 MHz (Fundamental)
	3.3 MHz (Third Harmonic)
Geometric Focus	63.2 mm
Thru Opening	20 mm (Ø)
Active Diameter	64 mm
Power Handling	150 W (CW)
Focal Depth	53.5 mm (measured from transducer housing rim to geometric focus)
Axial Half Intensity Beamwidth	15 mm (@ 1.1 MHz) 5 mm (@ 3.3 MHz)
Lateral Half Intensity Beamwidth	1.8 mm (@ 1.1 MHz) 0.6 mm (@ 3.3 MHz)

of the tissue at the maximum and minimum displacement time instants of the focal point are saved. The received Doppler signal can be extracted from the sequential EM simulations performed for that saved displacement distributions.

2.3.1 Acoustic and Mechanical Simulation Methods

The acoustic distribution intensity inside the breast tissue generated by the FUS probe is obtained by utilizing HITU simulator tool developed in MATLAB by US Food and Drug Administration (FDA) [57]. In this tool, wide-angle Khokhlov-Zabolotskaya-Kuznetsov (WAKZK) equation is solved in the frequency domain [57]. In this thesis, throughout the acoustic simulations, a transducer model with 1 cm inner radius, 2.1 cm outer radius, and 6 cm focal depth is utilized in order to be

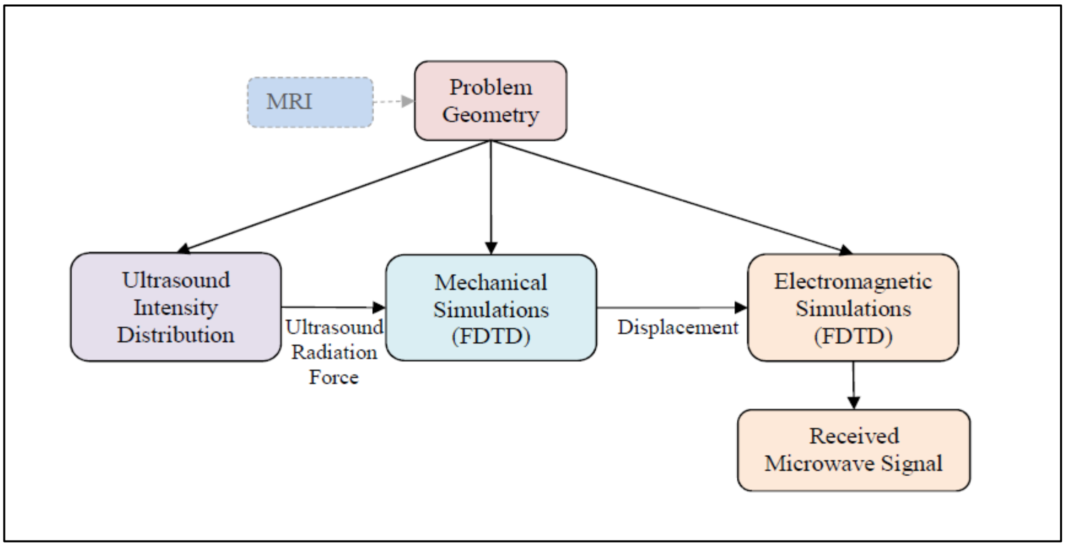
MRI
Problem Geometry
Ultrasound Intensity Distribution
Mechanical Simulations (FDTD)
Electromagnetic Simulations (FDTD)
Ultrasound Radiation Force
Displacement
Received Microwave Signal

Figure 2.6. Simulation Method for Solving the Forward Problem of HMMDI [49].

consistent with the previous studies in [49-52]. The simulation frequency is 3.33 MHz and 150 harmonics are included in the simulation.

The mechanical forward problem is implemented in 3D FDTD code in MATLAB© [50]. The ARF is computed from the acoustic radiation intensity obtained from HITU Simulator tool. The ARF on a specific voxel can be computed from [49];

$$F_{i,j,k} = \frac{2\alpha_{i,j,k} I_{i,j,k}}{c_{s_{i,j,k}}} \left(1 + \cos(\Delta\omega t)\right) \tag{2.11}$$

where $\alpha_{i,j,k}$ (Neper/m) is the absorption coefficient of (i,j,k)th voxel, $c_{s_{i,j,k}}$ (cm/s) is the absorption coefficient of (i,j,k)th voxel, $I_{i,j,k}$ (W/cm^2) is the acoustic radiation intensity in each of 3D grid cells.

The vibration characteristic of the tissue at the focus of FUS probe due to the applied ARF depends on the elastic properties of the tissue. Staggered-grid FDTD method was utilized in order to solve the forward problem for seismic wave propagation in elastic media [58, 59]. In the forward problem, coupled the velocity-stress equations are solved for an applied force on the body. The equations can be formulated as a set of first-order differential equations for a 3D grid cell as [49];

$$\frac{\partial v_i}{\partial \mathrm{t}} = \frac{1}{\rho} \left(\frac{\partial \tau_{ij}}{\partial x_i} + f_i\right) \tag{2.12}$$

$$\frac{\partial \tau_{ij}}{\partial t} = \lambda \delta_{ij} \frac{\partial v_k}{\partial x_k} + \mu \left(\frac{\partial v_i}{\partial x_j} + \frac{\partial v_j}{\partial x_i}\right) \tag{2.13}$$

where v_i values are the velocity components for time–differentiated displacements, ρ is the density of the medium, τ_{ij} the stress components, f_i values are the body force components, and λ and μ are the first and the second Lamé constants depending on the elastic properties of the medium, respectively.

2.3.2 Electromagnetic Simulation Method

The solution of the forward electromagnetic problem is based on implementation of the Volume Equivalence Principle [49] as two sequential simulations. In the first simulation, the transmitting antenna is the source of the electromagnetic radiation inside the breast and the electrical field distribution inside the breast is computed [49]. The total electric field inside the inclusion (tumor) is stored for the second simulation. In the second simulation, the transmitting antenna is passive and the inclusion is replaced by its equivalent volume electric current ($\vec{J}_{eq}$) [49];

$$\vec{J}_{eq} = (\varepsilon_{obj} - \varepsilon_b) \frac{d\vec{E}_{obj}}{dt} + (\sigma_{obj} - \sigma_b)\vec{E}_{obj} \tag{2.14}$$

where ε_{obj} is the dielectric permittivity of the inclusion, σ_{obj} is the conductivity of the inclusion; ε_b is the dielectric permittivity of the homogeneous breast tissue, σ_b is the conductivity of the homogeneous breast tissue, respectively. $\vec{E}_{obj}$ is total electric field distribution inside the inclusion obtained in the first simulation. Since the permabilities of both breast tissues and inclusion are constant, the equivalent magnetic current source is zero. The volume equivalent current source representation is presented in Fig. 2.7

In the second simulation, as the inclusion is modelled with equivalent current source, the electromagnetic radiation from the equivalent electric current source is computed inside the homogeneous breast tissue. The incident electric field on the aperture of the transmitter antenna is known from the first simulation and the scattered electrical field onto the aperture of the receiving antenna is computed. The transmission from transmitting antenna to the receiving antenna, i.e (S_{21}) parameter, can be computed as the ratio of the amplitude (A_1) and phase terms (Φ_1) of the electric field on the receiving antenna to the amplitude (A_2) and phase terms (Φ_2) of the electric field on the transmitting antenna [50].

Notice that the procedure above is applied for a single time instance of the simulation. In other words, the position of inclusion is fixed for both simulations. The harmonic motion (displacement of inclusion) can be modelled by repeating the calculation of transmission (S_{21}) at two time instants;

- At T_{max}, when maximum displacement of the tumor occurs. In order to find the phase modulation of the received signal due to maximum displacement, S_{21} is first calculated for undisplaced case and then calculated for the updated position of the inclusion at T_{max}. The difference between phase of S_{21} (φ_1) calculations are stored.
- At T_{min}, when minimum displacement of the tumor occurs. In order to find the phase modulation of the received signal due to minimum displacement, S_{21} is first calculated for undisplaced case and then calculated for the updated position of the inclusion at T_{min}. The difference between phase of S_{21} (φ_2) calculations are stored.

The forward EM simulation scheme is depicted in Fig. 2.8. The Doppler signal is a function of the phase modulation of the received signal on the receiving antenna, as

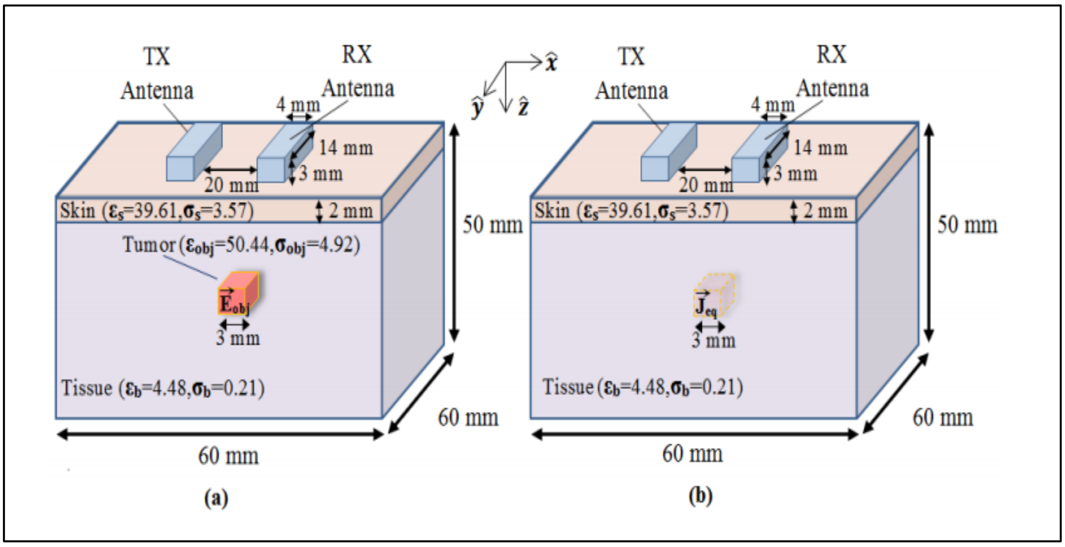
TX
Antenna
RX
Antenna
4 mm
14 mm
3 mm
20 mm
Skin (ε_s=39.61,σ_s=3.57)
2 mm
Tumor (ε_{obj}=50.44,σ_{obj}=4.92)
$\vec{E}_{obj}$
3 mm
Tissue (ε_b=4.48,σ_b=0.21)
50 mm
60 mm
60 mm
(a)
$\hat{x}$
$\hat{y}$
$\hat{z}$
TX
Antenna
RX
Antenna
4 mm
14 mm
3 mm
20 mm
Skin (ε_s=39.61,σ_s=3.57)
2 mm
$\vec{J}_{eq}$
3 mm
Tissue (ε_b=4.48,σ_b=0.21)
50 mm
60 mm
60 mm
(b)

Figure 2.7. The volume equivalent current modeling in forward EM simulation of HMMDI [49] a) In the original problem the source of the radiation is the transmitting antenna and the inclusion is present in the simulation b) In the equivalent (reciprocal) problem the tumor is replaced with equivalent volume electric current.

result the phase difference of the received signal at two time instants yield the level of Doppler component. The received Doppler component is calculated as;

$$S_{Doppler}(dB) = S_{undisplaced}(dB) - 20log_{10}\left(\frac{\emptyset_1-\emptyset_2}{2}\right) \qquad (2.15)$$

where $S_{undisplaced}(dB)$ is the level of scattered field calculated at the aperture of receiving antenna obtained from the simulation that tumor is undisplaced, $\emptyset_1$ is the phase of the scattered field calculated at the aperture of receiving antenna obtained from the simulation for maximum displacement of tumor at Tmax and , $\emptyset_2$ is the phase of the scattered field calculated at the aperture of receiving antenna obtained from the simulation for minimum displacement of tumor at Tmin.

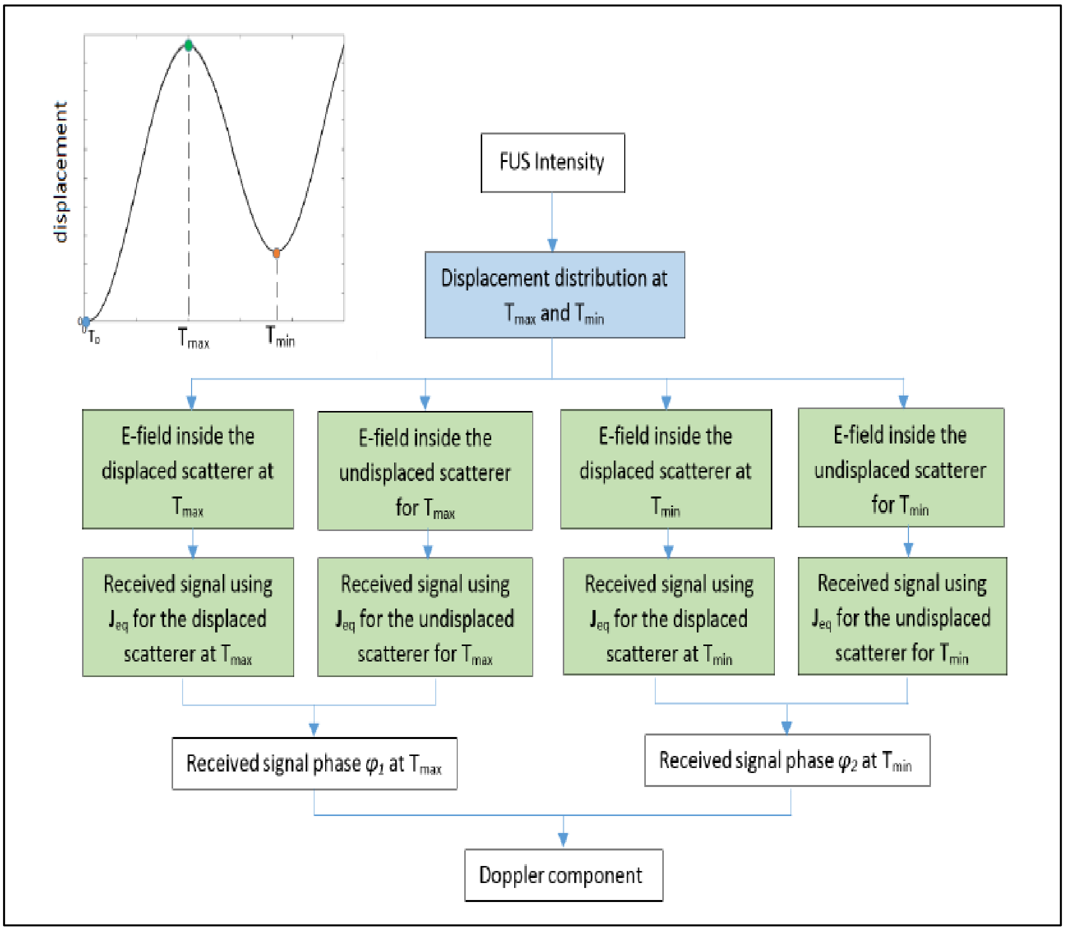
displacement
T_0
T_{max}
T_{min}
FUS Intensity
Displacement distribution at T_{max} and T_{min}
E-field inside the displaced scatterer at T_{max}
E-field inside the undisplaced scatterer for T_{max}
E-field inside the displaced scatterer at T_{min}
E-field inside the undisplaced scatterer for T_{min}
Received signal using J_{eq} for the displaced scatterer at T_{max}
Received signal using J_{eq} for the undisplaced scatterer for T_{max}
Received signal using J_{eq} for the displaced scatterer at T_{min}
Received signal using J_{eq} for the undisplaced scatterer for T_{min}
Received signal phase φ_1 at T_{max}
Received signal phase φ_2 at T_{min}
Doppler component

Figure 2.8. The sequential flow of the HHMDI simulation [50]: Four consecutive FDTD simulations are required in order to compute the phase difference of the received signal at two time instants, T_{max} and T_{min}.

The calculation the Doppler component of the forward EM problem was implemented in 3D FDTD scheme via MATLAB [49] in order to be consistent with the staggered grid model in mechanical simulations. Implementation of the Maxwell equations, easy modelling of the open-ended waveguides as antennas and conforming the boundaries to Convolutional Perfectly Matched Layer (CPML) are the main advantages for utilizing the FDTD method. Moreover, any inhomogeneity inside a realistic breast tissue can be easily modelled in FDTD.

The grid size of the 3D FDTD cubic lattice is selected as 1 mm in both mechanical and EM simulations. However, the maximum displacement metrics of the tumor inside the breast tissue is in the order of microns. When the position of the tumor is updated with the displacement data, the edges of the tumor will not lay on the grid lattice as seen in Fig. 2.9. The effect of the small displacements are handled with modification of normal electric field (E_z) with sub–cell method, inspired from the field calculation of the thin sheet materials in [60]. In the cells that have inhomogeneity due to displacement (containing both breast tissue and the tumor), the normal electric field (E_z) is splitted into two components: E_z and E_{zs} [50]. E_z represent the unchanged part (in terms of dielectric properties) of the cell even after the displacement whereas E_{zs} is defined for the sub cells where the properties of the medium changes due to displacement as seen in Fig. 2.9. The sub cell method in this FDTD code can handle the inclusions with arbitrary shapes, as a result, realistic breast tissues can be simulated in HMMDI studies with the FDTD code implemented in [50].

2.4 Resolution Analysis of HMMDI

In HMMDI method, image resolution depends on the volume of the vibrating (displaced) region induced by the FUS probe. As the half intensity beamwidth of acoustic pressure gets larger, the volume of the displaced region increases.

In this work, the FUS probe is operated at its third resonance frequency, in order to yield narrow lateral and axial half pressure intensity beamwidths. However, half intensity beamwidth of pressure is much larger in the axial direction than the beamwidth in the lateral direction. As shown in Table 2.1, the H-102 FUS probe, has 5 mm axial half intensity beamwidth and 0.6 mm lateral half intensity beamwidth. The resolution of HMMDI is better in lateral direction than in axial direction.

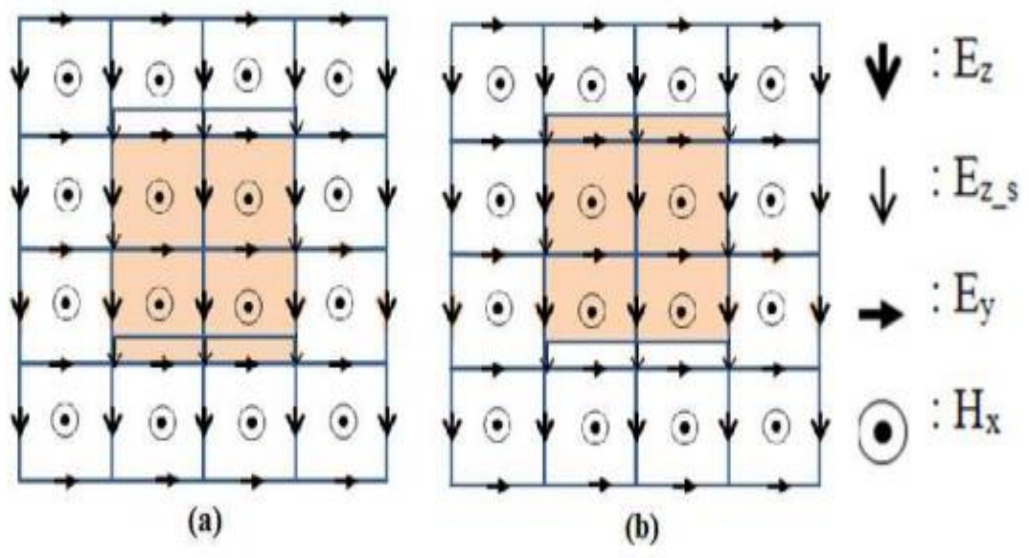

Figure 2.9. The sub cell method implementation in FDTD grid for the forward EM problem of HMMDI. The field component are displayed in y-z view of the 3D grid a) when there is no displacement b) when the position of tumor is updated with displacement data. E_{zs} is defined in the cells that displacement occurs [50]

The vibration frequency also affects the resolution of HMMDI since the FUS probe vibrates a larger volume than the ultrasound probe’s focal zone depending on the vibration frequency. In this section, the effect of the resultant displacement distribution on the HMMDI data profile is analyzed using the Finite Difference Time Domain (FDTD) simulation method explained in Section 2.3.

The position of a small cubic tumor model of edge size 3 mm was swept on a 3D grid as shown in Fig.2.10. The positions of the receiving and transmitting antennas and the FUS probe are fixed throughout the simulations. Since the position of the FUS probe is unchanged throughout the simulations, acoustic radiation intensity was computed only once. The mechanical and forward EM simulations were performed sequentially for each position of tumor. The level of HMMDI signal as a function of tumor positions are mapped in 2D cuts for the lateral (xy) and axial (xz and yz) planes. The sensitivity distribution of the HMMDI method can be obtained from these maps and an insight on the resolution of the method is inferred for the assessment of experimental studies. The vibration frequency in this study is chosen as 35 Hz to be consistent with experimental studies in [52].

2.4.1 The Simulation Model

The sequence of the simulations are as follows;

- Firstly, for each tumor position, the displacement map within the breast tissue is calculated by solving the forward mechanical FDTD simulation model for fixed the FUS probe source. The displacement map due to the vibration is recorded at the instants of first maximum and first minimum focal displacement via two different (mechanical) FDTD simulations.
- In the second step, the obtained displacement map from the mechanical problem is utilized as an input for the forward electromagnetic problem to calculate the level of the Doppler signal received in the receiving antenna. In the electromagnetic FDTD simulations, these displacement maps, recorded from (mechanical) FDTD simulations are used to obtain the phase of the received microwave signal. The difference of the phase responses of the received signals obtained at the instances of maxima and minima of the vibration yields the level of received Doppler component

In the simulations, the FUS probe is placed 3 cm above the phantom as seen in Fig. 2.10. The transmitting and receiving antennas are fixed at the bottom of the phantom. Normal tissue is modeled as homogeneous fat tissue with dielectric constant, ε_R = 4.48; conductivity, σ = 0.21 S/m and Young's modulus, E =5 kPa. The small tumor

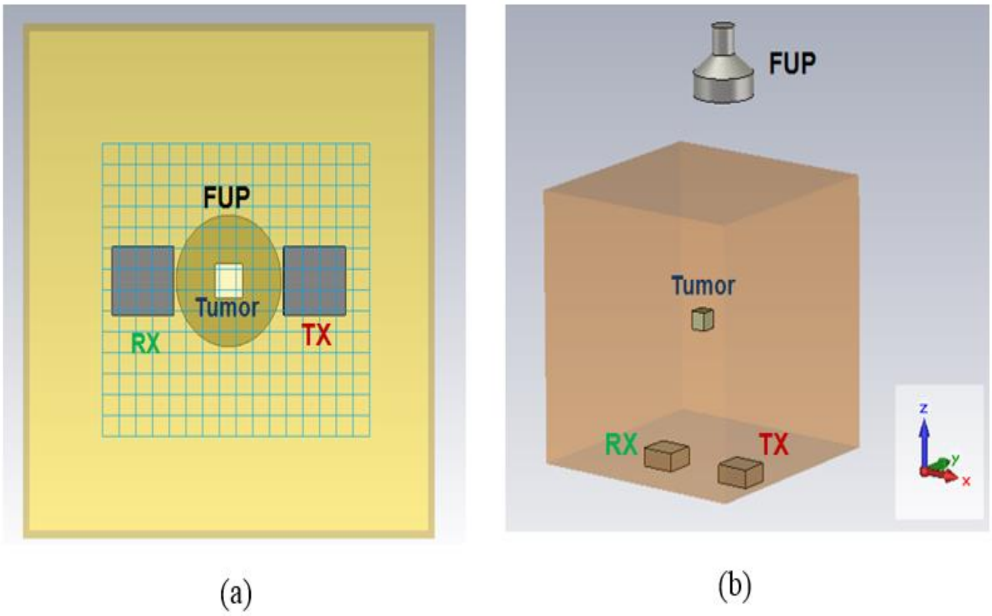

Figure 2.10. HMMDI simulation model for monitoring effect of vibrating region (a) Top view of the simulation model: The position of 3 mm sized cubic tumor is swept on the grids in a 3D grid volume, (b) Side view of the simulation model: The positions of the FUS probe and transmit (T_X) and receive (R_X) antennas are fixed throughout the simulations.

is modelled with dielectric constant, $\varepsilon_R = 50.44$; conductivity, $\sigma = 4.91$ S/m and Young's modulus E=20 kPa. The transmitting and receiving antennas are modelled with open-ended waveguides of dimensions of 23 mm x 14 mm x 17 mm filled with sun flower oil ($\varepsilon_R = 3.15$) and antennas are placed in H plane orientation. The center frequency of the microwave signal is chosen as 4 GHz and the vibration frequency is 35 Hz similar to experimental studies in [52]. The transmitted power is +10 dBm. In the simulation model, outer radius of the FUS probe is 2.1 cm; inner radius of the FUS probe is 1 cm, and the focal depth is 6 cm at 3.3 MHz. The FUS probe applied 1.23 MPa peak negative pressure inside the tissue, which is similar to experimental studies.

Keeping the focus of the FUS probe at the origin of the xy plane, the position of a tumor of 3 mm x 3 mm x 3 mm is swept in the xy-plane (48 mm x 38 mm area), in the xz-plane (48 mm x 50 mm area), and in the yz-plane (38 mm x 50 mm area). As currently the smallest tumor phantom that can be produced for the experimental studies is 3 mm x 3 mm x 3 mm, this size was selected for the simulation studies for the purpose of comparison. The radiation intensity and position of FUS probe is kept at fixed position and for each position of tumor, the level of received Doppler signal at receiving antenna is calculated. The simulation time for each tumor position on computer with Intel Xeon E5-2696 V4 processor was 4 hours. The grid steps are chosen as 3 mm, 3 mm and 5 mm for the x, y and z axes, respectively.

2.4.2 The Simulation Results

The amplitude level of the Doppler component for the 2D lateral cut (xy-plane) is plotted in Fig. 2.11 as a function of tumor position. The signal levels along the x and y axis cuts are given in Fig 2.12(a) and Fig. 2.13(b), respectively. The peak value of received Doppler signal is -86.2 dBm, when the tumor is exactly at the focus of the FUS probe.

When the tumor is displaced by 3 mm away from focus of the FUS probe in the x-axis, the received Doppler level decreases to -100.2 dBm. In the y-axis, similar signal levels were observed in two grid positions. The signal decreases to -97.63 dBm in the next grid positions. This cut is symmetric, while the x-axis cut has an asymmetry. The received signal level in the axial planes of FUS probe, are given in Fig 2.13 (xz-plane) and Fig 2.14 (yz-plane). Notice that the scan position in the x-axis starts from x=5 mm and in y-axis starts from y=10 mm. As a result, with grid step of 3 mm, E-F and G-H lines do not intersect each other. Moreover, since axial beamwidth of the FUS probe is larger than that in lateral plane, the grid step size in z axis for the simulation was chosen as 5 mm. When the tumor is placed 5 mm away from focus in the negative z-direction, the received Doppler signal drops to -98.73 dBm, whereas it decreases to -108.42 dBm in the positive z-direction (Fig. 2.13(b)). In the

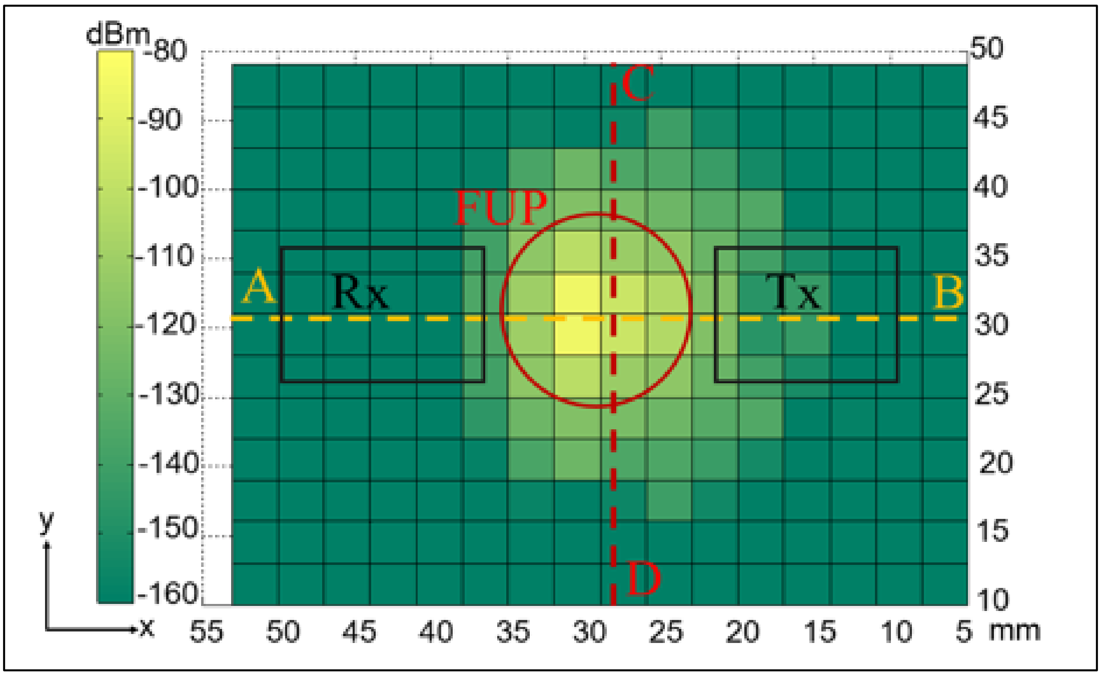

Figure 2.11. Variation of received Doppler signal levels (dBm) in xy plane as a function of different tumor positions (mm) for the case when the FUS probe is focused at 3 cm beneath of the phantom surface level (focus)

yz-plane, the signal level decreases to -94.2 dBm as the tumor is displaced 5 mm in the -z direction, and to -115.3 dBm in the +z-direction (Fig 2.14(b)).

It is observed that the maximum received Doppler signal level is obtained when the tumor is at the focus of the FUS probe, and as the tumor is moved 3 mm away from the focus in the lateral axis and 5 mm away from the focus in the axial axis, the received Doppler signal level decreases, substantially. In the lateral (xy) plane, 10 dB decrease in the received Doppler signal can be observed within a circle of 3 mm radius around the focus. These results show that resolutions on the order of millimeters can be achieved with the HMMDI method while detecting a tumor in a high adipose (fat) breast tissue. The received Doppler signal is higher when the tumor

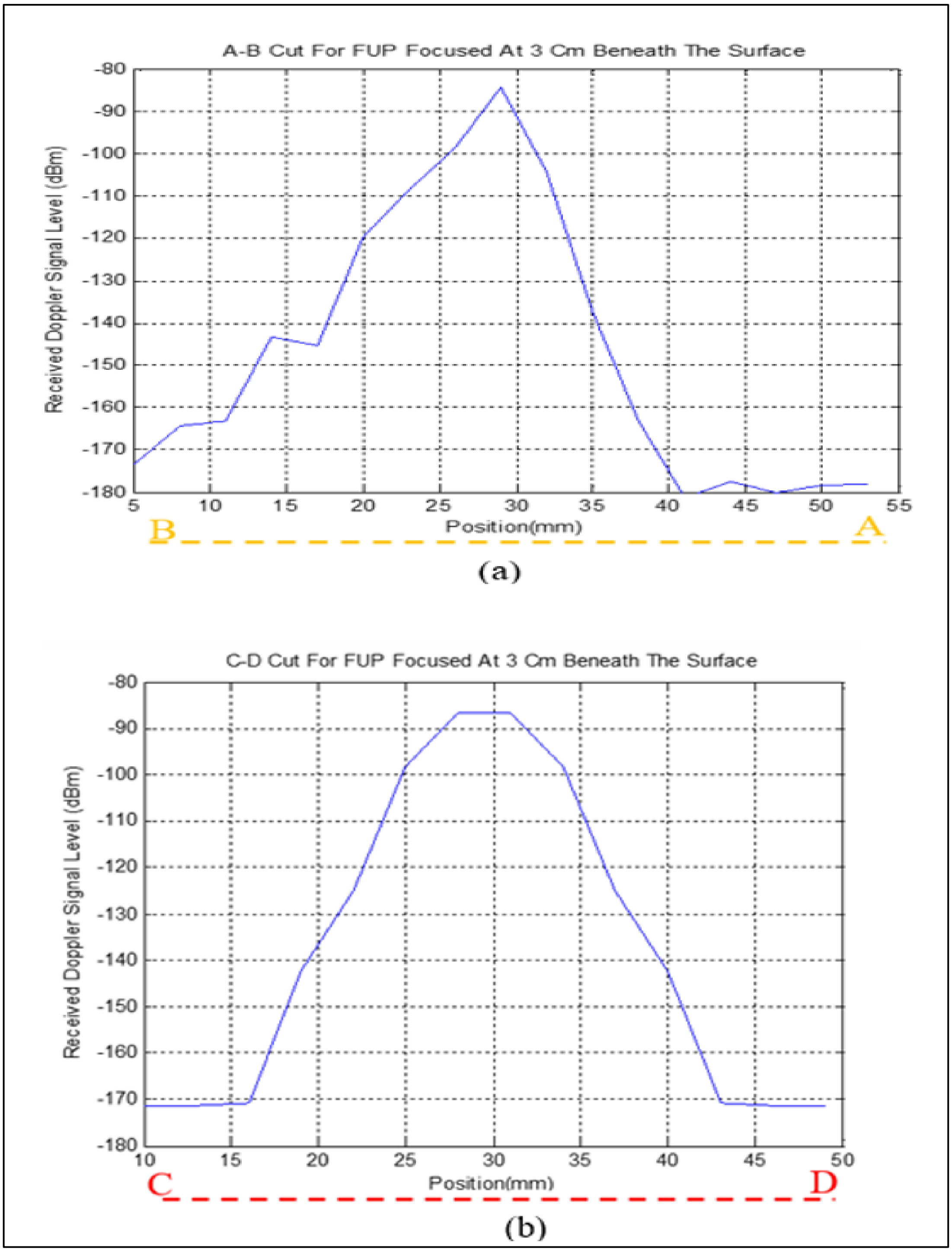

Figure 2.12. (a) Variation of the Doppler signal levels as a function of tumor positions along A-B cut line (b) Variation of the Doppler signal levels as a function of tumor positions along C-D cut line.

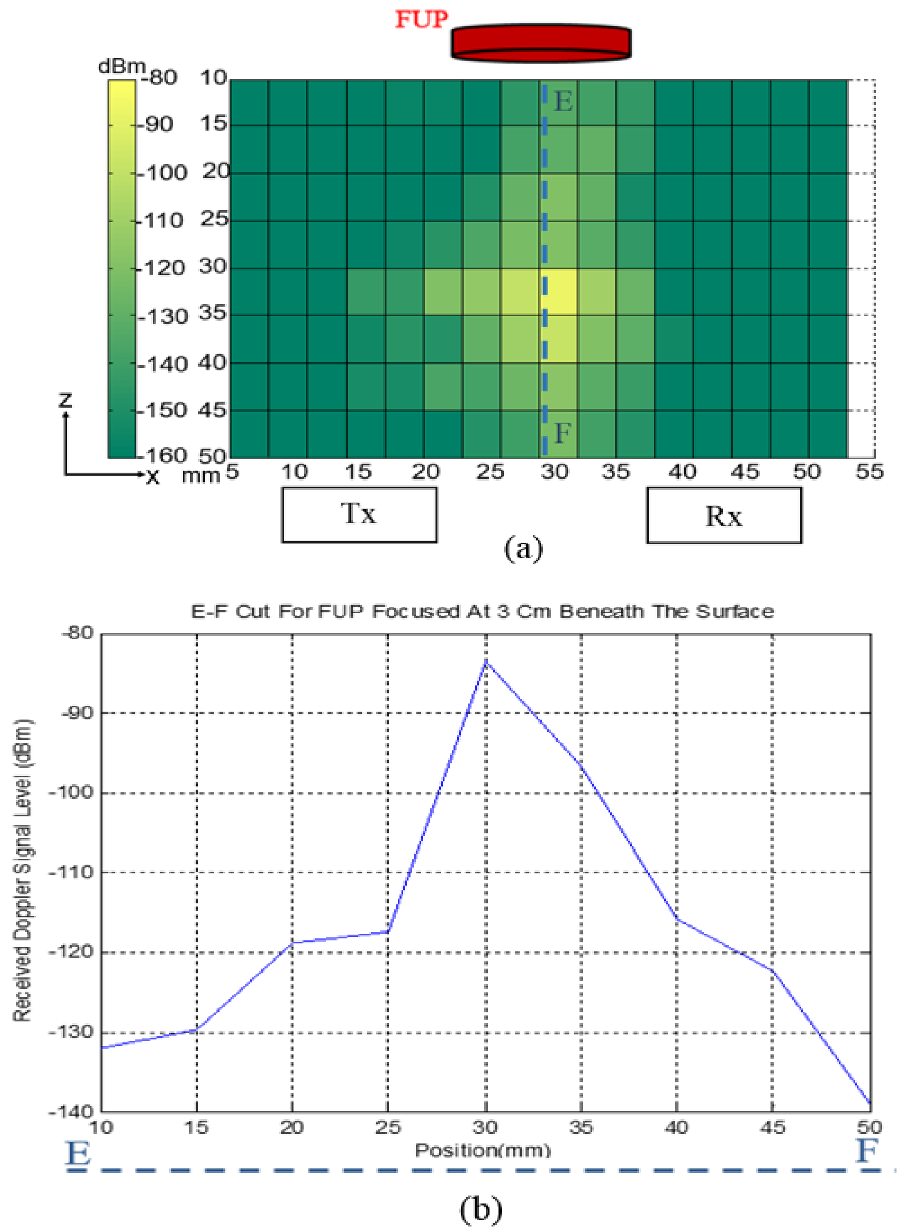

Figure 2.13. (a) Variation of the received Doppler signal levels as a function of different tumor positions along (xz plane) for the case when the FUS probe is focused at 3 cm beneath of the phantom surface level. The projection views of transmit (Tx) and receiving (Rx) antennas are marked with black rectangles and the FUS probe is marked with red cylinder at the center. (b) Variation of the Doppler signal levels as a function of tumor positions along E-F cut.

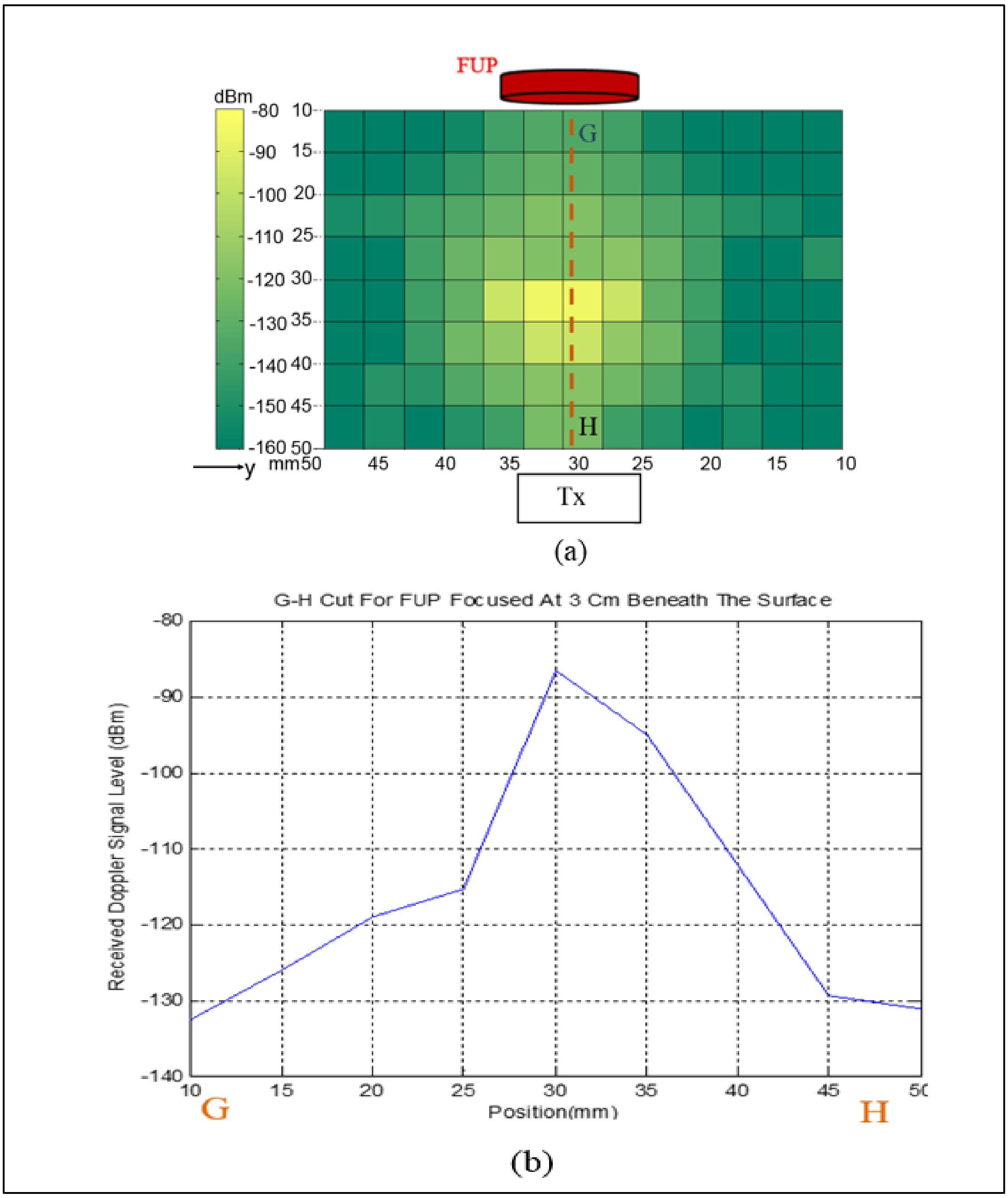

Figure 2.14. (a) Variation of the received signal levels as a function of different tumor positions along (yz plane) for the case when the FUS probe is focused at 3 cm beneath of the phantom surface level. The projection views of transmit (Tx) and receiving (Rx) antennas are marked with black rectangles and the FUS probe is marked with red cylinder at the center. (b) Variation of the Doppler signal levels as a function of tumor positions along G-H cut line.

is closer to the transmit antenna compared to the case when tumor is closer to the receiving antenna. This may be a result of scattering coefficient variation for the cubical tumor (bistatic radar cross section) as a function of microwave incidence angle.

2.5 Conclusion

Since HMMDI is a hybrid method employing both microwave imaging and harmonic motion imaging, the received Doppler signal is a function of the dielectric and mechanical properties of the tissue and the vibration frequency of the FUS probe. In order to simulate HMMDI, acoustic, mechanical and electrical simulations are carried out sequentially. The acoustic intensity of the FUS probe is found in acoustic simulations. The ARF is calculated from acoustic intensity and it is utilized as driving source while solving stress-strain equations in mechanical simulations in order to find the tissue displacement as a function of time. The EM simulations were carried out for three time instants such as when tissue is i) undisplaced, ii) displaced maximum, iii) displaced minimum. Moreover, for each of these instants, the EM simulation comprises of two consecutive simulations solving the scattering problem via Volume Equivalence Principle. Hence, six sequential FDTD simulations are required for the calculation of Doppler signal at single position of FUS probe during scan.

The FUS probe excitation is the main drive force for the harmonic motion yielding a Doppler signal component signal in the receiver. The displaced region at the focus of FUS probe depends on the transducer parameters. Because the momentum transfer during ultrasound excitation is mostly axial, the beamwidth is higher in axial direction and the resolution of HMMDI is low is axial axes. In previous studies [52], at low vibration frequencies, the tumors in breast phantom were appeared larger than their original sizes. In this chapter, the FUS probe is kept at a fixed position and the position of tumor is swept in the grids of 3D scan volume in order to study the resolution of the HMMDI for a small tumor of size 27 mm^3. Since the lateral resolution of FUS probe is better than axial axis, the tumor is swept by 3 mm grids in lateral axis and 5 mm grids in axial axes.

In the lateral (xy) plane, 10 dB decrease in the received Doppler signal is observed within a circle of 3 mm radius around the focus. These results show that resolutions on the order of millimeters can be achieved with the HMMDI method while detecting a tumor in a high adipose (fat) breast tissue.

In the simulation study in Chapter 2.4, the simulation time for each tumor position on computer with Intel Xeon E5-2696 V4 processor was 122 minutes. As a result, a simulation study with smaller grid step for scan is impractical utilizing the FDTD code in [49]. In the next chapter, fast simulation scheme is proposed for HMMDI simulations.

CHAPTER 3

IMPLEMENTATION OF A FAST SIMULATION SCHEME FOR THE FORWARD EM SIMULATION OF HMMDI

3.1 Introduction

In the previous simulation studies on HMMDI, the forward electromagnetic problem was modelled via the FDTD method since its staggered grid nature enabled the use of displacement data directly, which is obtained from mechanical FDTD simulations [49]. Moreover, FDTD provides an accurate and efficiently implementable platform to model the EM problem for complex geometries and realistic models. However, the solution of the forward electromagnetic problem is based on the implementation of the Volume Equivalence Principle [49] as two sequential simulations, which are performed for three different time instants; T_0: when there is no displacement, T_{max}: when the displacement is maximum and T_{min}: when the displacement is minimum. As a result, for each position of the FUS probe during a scan, six FDTD simulations are required that last 4 hours on a computer with Intel Xeon E5-2696 V4 processor.

The received Doppler signal in HMMDI depends on the dielectric and elastic contrasts between the tumor and the background tissue, the vibration frequency and the size of the tumor. To investigate the effect of each of these parameters on the received Doppler signal while 3D scanning the breast tissue, the FDTD simulation duration is impractical. Therefore, in order to study the effect of the contrast parameters and vibration frequency, a new simulation method is required.

In [61], the FDTD simulation method for the forward EM problem of HMMDI was accelerated with the utilization of Parallel Computing and vectorization of the FDTD code. On a computer workstation with GPU computing, the simulation time was decreased by 19 times [61]. However, the GPU computing requires a high cost computing hardware. An alternative efficient and faster simulation toll is required for the parametric study of contrast mechanisms in the HMMDI as a function of vibration frequency. In this chapter, a DDA based simulation method is proposed for solving the forward problem of HMMDI in order to study the effect of contrast mechanism and vibration frequency. DDA method provides a general solution for calculation of scattered electromagnetic field from and arbitrary shape [62], which enables accurately modelling of shape deformation of tissues under harmonic motion of ultrasound excitation. This method was also previously utilized for microwave breast cancer imaging methods [63-65]. There are also open source DDA codes available in literature for simulations [66-68]. The proposed method is verified by solving the problem with the FDTD code in [50].

3.2 DDA Based Simulation Method (3-Stage)

The DDA method is a generalized computational technique for calculation of scattering and absorption of electromagnetic waves from arbitrarily shaped geometries [62]. The DDA method was initially devised by Purcell and Pennypacker [69], representing the scatterer object with a finite number of dipoles (Fig 3.1). The method is also known as "coupled dipole approximation" [68]. The DDA method is a full-wave method that it can also be derived from discretized electric field integral equations via subdividing the scatterer into a set of sub-volumes [70].

In DDA, arbitrary shaped scatterer object can be modeled by an array of point dipoles [70]. The incident electrical field induces dipole moments at each dipole, and the dipoles start to interact with each other's electrical fields. For an array of N dipoles, the polarization of the jth dipole (j=1, 2, …, N) at position $\vec{r_j}$ is expressed as [62]:

$$\vec{P_j} = \alpha_j \vec{E_j}, \tag{3.1}$$

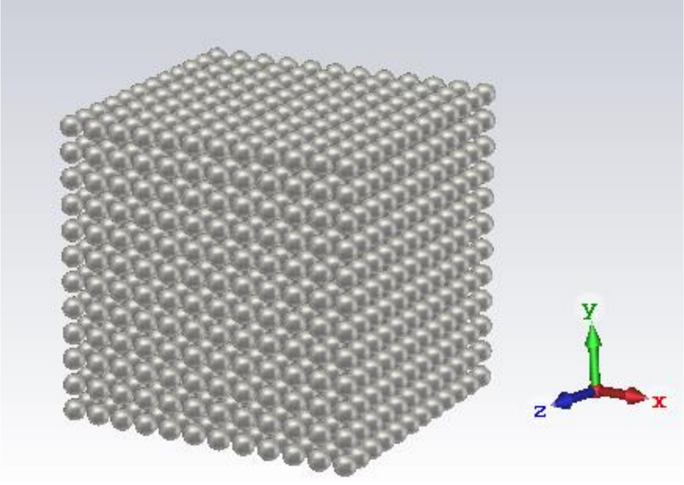

Figure 3.1. DDA model for a cubic inhomogeneity with small dipoles. A cubic inhomogeneous tissue of edge length 3mm is represented via equidistant (12 x 12 x 12) 1728 dipoles

where $\vec{E}_j$ is the total electric field at position $\vec{r}_j$ consisting of the incident electrical field and scattered fields by all other dipoles. α_j is the polarizability of dipole at position $\vec{r}_j$. $\vec{E}_j$ can be written as [69]:

$$\vec{E}_j = \vec{E}_{inc\,j} - \sum_{k \neq j} \bar{\bar{A}}_{jk}\,\vec{P}_k, \tag{3.2}$$

where $\vec{E}_{inc\,j}$ is the incident electrical field at $\vec{r}_j$, $\bar{\bar{A}}_{jk}$ is the tensor element representing the effect of the dipole at position $\vec{r}_k$ on the dipole at position $\vec{r}_j$. The dipole interaction tensor $\bar{\bar{A}}$ originates from the electric field Green's tensor of a radiating dipole, which is derived from vector Helmholtz equation in [71] and [72]. Each off-diagonal element of $\bar{\bar{A}}$ (i.e. j ≠ k) is a 3x3 matrix [62]:

$$\bar{\bar{A}}_{jk} = \frac{\exp(ikr_{jk})}{r_{jk}} \times \left[k^2\left(\hat{r}_{jk}\hat{r}_{jk} - \bar{\bar{I}}\right) + \frac{ikr_{jk}-1}{r_{jk}^2}\left(3\hat{r}_{jk}\hat{r}_{jk} - \bar{\bar{I}}\right)\right] \tag{3.3}$$

where k is the wave number of the medium, $r_{jk} = \left|\vec{r}_j - \vec{r}_k\right|$ and $\hat{r}_{jk} = (\vec{r}_j - \vec{r}_k)/\left|\vec{r}_j - \vec{r}_k\right|$ and $\bar{I}$ is unit dyad. The diagonal elements of $\bar{\bar{A}}$ dyadic matrix can be obtained from (3.1) and can be written as:

$$\bar{\bar{A}}_{jj} = \alpha_j^{-1} \tag{3.4}$$

As a result, formulation of scattering problem is simplified to finding the polarization of dipoles from a determined system of 3N linear equations [62]:

$$\sum_{k=1}^{N} \bar{\bar{A}}_{jk} \vec{P}_k = \vec{E}_{inc\,j} \tag{3.5}$$

In [69], the Clausius-Mossotti dipole polarizability was assigned:

$$\alpha_j^{CM} = \frac{3d^3}{4\pi}\left(\frac{\varepsilon_j - 1}{\varepsilon_j + 2}\right) = \frac{3d^3}{4\pi}\left(\frac{m_j^2 - 1}{m_j^2 + 2}\right) \tag{3.6}$$

where ε_j and m_j are the relative dielectric permittivity and refractive index of scatterer at location $\vec{r}_j$, and d is the spacing between dipoles in terms of incident electrical field wavelength. A more complete form, the Lattice Dispersion Relation (LDR) was derived in [73]:

$$\alpha_j^{LDR} = \frac{\alpha_j^{CM}}{1 + \frac{\alpha_j^{CM}}{d^3}\left[(b_1 + m^2 b_2 + m^2 b_2 S)(kd)^2 - \frac{2}{3} i (kd)^3\right]}, \tag{3.7}$$

b_1=-1.891531, b_2=0.1648469, b_3=-1.7700004, $S \equiv \sum_{j=1}^{3} \left(\hat{a}_j \hat{e}_j\right)^2$.
Here $\hat{a}_j$ and $\hat{e}_j$ are the unit vectors representing the direction and polarization of the incident electric field.

Once the E_{inc} is known and $\bar{\bar{A}}$ matrix elements are computed, polarization matrix P can be found, by utilizing iterative methods. The illustration of the matrix representation of Equation (3.5) is shown in Fig. 3.2. Krylov-space methods are widely used iterative methods in DDA calculations, such as Conjugate Gradient (CG) [74], Bi-Conjugate Gradient (Bi-CG) [75], Bi-Conjugate Gradient Stabilized

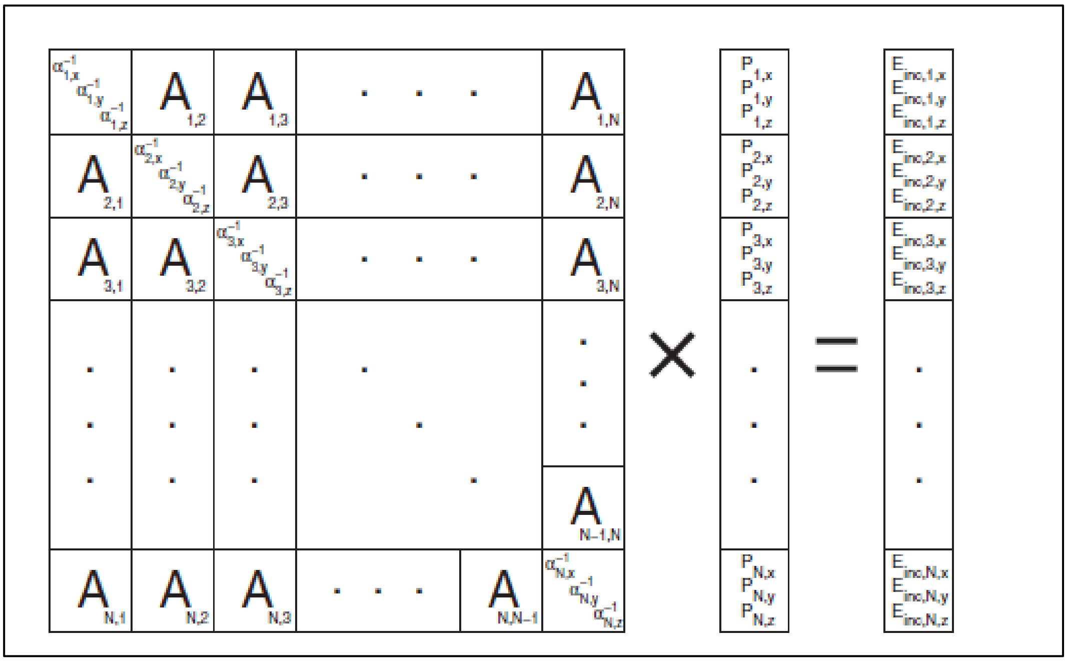
$\alpha_{1,x}^{-1}$ $\alpha_{1,y}^{-1}$ $\alpha_{1,z}^{-1}$
$A_{1,2}$
$A_{1,3}$
$A_{1,N}$
$A_{2,1}$
$A_{2,3}$
$A_{2,N}$
$A_{3,1}$
$A_{3,2}$
$A_{3,N}$
$A_{N-1,N}$
$A_{N,1}$
$A_{N,2}$
$A_{N,3}$
$A_{N,N-1}$
$P_{1,x}$ $P_{1,y}$ $P_{1,z}$
$P_{N,x}$ $P_{N,y}$ $P_{N,z}$
$E_{inc,1,x}$ $E_{inc,1,y}$ $E_{inc,1,z}$
$E_{inc,N,x}$ $E_{inc,N,y}$ $E_{inc,N,z}$

Figure 3.2. Formulation of scattering problem is simplified to finding the polarization of diploes from a determined system of 3N linear equations [67]. Once E_{inc} is known, the elements of $\bar{\bar{A}}$ can be calculated via equations (3.3) and (3.4).

(Bi-CGSTAB)[76], Generalized Minimal Residual (GMRES) [76] and Quasi-Minimal Residual (QMR) [76] and Generalized Product Type methods based on Bi-CG (GPBi-CG) [77]. FFT [78-79] and Fast Multipole Method (FMM) [71] are also utilized in DDA solution. The comparison of the methods for solving (3.5) is available in [70], [80-81], and [76]. In [80] it was shown that for small scaled problem QMR yielded faster solution with less memory requirement comparing to Bi-CG, CGSTAB and GMRES. In [76] QMR and Bi-CG showed better convergence than Bi-CGSTAB and GPBi-CG especially for high dielectric contrast scatterers, for $|m| > 2$, where m, is the refractive index and can be expressed as, $m = \sqrt{\frac{\varepsilon_{inhomogenety}}{\varepsilon_{breast\_tissue}}}$. As a result, in this study, QMR method is chosen as iterative method to find polarization matrix. The maximum iteration number is chosen as 60 and the maximum iteration number is chosen as 60 and the convergence tolerance is chosen as 10^{-7}. By adding up the field contributions from each dipole at point $\vec{r}_j$, the scattered field at any point $\vec{r}_i$ (relative to origin) can be found as [67]:

$$\vec{E}_{sca}(\vec{r}_i) = \sum_{j=1}^{N} \frac{e^{ikr_{ij}}}{r_{ij}} \left[k^2 \left(\hat{r}_{ij}\hat{r}_{ij} - \bar{\bar{I}} \right) + \frac{ikr_{ij}-1}{r_{ij}^2} \left(3\hat{r}_{ij}\hat{r}_{ij} - \bar{\bar{I}} \right) \right] . \vec{P}_j \tag{3.8}$$

where $r_{ij} = \left|\vec{r}_i - \vec{r}_j\right|$ and $\hat{r}_{ij} = (\vec{r}_i - \vec{r}_j)/\left|\vec{r}_i - \vec{r}_j\right|$.

Two main criteria for the validity of the DDA calculations are [62];

- $|m|kd \leq 1$ such that the spacing between dipoles d must be small compared to wavelength of the incident field;
- N, number of dipoles, must be chosen efficiently high so that the DDA model should resemble to original scatterer.

In [62], for $|m-1| \leq 1$, the DDA yielded good accuracies, that error remained in few percentages with the LDR polarizability. In this study, m values are chosen to satisfy $|m-1| \leq 1$ criteria in order to guarantee the accuracy of the solution.

The position of the dipoles can be updated via displacement data obtained at the instant when first maximum displacement occurs (T_{max}) and data obtained at the instant when first minimum displacement occurs (T_{min}). Performing three consecutive EM simulations with DDA, one for undisplaced (initial) dipole positions and two for updated dipole positions at, T_{max} and T_{min}, level of Doppler signal component can be found from simulated scattered electric fields via equation (2.15). The simulation steps of this study are summarized in Fig. 3.3.

3.3 Alternative DDA Based Simulation Method (1-Stage)

3.3.1 Semi-Analytical Solution for the Computation of Incident Electrical Field

The calculation of the incident electric field inside the breast tissue is implemented via the FDTD code in [50]. Alternatively, analytical formulation of electric field given in [82] for one layer can be employed in order to compute the incident electric field distribution inside homogeneous breast tissue from a rectangular open ended wave guide transmitting antenna. Transmitting antenna is assumed to be filled with oil in order to couple energy into homogeneous breast tissue as in [49]. The broad-wall (a) and narrow-wall (b) dimensions of antenna are selected to support the fundamental mode (i.e. TE_{10}) in the aperture of the antenna. On the boundary between breast tissue and antenna, outside the aperture of the antenna, electric field is zero assuming the aperture is radiating over an infinite ground plane [82]. TE_{10} mode electric field in $\hat{x}$ direction at the antenna aperture can be expressed as :

$$E_x(x, y, 0) = \sqrt{\frac{2}{ab}} cos\,\frac{\pi y}{a} \tag{3.9}$$

and the field in breast tissue is assumed to be TE to $\hat{y}$ [82] and vector potential can be written as :

$$\vec{F} = \psi \hat{y} \tag{3.10}$$

where ψ is scalar potential and $\hat{x}$, $\hat{y}$, $\hat{z}$ are the unit vectors in x, y and z directions respectively. The scalar potential can be formulated with plane wave spectral techniques in [82];

$$\psi = \frac{1}{(2\pi)^2} \sqrt{\frac{2a}{b}} \iint_{-\infty}^{\infty} \frac{4\pi j}{k_x k_z} \frac{\sin\left(\frac{k_x a}{2}\right) \cos\left(\frac{k_y b}{2}\right)}{\pi^2 - k_y^2 b^2} e^{-jk_z z} e^{-jk_x x} e^{-jk_y y}\, dk_x dk_y \tag{3.11}$$

where k_x ,k_y and k_z are the propagations constants in $\hat{x}$, in $\hat{y}$ and $\hat{z}$ directions respectively. k_z can be found from,

$$k_z = \begin{cases} \sqrt{\omega^2\mu_0\varepsilon_0\varepsilon_R - k_x^2 - k_y^2} & Re\{\omega^2\mu_0\varepsilon_0\varepsilon_R\} \geq k_x^2 + k_y^2 \\ -j\sqrt{k_x^2 + k_{y-}^2\omega^2\mu_0\varepsilon_0\varepsilon_R} & Re\{\omega^2\mu_0\varepsilon_0\varepsilon_R\} < k_x^2 + k_y^2 \end{cases} \tag{3.12}$$

where ω is the frequency of the microwave signal applied to transmitting antenna (rad/sec), μ_0 , is the permeability constant of free space since breast tissue is assumed non-magnetic, ε_0 is permittivity of free space and ε_R is the complex relative permittivity of breast tissue. The electric field inside the breast tissue can be derived from,

$$\vec{E} = E_x\hat{x} + E_z\hat{z} = -\nabla x\vec{F} \tag{3.13}$$

The electric field in $\hat{x}$ and $\hat{z}$ direction are calculated as [82]

$$E_x(x,y,z) = \frac{1}{(2\pi)^2}\sqrt{\frac{2a}{b}}\iint_{-\infty}^{\infty}\frac{4\pi}{k_x}\frac{\sin\left(\frac{k_x a}{2}\right)\cos\left(\frac{k_y b}{2}\right)}{\pi^2 - k_y^2 b^2}e^{-jk_z z}e^{-jk_x x}e^{-jk_y y}\,dk_x dk_y \tag{3.14}$$

and

$$E_z(x,y,z) = \frac{1}{(2\pi)^2}\sqrt{\frac{2a}{b}}\iint_{-\infty}^{\infty}\frac{4\pi}{k_z}\frac{\sin\left(\frac{k_x a}{2}\right)\cos\left(\frac{k_y b}{2}\right)}{k_y^2 b^2 - \pi^2}e^{-jk_z z}e^{-jk_x x}e^{-jk_y y}\,dk_x dk_y \tag{3.15}$$

Since the infinite summation is not possible for the numeric computation of electric field formulations in equations (3.14) and (3.15), an upper limit for summation is found so that contribution of higher order terms beyond the upper limit is negligible. $E_x(x,y,z)$ and $E_z(x,y,z)$ can be expressed as a finite summation plus asymptotic integration term as;

$$E_x(x,y,z) = \frac{1}{(2\pi)^2}\sqrt{\frac{2a}{b}}\iint_{-M}^{\mathrm{M}}\left(\frac{4\pi}{k_x}\frac{\sin\left(\frac{k_x a}{2}\right)\cos\left(\frac{k_y b}{2}\right)}{\pi^2 - k_y^2 b^2} - \theta\right)e^{-jk_z z}e^{-jk_x x}e^{-jk_y y}\,dk_x dk_y$$

$$+\frac{1}{(2\pi)^2}\sqrt{\frac{2a}{b}}\iint_{-\infty}^{\infty}(\theta)e^{-jk_z z}e^{-jk_x x}e^{-jk_y y}\,dk_x dk_y \tag{3.16}$$

$$E_z(x,y,z) = \frac{1}{(2\pi)^2}\sqrt{\frac{2a}{b}}\iint_{-M}^{\mathrm{M}}\left(\frac{4\pi}{k_z}\frac{\sin\left(\frac{k_x a}{2}\right)\cos\left(\frac{k_y b}{2}\right)}{\pi^2-k_y^2 b^2} - \beta\right)e^{-jk_z z}e^{-jk_x x}e^{-jk_y y}\,dk_x dk_y$$

$$+\frac{1}{(2\pi)^2}\sqrt{\frac{2a}{b}}\iint_{-\infty}^{\infty}(\beta)e^{-jk_z z}e^{-jk_x x}e^{-jk_y y}\,dk_x dk_y \qquad (3.17)$$

where θ and β are [83];

$$\theta = \int_{-a/2}^{a/2}\int_{-b/2}^{b/2}E_x(x,y,0)e^{jk_z z}e^{jk_x x}e^{jk_y y}\mathrm{d}x\mathrm{d}y \qquad (3.18)$$

$$\beta = -j\frac{k_x}{k_z}\int_{-a/2}^{a/2}\int_{-b/2}^{b/2}E_x(x,y,0)e^{jk_z z}e^{jk_x x}e^{jk_y y}\mathrm{d}x\mathrm{d}y \qquad (3.19)$$

The asymptotic integration parts of (3.16) and (3.17) can be represented by I_1 and I_2 respectively and are analytically expressed as [83];

$$I_1 \approx \frac{1}{2\pi}\cos\frac{\pi y}{b}\left[\tan^{-1}\frac{\frac{a}{2}+x}{z} + \tan^{-1}\frac{\frac{a}{2}-x}{z}\right] \qquad (3.20)$$

$$I_2 \approx \frac{-j}{2\pi}ln\frac{z^2+\left(\frac{a}{2}+x\right)^2}{z^2+\left(\frac{a}{2}-x\right)^2} \qquad (3.21)$$

For an open ended wave guide with aperture dimensions 24 mm and 14 mm respectively is assumed to be filled with sunflower oil similar to studies in [52]. The dielectric constant for breast tissue is chosen as a medium adipose (medium density) tissue, as $\varepsilon_R = 19.2$ and the conductivity is $\sigma = 0.46$ S/m [19]. The dielectric constant for the oil filling the waveguide antenna is chosen as 3.15 [52]. The tangential electric field, E_x, propagating inside the breast tissue is calculated the at position (0, 0, 10 mm). Integrating both k_x and k_y from -2500 rad/m to 2500 rad/m yielded convergence such that further extending the integration upper limits had negligible effect on computation. The error bound was below 0.12 %. Since the integrands in (3.14) have poles at $k_x = 0$ and $k_y = \pm\pi/b$, the integration boundaries for k_x are taken as [-2500, 2500]\{[-δ, δ]} and for k_y are taken as [-2500, 2500]\{[- π/b -δ, - π/b +δ] ∪[π/b -δ, π/b +δ] } where δ is 10^{-4} rad/m. The step size is chosen as 2 rad/m.

3.3.2 Adding Phase Terms to Polarization Matrix

In Chapter 3.2, the Doppler signal is obtained through three consecutive DDA simulations for each of *i*) its initial (undisplaced) position of tumor, *ii*) at the instant when maximum displacement of tumor occur (T_{max}) and *iii*) at the instant when minimum displacement of tumor occur (T_{min}). For the displaced tumors diploes were displaced with the displacement data obtained from mechanical simulation. However, the metric amount of displacements are in the order of microns and displacements are much smaller than wavelength (13.8 mm).

$$r_{ij} = \left|\vec{r}_i - \vec{r}_j\right| \approx r_{ij'} = \left|\vec{r}_i - \vec{r}_{j'}\right| \tag{3.22}$$

where $\vec{r}_{j'}$ is the new position of dipole after displacement. As a result, the effect of displacement on polarization can be added as a phase shift to the polarization of each dipole. Hence, for the calculation of the polarization vector for displaced cases, the phase terms found for undisplaced case can be added to polarization vector and only single DDA simulation is sufficient for calculation of the scattered electric field for displaced cases. The flow chart of the simulation steps in this study is summarized in Fig. 3.4.

3.4 Verification of the Proposed Simulation Method

In order to verify the proposed DDA based methods, forward EM problem of HMMDI is solved for both with the FDTD code in [49] and the proposed DDA based methods for same model. The acoustic and mechanical simulations are run only once and the results are utilized for all three methods (FDTD, 3-stage DDA and 1-stage DDA).

3.4.1 Acoustic and Mechanical Simulations

In the acoustic simulations, the HITU program is utilized and the simulation parameters for the FUS probe are chosen as given in Section 2.3.1. The FUS probe is assumed to be fixed throughout the simulations and similar to the experimental studies in [52]. 3 cm sunflower oil was assumed to be present between FUS probe and the upper surface of the breast phantom model so that the depth of the FUS probe focus can be adjusted to 3 cm inside the breast tissue from the surface. The ultrasound medium parameters are given in Table 3.1.

In the mechanical simulation model, a homogeneous breast phantom with 60 mm edge length was used (Fig.3.5). The position of the FUS transducer was fixed at 30 mm above from the upper surface of breast phantom so that the focus (with 6 cm focus depth) is kept constant at the symmetry center of the breast phantom. The medium was discretized with 1 mm x 1 mm x 1 mm cubic cells, and the computational grid was terminated with Dirichlet boundary conditions. Simulations were run up to 5300 iterations with 8.26-us time steps. In the simulations with tumor,a small and cubic tumor (with 3 mm edge length) was introduced inside the homogeneous breast tissue phantom. Its position was swept away from the focus of the FUS transducer with 1 mm step size along the x-and z-axis. The trajectory of tumor is shown in Fig. 3.5b. The tumor was swept 40 mm along A-B line in the lateral (x-axis) direction and then 40 mm along C-D line in axial (z-axis) direction. The midpoint of both A-B and C-D lines intersects at the focus of FUS transducer.

3.4.1 Electromagnetic Simulations

In the electromagnetic simulations, the problem was solved in two main stages. In the first stage, the incident electric field inside the medium was calculated, and in the second stage, the scattered fields from the displaced inclusion were calculated. In the incident field calculations, the transmitting and receiving antennas are modelled with

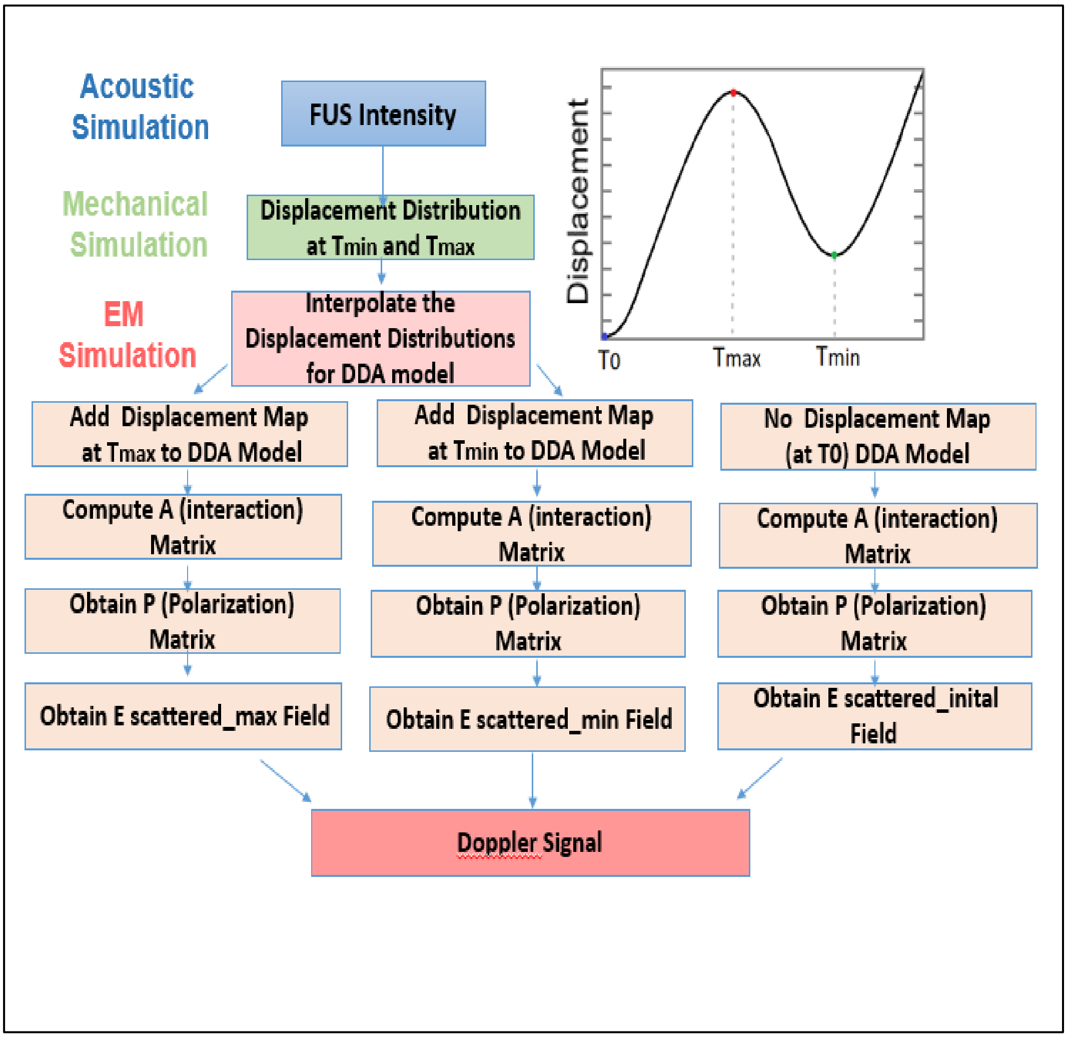
Acoustic Simulation
FUS Intensity
Mechanical Simulation
Displacement Distribution at Tmin and Tmax
EM Simulation
Interpolate the Displacement Distributions for DDA model
Displacement
T0
Tmax
Tmin
Add Displacement Map at Tmax to DDA Model
Add Displacement Map at Tmin to DDA Model
No Displacement Map (at T0) DDA Model
Compute A (interaction) Matrix
Compute A (interaction) Matrix
Compute A (interaction) Matrix
Obtain P (Polarization) Matrix
Obtain P (Polarization) Matrix
Obtain P (Polarization) Matrix
Obtain E scattered_max Field
Obtain E scattered_min Field
Obtain E scattered_inital Field
Doppler Signal

Figure 3.3 Simulation procedure for calculation of the Doppler signal component. In acoustic simulations, FUS intensity is calculated in order to find the acoustic radiation force. In mechanical simulations, displacement distribution of the tumor is obtained at the instances that maximum and minimum tumor displacements occur. In electrical simulations, tumor inside a homogeneous tissue is represented as an array of dipoles. The displacement data is interpolated in order to find the displacement data of each dipole. The positions of dipoles are updated according to the interpolated displacement map for three different time instants. The DDA simulations are done for each case and the Doppler signal is extracted.

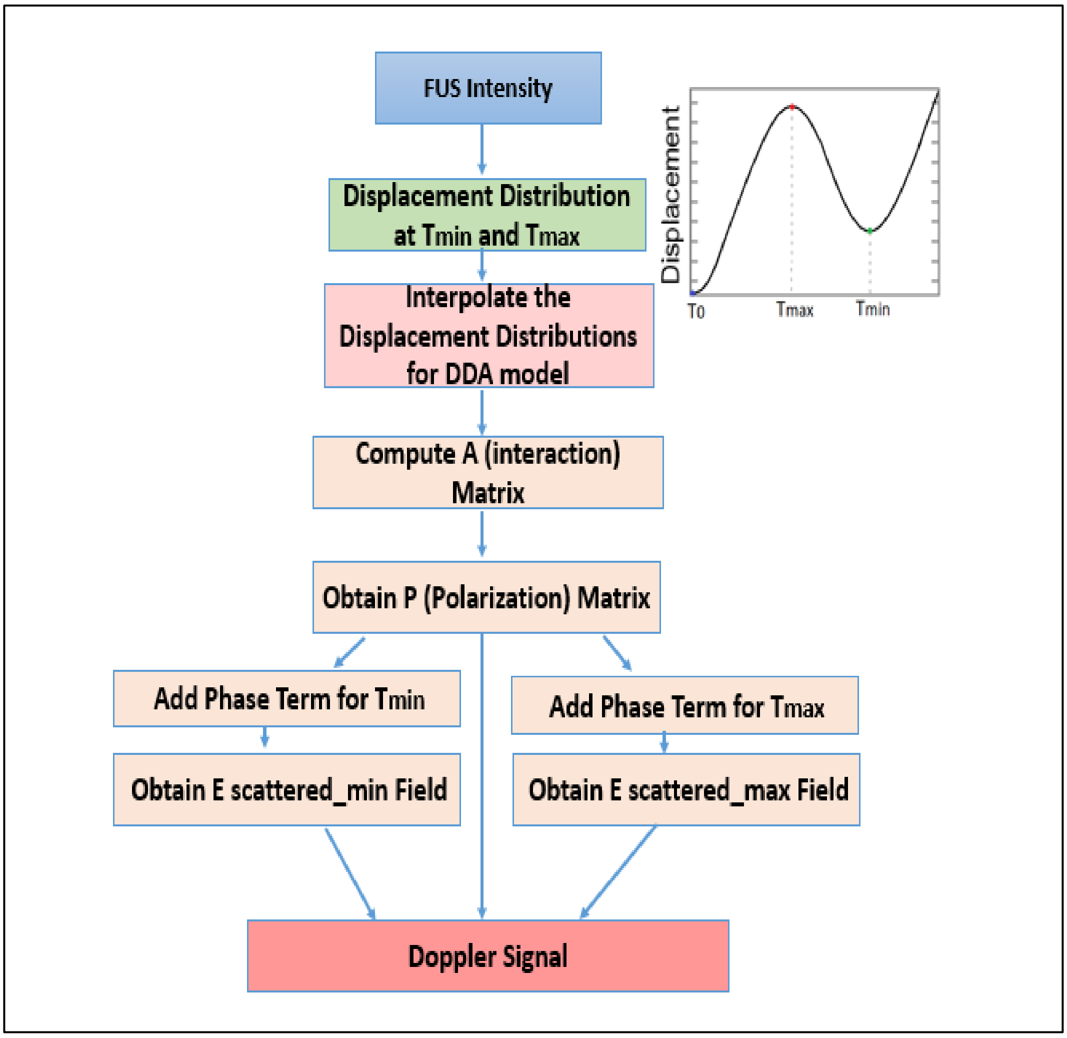
FUS Intensity
Displacement Distribution at Tmin and Tmax
Interpolate the Displacement Distributions for DDA model
Compute A (interaction) Matrix
Obtain P (Polarization) Matrix
Add Phase Term for Tmin
Add Phase Term for Tmax
Obtain E scattered_min Field
Obtain E scattered_max Field
Doppler Signal
Displacement
T0
Tmax
Tmin

Figure 3.4 Simulation procedure for single stage DDA simulation for the calculation of the Doppler signal. Apart from 3-stage DDA method, 1-stage DDA method the displacement data is added as phase term to the elements of the polarization of undisplaced case.

Table 3.1 Acoustic medium parameters utilized in HITU Simulation program.

Parameters	*Sunflower oil*	*Breast Tissue Phantom*
Speed of Sound (m/s)	1418 [84]	1553 [86]
Mass Density (kg/cm^3)	919 [84]	950 [87]
Attenuation at 1 MHz (dB/m)	5.28 [85]	150 [86]

open-ended waveguides with dimensions of 24 mm x 14 mm x 9 mm filled with sun flower oil (ε_R = 3.15). The antennas are placed in H plane orientation and 15 mm spacing is arranged on the bottom face of a homogeneous breast tissue model. Breast tissue and tumor were modelled as cubes with edge lengths 60 mm and 3 mm, respectively. The simulation model is shown in Fig 3.6. The breast tissue parameters were chosen to be of fibroglandular type tissue that relative permittivity (ε_R) and conductivity (σ) values were ε_R =23, σ=3.5 S/m [18], and Young's modulus of breast tissue was 3.8 kPa in the simulations [31], [32]. When the dielectric and elastic properties of the tumor and the breast tissue have low contrast, the received Doppler signal level tends to decrease and the numerical accuracy dominates in Doppler signal computation. In this study, we aimed to verify the performance of the proposed method for detection of tumor with low contrast in dielectric and elastic properties with respect to breast tissue. As a result, the relative permittivity and conductivity of the tumor are chosen as ε_R=26.9, σ=4.09 S/m, and Young modulus of tumor 5.7 kPa in the simulations. A CW microwave signal was applied to the transmitting antenna at 4.5 GHz.

The incident field distribution inside the homogenous breast model is analyzed with the FDTD code [38] only once. The calculated electric field inside the tissue when no tumor is utilized as incident field distribution map for scattering field calculation.

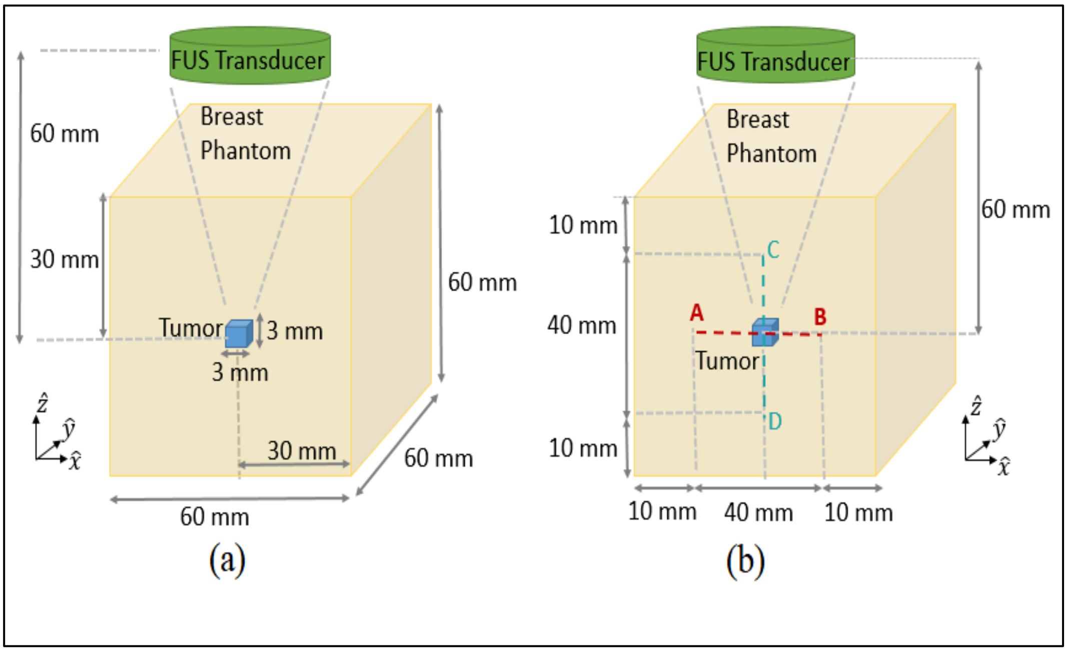
FUS Transducer
Breast Phantom
60 mm
30 mm
Tumor
3 mm
3 mm
60 mm
30 mm
60 mm
60 mm
$\hat{z}$
$\hat{y}$
$\hat{x}$
(a)
FUS Transducer
Breast Phantom
10 mm
C
40 mm
A
B
Tumor
D
10 mm
60 mm
$\hat{z}$
$\hat{y}$
$\hat{x}$
10 mm
40 mm
10 mm
(b)

Figure 3.5 Simulation model for the forward mechanical problem a) The tumor is modelled as a cube with 3 mm edge length and breast tissue phantom is modelled as a cube with 60 mm edge length. Position of the FUS transducer is fixed for mechanical simulations, its focus is at the symmetry center of the breast phantom b) In mechanical simulations, position of the tumor is swept by 1 mm grid steps along x axis (A-B line trajectory), then in z axis (C-D line trajectory) for a fixed FUS position. Both A-B and C-D tumor sweep line trajectories are 40 mm long and the lines intersect at the focus of the FUS transducer.

For 3-stage DDA method incident electric field is utilized from the incident field calculation from FDTD since our aim is to accelerate the calculation of scattered electric field. As for 1-stage DDA method, incident electric field is calculated via semi-analytic method in Chapter 3.3.1.

In the DDA based scattered field calculation, the tumor inclusion was implemented with small dipoles forming a cubic lattice array. The spacing between dipoles, *d*, was chosen as 250 µm, which is much smaller than wavelength of incident electrical field inside the breast tissue (i.e. 13.8 mm). The position of the dipoles representing the tumor were modified according to the displacement map obtained in the mechanical simulations (Fig. 3.7).The grid resolution of the displacement data in the mechanical FDTD simulations was 1 mm. However, the DDA tumor model consists of many small dipoles having an interelement distance much smaller than the mechanical simulation grid size. The displacement of each individual dipole was found by interpolating the displacement distribution obtained in the mechanical simulations.

In 3-stage DDA method, the positions of dipoles were updated using displacement data obtained at the first maximum (T_{max}) and the first minimum displacement instants (T_{min}) of the focal point. Performing three consecutive EM simulations with DDA, one for undisplaced (initial) dipole positions and two for updated dipole positions (T_{max} and T_{min}) the Doppler signal component can be calculated from simulated scattered electric fields from Eq. (2.15).

In 1-stage DDA method, the polarization matrix is calculated only for undisplaced case. For the displacement instants, the displacement data is added as phase term to the elements of the polarization of undisplaced case.

3.4.1 Simulation Results

The developed DDA based electromagnetic simulation methods for the HMMDI problem was verified by comparing the results with the FDTD based simulations presented in [52]. On a computer with Intel Xeon E5-2696 V4 processor, the simulation times of the EM problem for a single inclusion position were 122 minutes, 50.13 seconds and 18.54 seconds with the FDTD, 3-stage DDA and 1-stage DDA solvers, respectively. DDA based model enabled the calculation of the scattered electric field 164 times (via 3-stage DDA method and 398 times (via 1-stage DDA method) faster than the FDTD based model presented in [50].

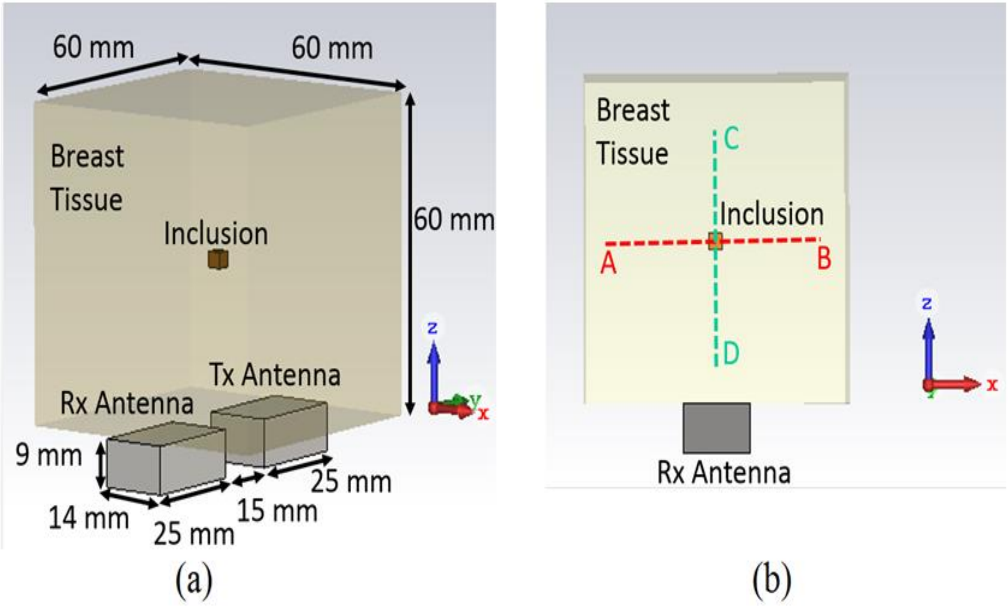
60 mm
60 mm
60 mm
Breast
Tissue
Inclusion
Tx Antenna
Rx Antenna
9 mm
14 mm
25 mm
15 mm
25 mm
z
y
x
(a)
Breast
Tissue
C
Inclusion
A
B
D
z
x
Rx Antenna
(b)

Figure 3.6 EM simulation geometry for receiving Doppler signal from a tumor inside breast tissue model a) Perspective view of simulation geometry: Breast tissue is modelled as cube with 60 mm edge length and tumor is modelled as a cube with edge length 3 mm. Transmit and receiving antennas are fixed at the bottom of breast tissue model b) Side view of simulation geometry: The tumor is moved along A-B line in x axis and C-D line in z axis. Both line trajectories are 40 mm long and they intersect at the focus of FUS transducer

The results of the developed DDA tools and FDTD method are presented in Fig. 3.8 and Fig. 3.9. In Figures 3.7a and 3.7b, the Doppler signal levels are given as a function of tumor position for 30 Hz vibration frequency along the axial (C-D line) and lateral (A-B line) directions, respectively. As expected, the maximum Doppler signal level (-114.2 dBm) was received, when tumor is at the focus of the FUS probe. In Figures 3.8a and 3.8b, the Doppler signal level is given as a function of tumor position for 60 Hz vibration frequency along the axial (C-D line) and lateral (A-B line) directions, respectively. The maximum Doppler signal level was -115.6 dBm in this case.

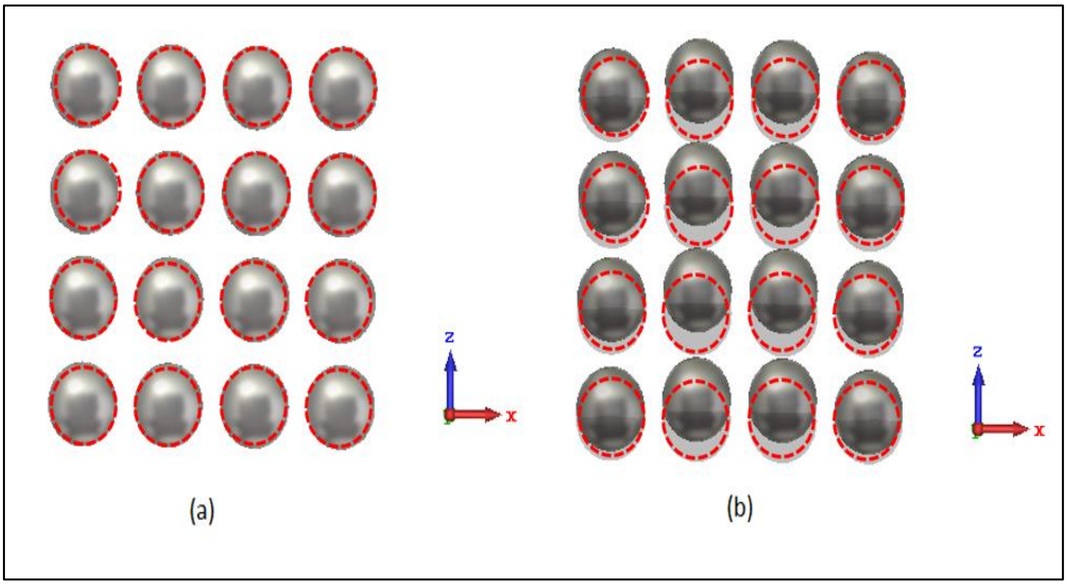

Figure 3.7 Updating the positions of the dipoles with displacement data obtained in mechanical simulations. This figure illustrates the a) side view of the DDA model of a cubic tumor for the initial position (no vibration) which is represented by equally spaced dipoles. Their initial positions are encircled with dashed red circles. b) Dipoles are reoriented by shifting each dipole according to the interpolated displacement data. New positions of the dipoles are shown with dark grey color and shift from their initial (undisplaced) positions are shown with light grey colored shadow encircled with red dashed circles.

When the focus of FUS probe coincides with the tumor, for 30 Hz vibration frequency, the difference of the maximum levels of received Doppler signals calculated via FDTD and 3-stage DDA method is 0.18 dB, whereas the difference is 0.71 dB for the results obtained from FDTD and 1-stage DDA method. On the other hand, for 60 Hz vibration frequency, the difference between maximum signal levels computed via FDTD and 3-stage DDA method is 0.27 dB and as for the comparison of the levels between FDTD and 1-stage DDA method, the difference is 1.37 dB. The computational error increases for 1-stage DDA method for higher vibration frequencies. Since the displaced region width decreases with higher vibration frequencies, the interpolation errors become more dominant.

The decrease in the amplitude of the received Doppler signal level compared to the signal level for the tumor position at the focus of FUS transducer is defined as the Rate of Decrease (ROD) metric. As seen in Fig. 3.8 and Fig. 3.9, the Doppler signal level decreases as the position of the tumor moves away from the focus of the FUS probe. The ROD for the lateral axis scan of tumor is much higher than that of the axial axis scan, suggesting higher resolution in the lateral direction. Moreover, half maximum widths at 60 Hz vibration frequency are smaller than the half maximum widths at 30 Hz frequency.

3.5 2D HMMDI Scan Simulations With The 1-stage DDA Based Method

HMMDI scan simulation of a 27 mm^3 cubic tumor is performed with the proposed 1-stage DDA based simulation method. The simulation geometry is shown in Fig. 3.10. A Focused Ultrasound (FUS) probe is located over breast phantom. The breast phantom and tumor are modelled as cubes with dimensions of 60 mm x 60 mm x 60 mm and 3 mm x 3 mm x 3 mm respectively. The simulation properties of open ended wave-guides, FUS probe, breast and tumor are chosen same from Chapter 3.3.

The volume center of the tumor is located 30 mm below the upper surface of the breast phantom (Fig. 3.10). 2D HMMDI of the tumor is obtained in two orthogonal planes as seen in Fig. 3.10a and Fig. 3.10b. In both scans the, the position of FUS probe is altered to scan the 40 mm x 40 mm area with 1 mm grid resolution. The planes of 2D scan lay in lateral (xy) and axial (xz) directions respectively and the planes intersect at the volume center of the cubic tumor.

2D HMMDI scan results of cubic tumor with 3 mm edge length in lateral and axial axes are given in Fig. 3.11. The boundaries of the scanned tumor is presented with red square. The results show that the tumor is imaged larger than its original size for the 2D scan in axial axes. However, for the lateral axes scan, the received image

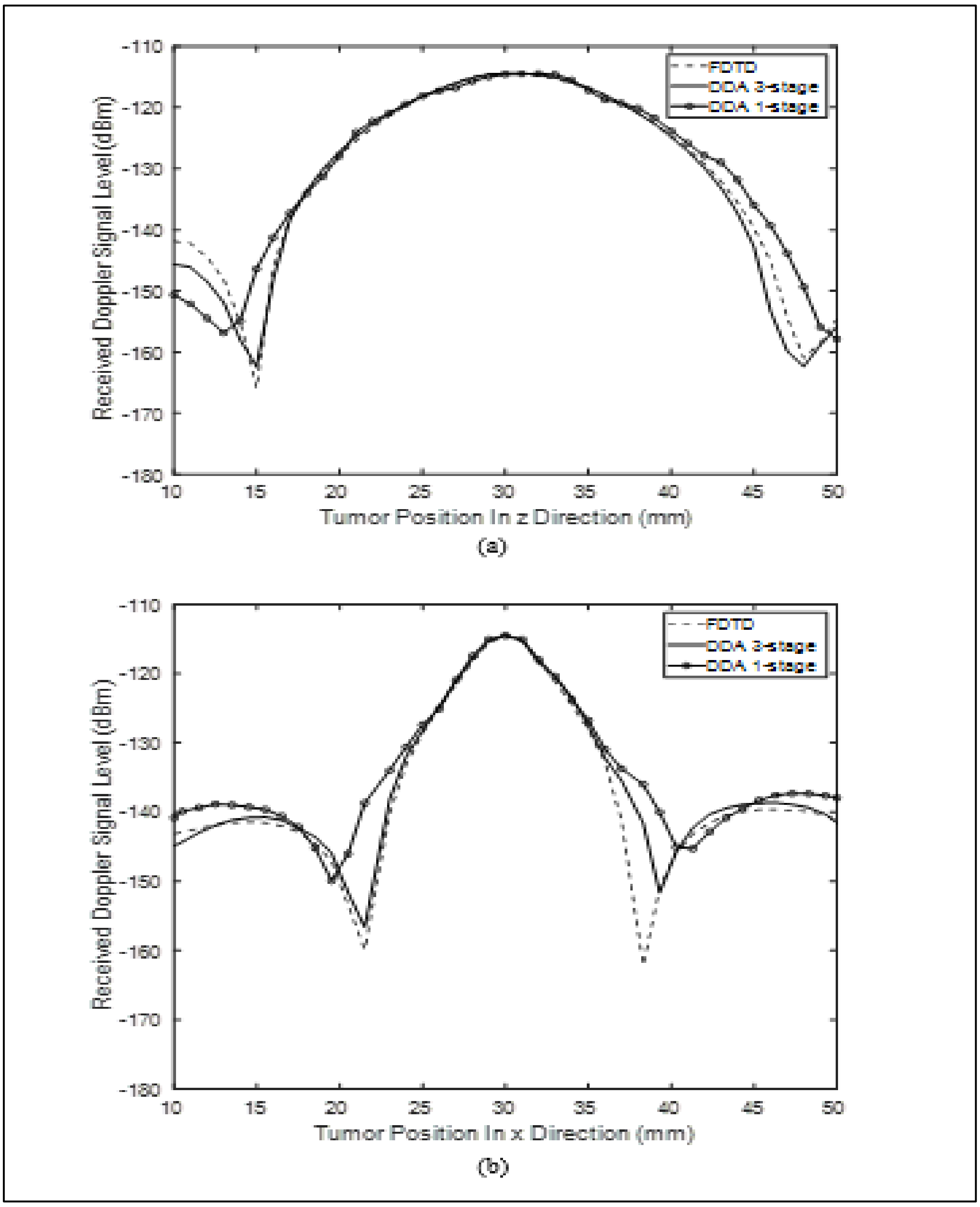

Figure 3.8 Comparison of EM simulation results computed from FDTD based code [50] and DDA based proposed EM simulation codes for cubic tumor with 3 mm edge length. For 30 Hz vibration frequency the tumor is swept along a) C-D line (along z axis) b) A-B line (along x axis)

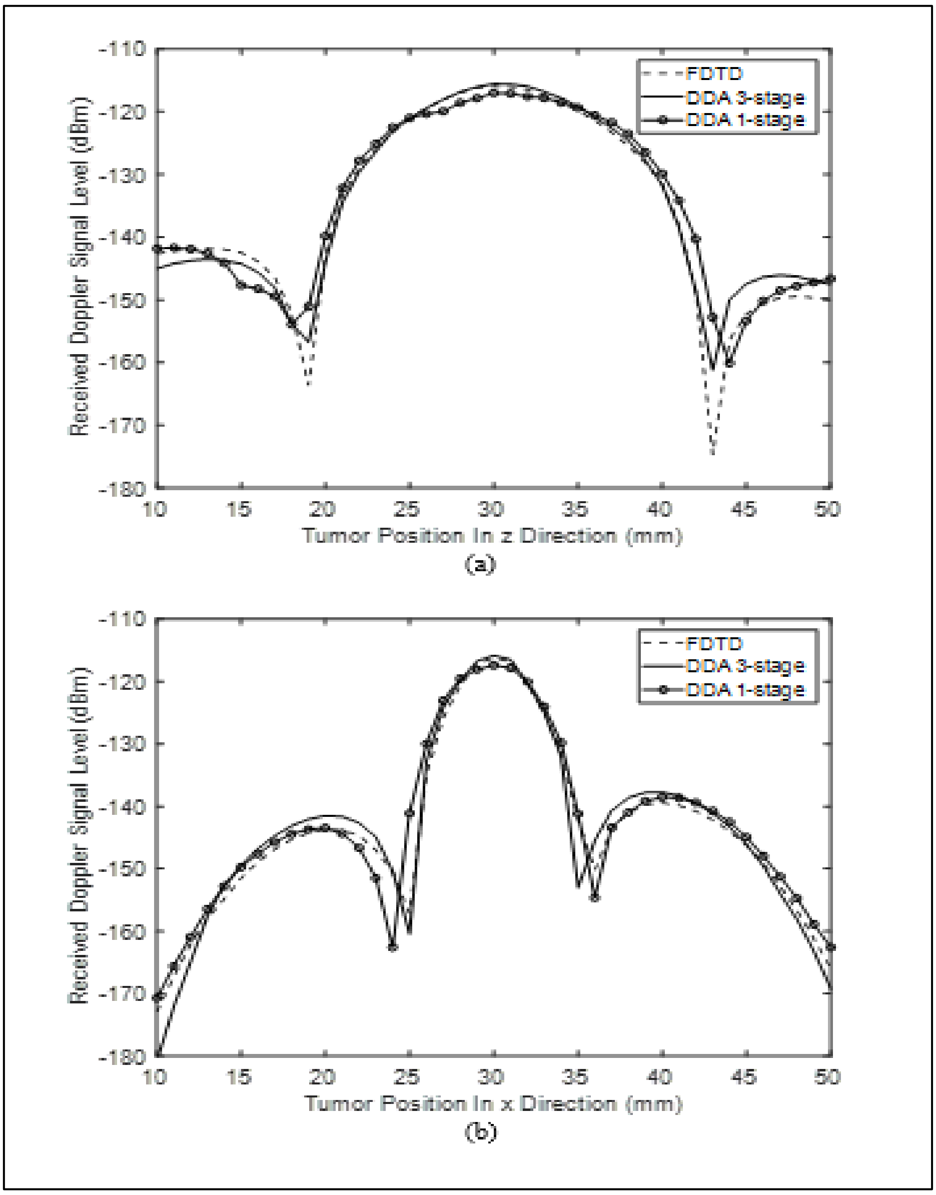

Figure 3.9 Comparison of EM simulation results computed from FDTD based code [50] and DDA based proposed EM simulation codes for cubic tumor with 3 mm edge length. For 60 Hz vibration frequency the tumor is swept along a) C-D line (along z axis) for 60 Hz vibration frequency b) A-B line (along x axis)

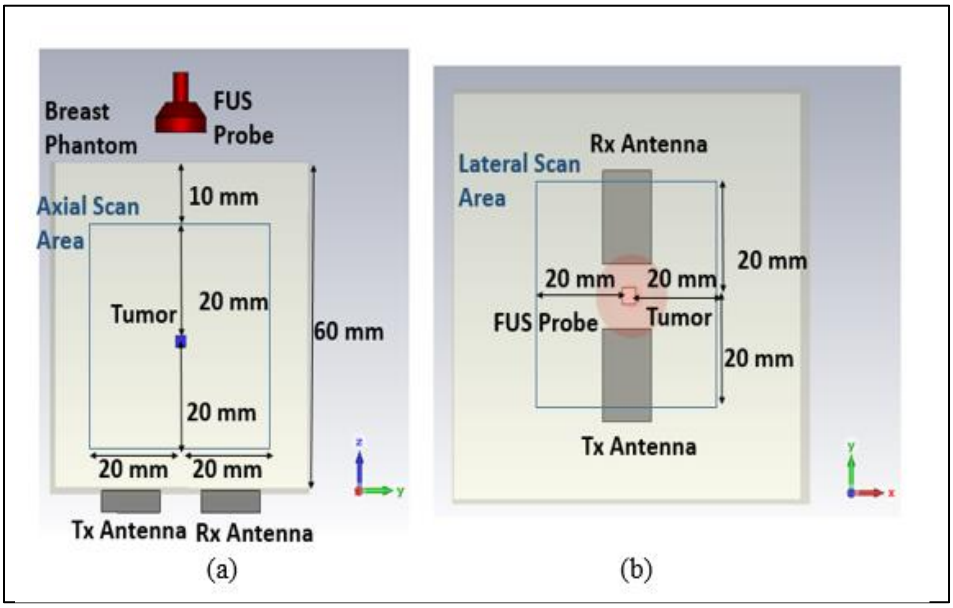
Breast Phantom
FUS Probe
Axial Scan Area
10 mm
Tumor
20 mm
60 mm
20 mm
20 mm
20 mm
Tx Antenna
Rx Antenna
(a)
Lateral Scan Area
Rx Antenna
20 mm
20 mm
20 mm
FUS Probe
Tumor
20 mm
Tx Antenna
(b)
z
y
x

Figure 3.10 2D HMMDI scan simulation model: a small cubic tumor inside a medium adipose content breast tissue phantom (a) 2D scan model for the axial axes (yz), focus of the FUS probe is scanned over Axial scan area with 1 mm grid resolution (b) 2D scan model for the lateral axes (xy), focus of the FUS probe is scanned over Axial scan area with 1 mm grid resolution.

resembles to the original tumor. In Fig. 3.12, the displacement data of the tumor at T_{max} instant when the focus of the FUS probe coincides with the volume center of the tumor is given in lateral and axial directions. It is observed that the image of the tumor has strong correlation with the displacement map.

As the vibration frequency decreases the DRW (half beamwidth where maximum displacement occurs) increases. For 30 Hz vibration frequency, the DRW in axial axis is large with respect to tumor size. Hence the tumor is imaged larger than its original size in axial axes. On the other hand, the DRW in lateral axis is much smaller than DRW in axial axis, 2D HMMDI scan of the tumor in lateral axis yields better tumor resolution.

3.6 3D HMMDI Scan Simulations For Two Different Tumor Sizes With The 3-stage DDA Based Method

In this section, detection of a tumor inside a homogeneous breast phantom model is studied as a function of tumor size. The position of the tumor is fixed inside a homogeneous breast phantom and the FUS Probe is scanned over the breast tissue with 1 mm spacing. A homogeneous high adipose breast tissue phantom is modeled as a square prism with dimensions of 80 mm x 80 mm x 60 mm. The center of the tumor is placed at 30 mm below the upper surface of the breast tissue. The acoustic coupling medium between the breast phantom and the FUS Probe is assumed as sunflower oil. Since the position of the FUS Probe is altered during the scan, for each axial scan position (with 1 mm step size) in z direction, the acoustic radiation intensity distribution inside the breast phantom is calculated. Similar to the experimental studies [50-52], the peak pressure of FUS Probe is 1.23 MPa. In the DDA based simulation model, the antennas and the skin layer are not included in the simulation model. The normalized (unit) incident field (y polarized) is injected into the simulation and propagation direction is aligned with the positions of the antenna locations in previous simulation and the focus of FUS Probe. The operation frequency of CW microwave signal is 4.5 GHz. The dielectric constant for breast tissue is chosen as a medium adipose (medium density) tissue, as $\varepsilon_R = 19.2$ and the conductivity is $\sigma = 0.46$ S/m [19]. The elastic constant, Young modulus of the breast tissue was chosen as, E=3.8 kPa [31]. The tumor is modelled with dielectric constant, $\varepsilon_R = 44$; conductivity $\sigma = 3.86$ S/m, and elastic constant Young modulus E=15 kPa.

The FUS probe is swept along a volume of 30 mm (in x-direction) x 30 mm (in y-direction) x 45 mm (in z-direction) keeping the tumor at the center. The model for scanning and the volume of the scanned region in three orthogonal views (xz, xy and xz) are shown in Fig. 3.13. The simulations are made for cubic tumors with edge lengths of 3 mm and 6 mm respectively. The distribution of the Doppler signal in three orthogonal views are shown in Fig. 3.14-Fig 3.16 for a cubic tumor with 3 mm edge length, and in Fig. 3.17-Fig 3.19 for a cubic tumor with 6 mm edge length. For

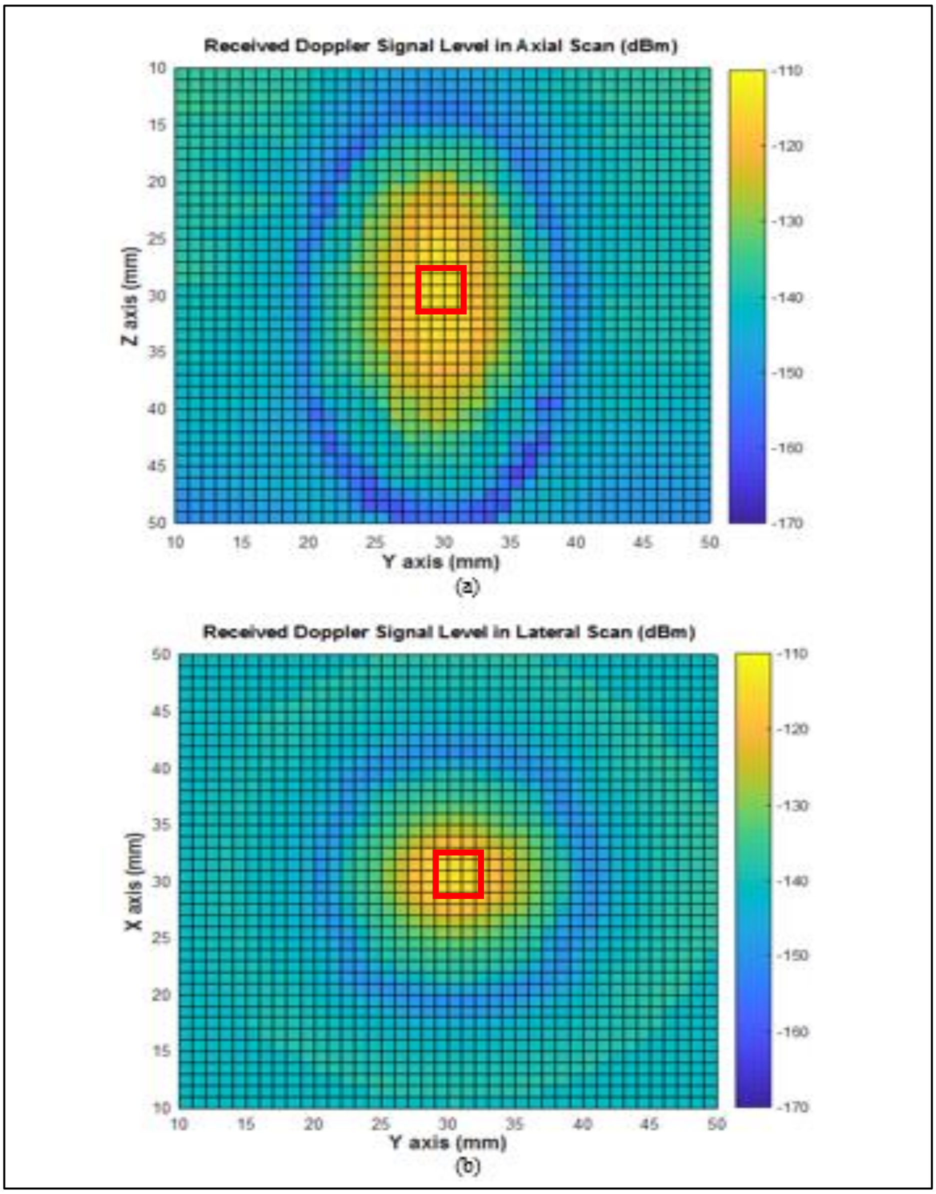

Figure 3.11 2D HMMDI scan simulation model: a small cubic tumor inside a medium adipose content breast tissue phantom. Original tumor is represented with red square (a) 2D scan model for the axial axes (yz), focus of the FUS probe is scanned over Axial scan area with 1 mm grid resolution (b) 2D scan model for the lateral axes (xy), focus of the FUS probe is scanned over Axial scan area with 1 mm grid resolution.

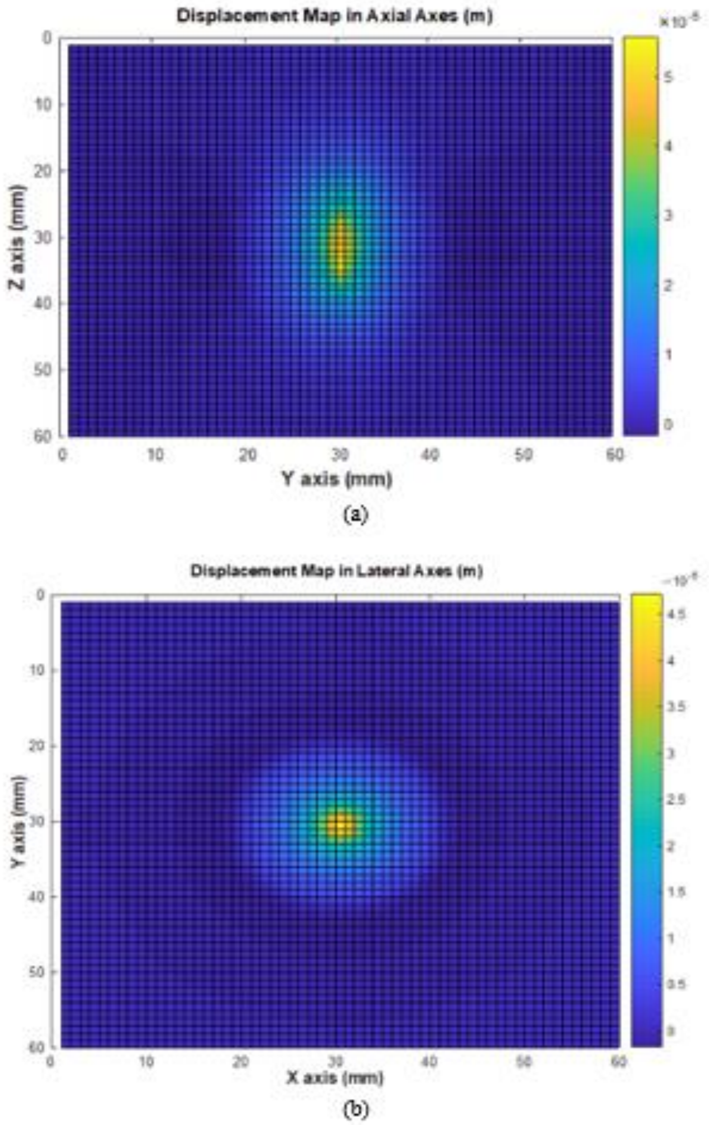

Figure 3.12 The displacement data of the tumor at Tmax instant when the focus of the FUS probe coincides with the volume center of the tumor is given in a) axial and b) axial directions

the cubic tumor with edge length of 3 mm, the maximum level of the received Doppler signal is -61.7 dBm when the focus of FUS probe coincides with the center of the tumor. As the FUS probe moves away from the tumor by 5 mm and 10 mm in axial (z) axes, the received Doppler signal drops approximately by 3 dB and 10 dB respectively. On the other hand, if FUS probe moves away from the tumor by 5 mm and 10 mm in lateral (x and y) axes, the received Doppler signal drops more than 10 dB and 25 dB, respectively. The rate of decrease of the Doppler signal in axial is less than that of in the lateral (xy) directions, owing to the larger half power intensity beamwidth of the FUS probe in the axial direction.

For the cubic tumor with edge length of 6 mm, the maximum level of the received Doppler signal is -65.4 dBm, when the focus of the FUS probe coincides with the center of the tumor. As the FUS probe moves away from the tumor by 5 mm and 10 mm in axial (z) axes, the received Doppler signal drops approximately by 2 dB and 6 dB respectively. On the other hand, if FUS probe moves away from the tumor by 5 mm and 10 mm in the lateral (x and y) axes, the received Doppler signal drops more than 8 dB and 20 dB, respectively. The difference between the peak amplitude of the received Doppler signal for two tumor sizes is about 4.7 dB.

The vibration of the edges of the smaller tumor is larger than the vibration of larger tumor. As the size of small tumor is within the half power intensity beamwidth of the FUS probe, whole tumor is displaced with the FUS probe excitation. On the other hand, for large tumor the intensity of the acoustic radiation decreases on the edges of large tumor, yielding less displacement.

For larger tumor, the received Doppler signal graphs have a plateau for the peak values; which is related to the size of the tumor. The decrease of Doppler signal starts when the FUS probe is moved 3 mm away from the center of the tumor. This point coincides where the focus of the FUS probe is at the edges of the tumor, beyond which tumor is out of the focus of the FUS probe. However, for smaller tumor the decrease in Doppler signal starts when the FUS probe is moved by 1 mm away from

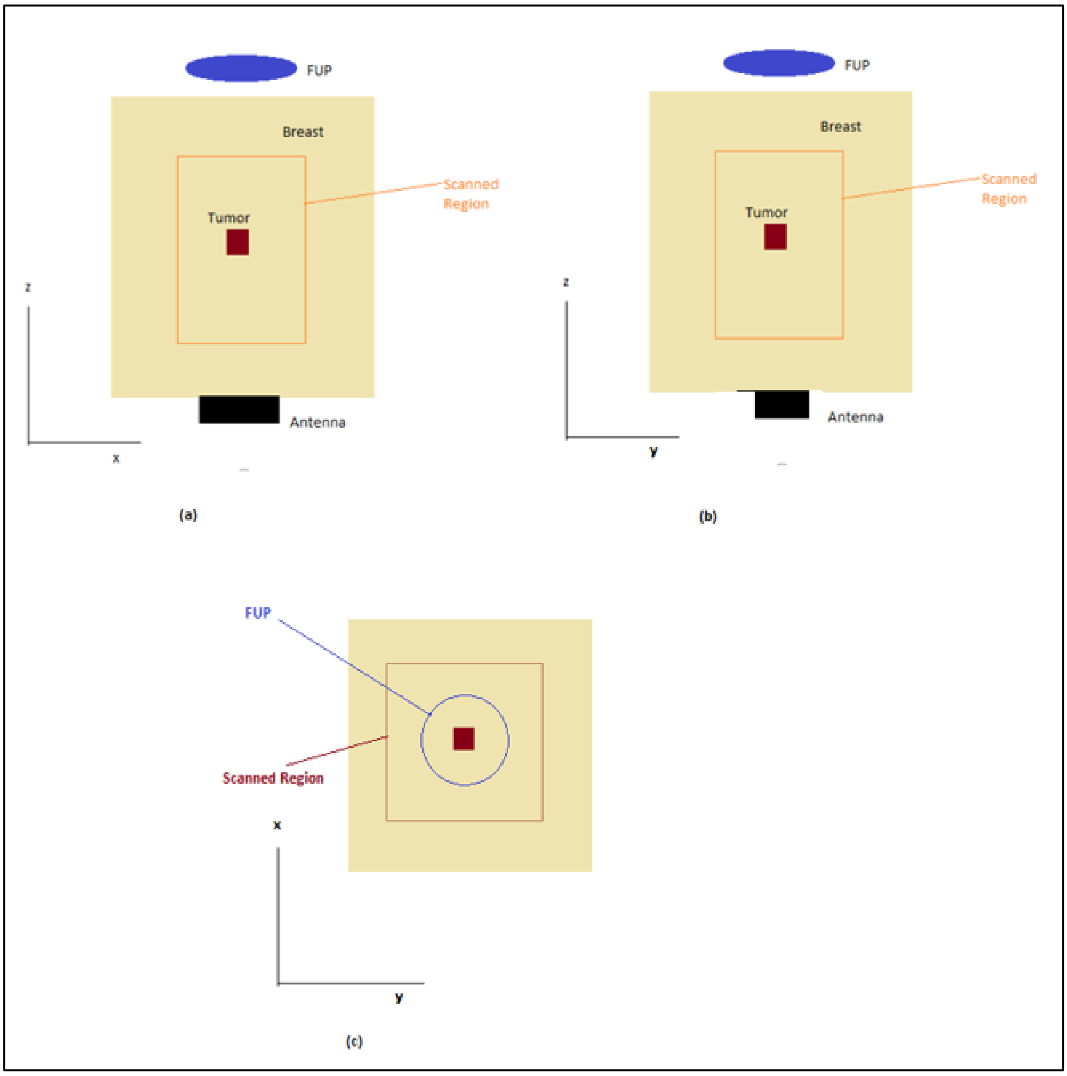
FUP
Breast
Scanned Region
Tumor
z
Antenna
x
(a)
FUP
Breast
Scanned Region
Tumor
z
Antenna
y
(b)
FUP
Scanned Region
x
y
(c)

Figure 3.13 The scanned area for a tumor of fixed position in the HMMDI simulations performed with DDA method a) xz view b) yz view c) xy view.

the center of the small tumor. The rate of decrease of the Doppler signal when the FUS probe moves away from the edge of the tumor has similar characteristics for the two scans.

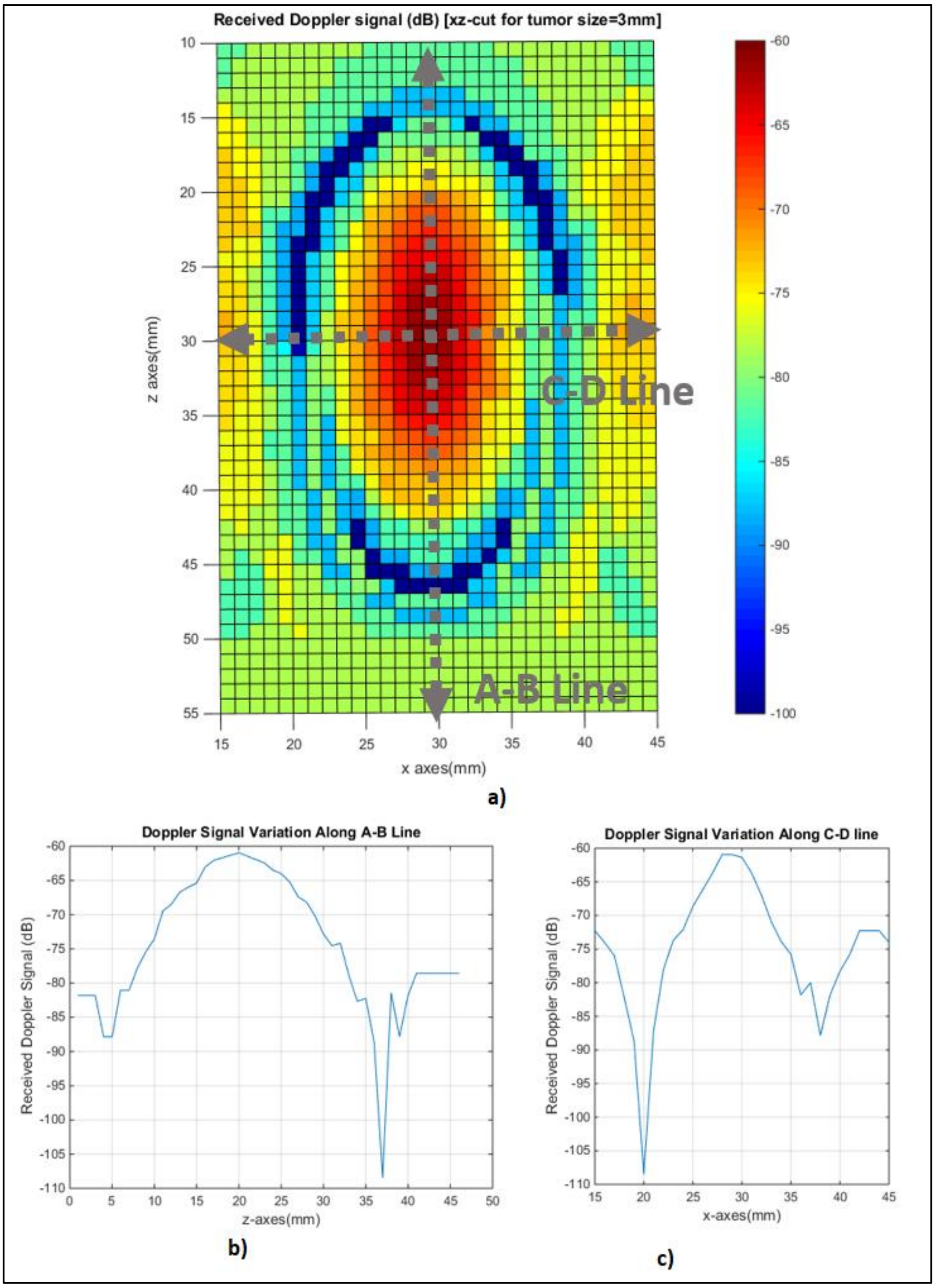

Figure 3.14 The distribution of the normalized received Doppler signal from a 3 mm cubic tumor a) 2D xz view b) variation along A-B line c) variation along C-D line

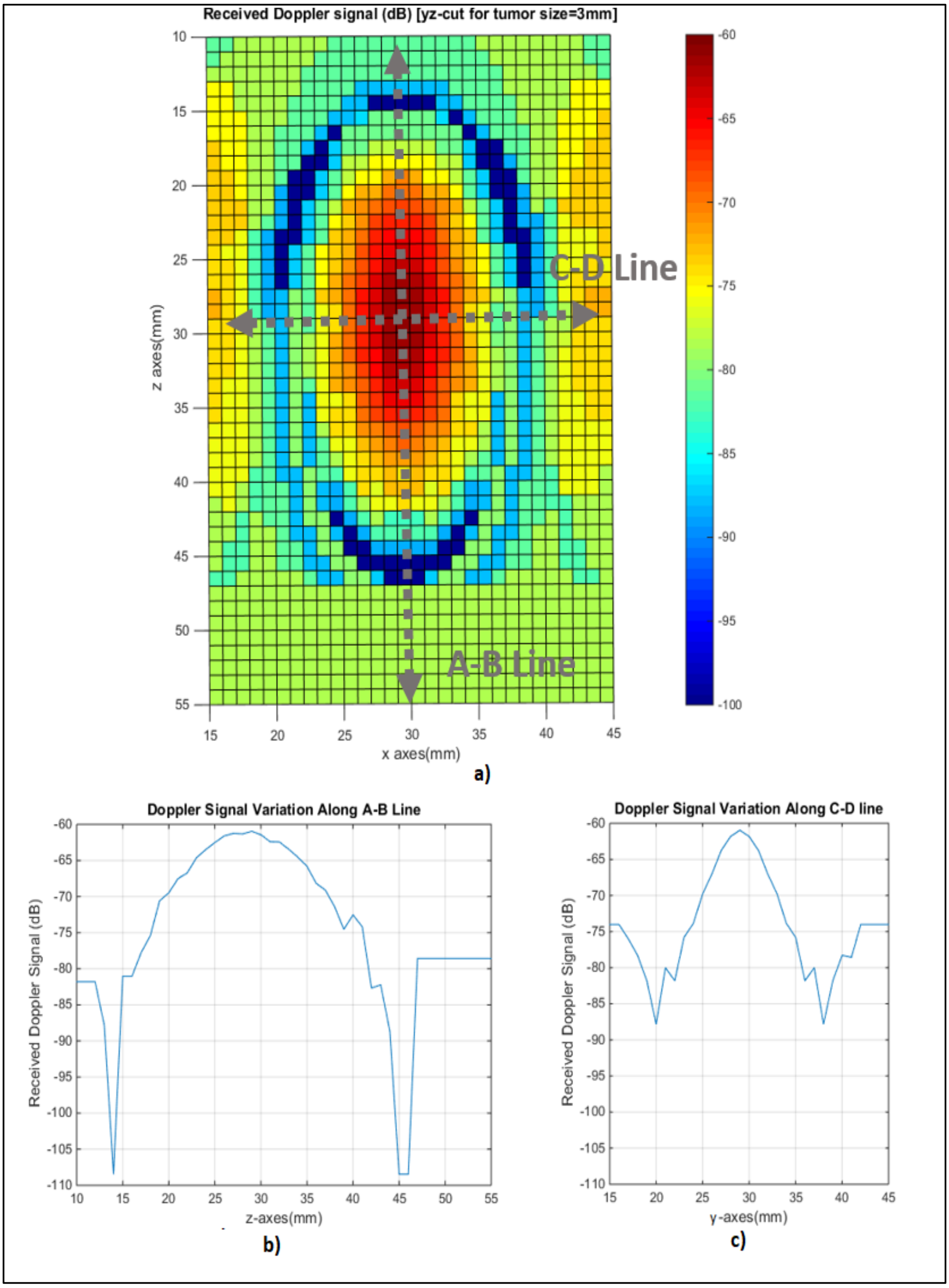

Figure 3.15. The distribution of the normalized received Doppler signal from a 3 mm cubic tumor a) 2D yz view b) variation along A-B line c) variation along C-D line.

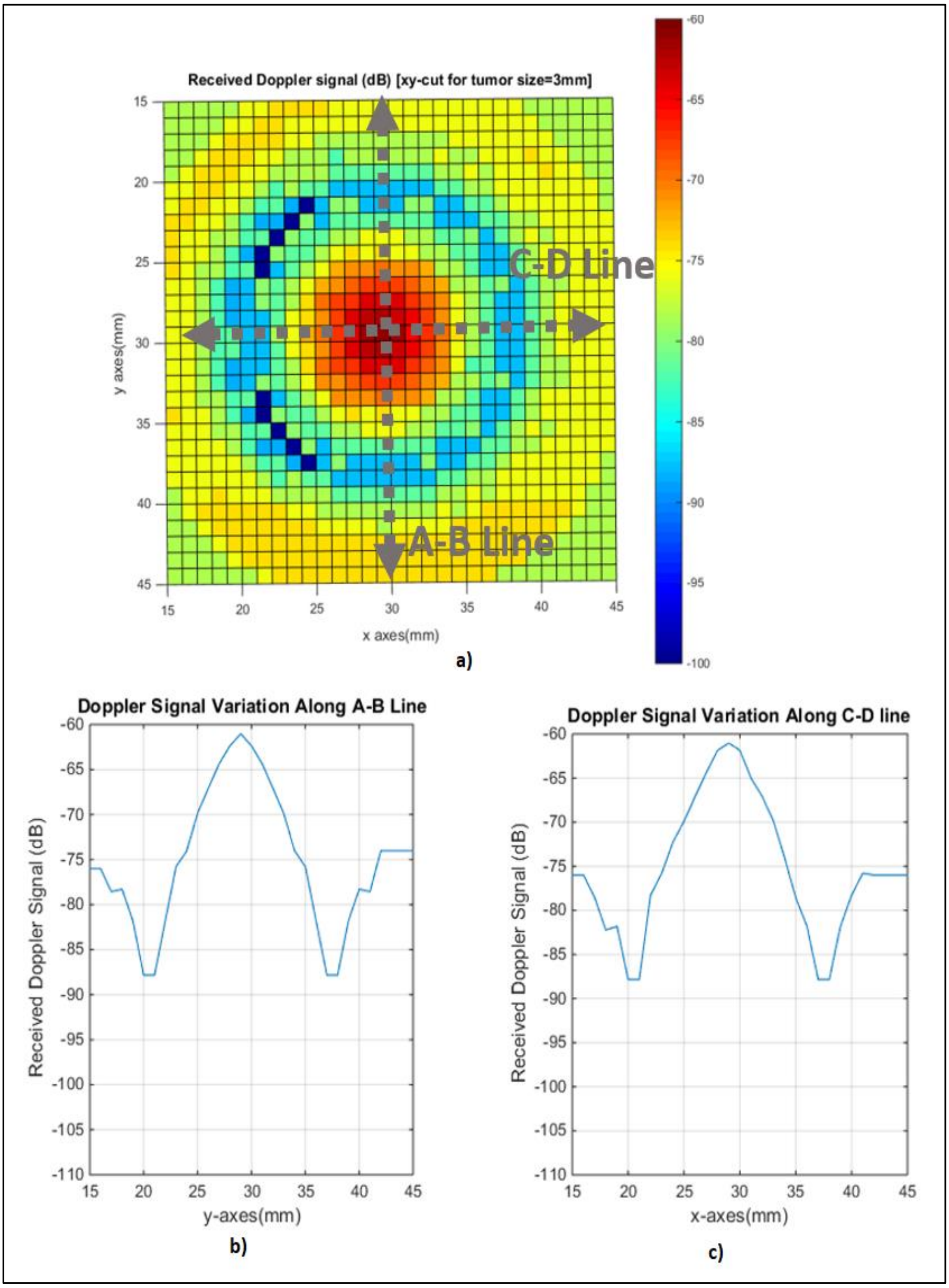

Figure 3.16. The distribution of the normalized received Doppler signal from a 3 mm cubic tumor a) 2D xy view b) variation along A-B line c) variation along C-D line.

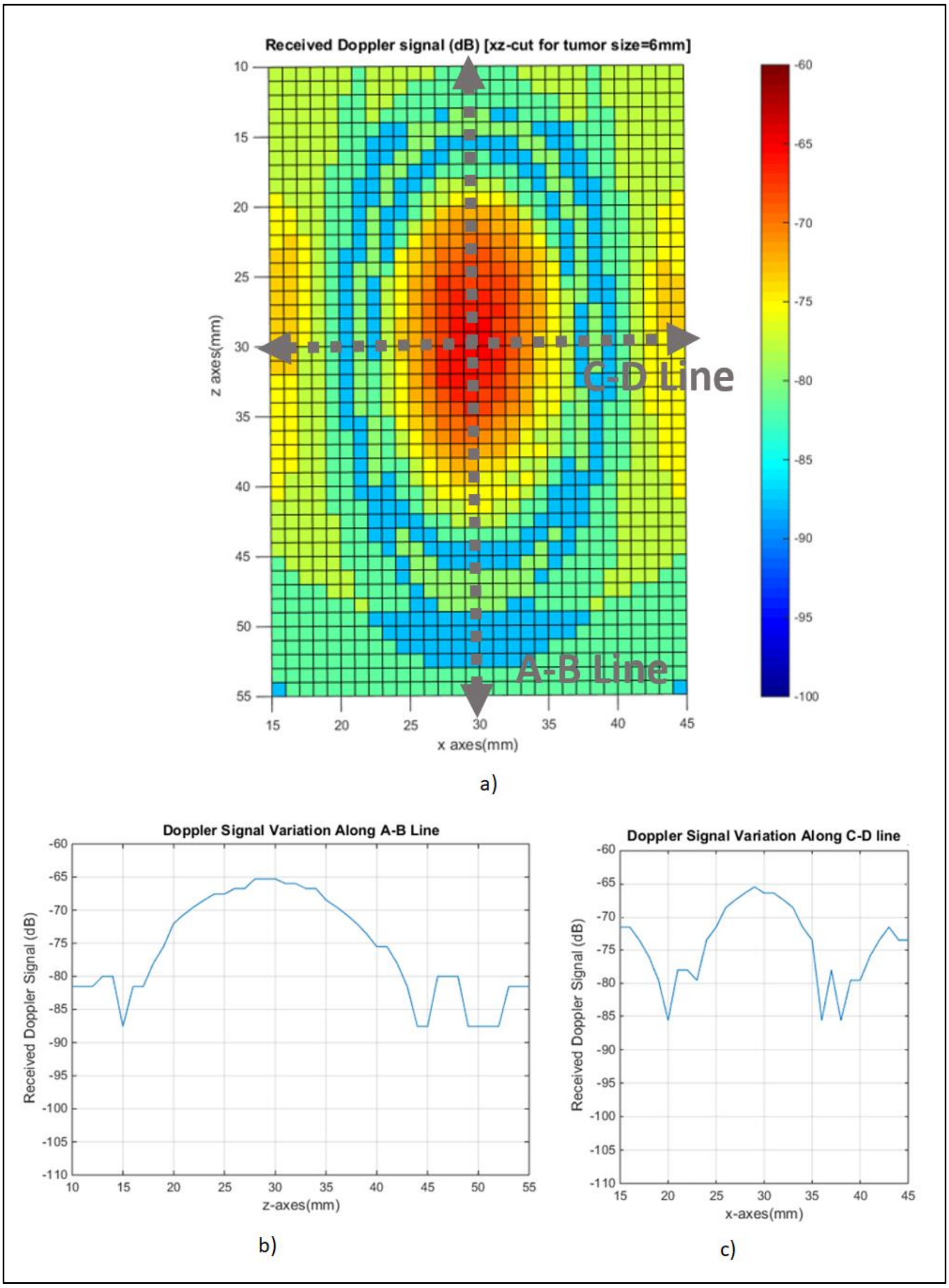

Figure 3.17. The distribution of the normalized received Doppler signal from a 6 mm cubic tumor a) 2D xz view b) variation along A-B line c) variation along C-D line.

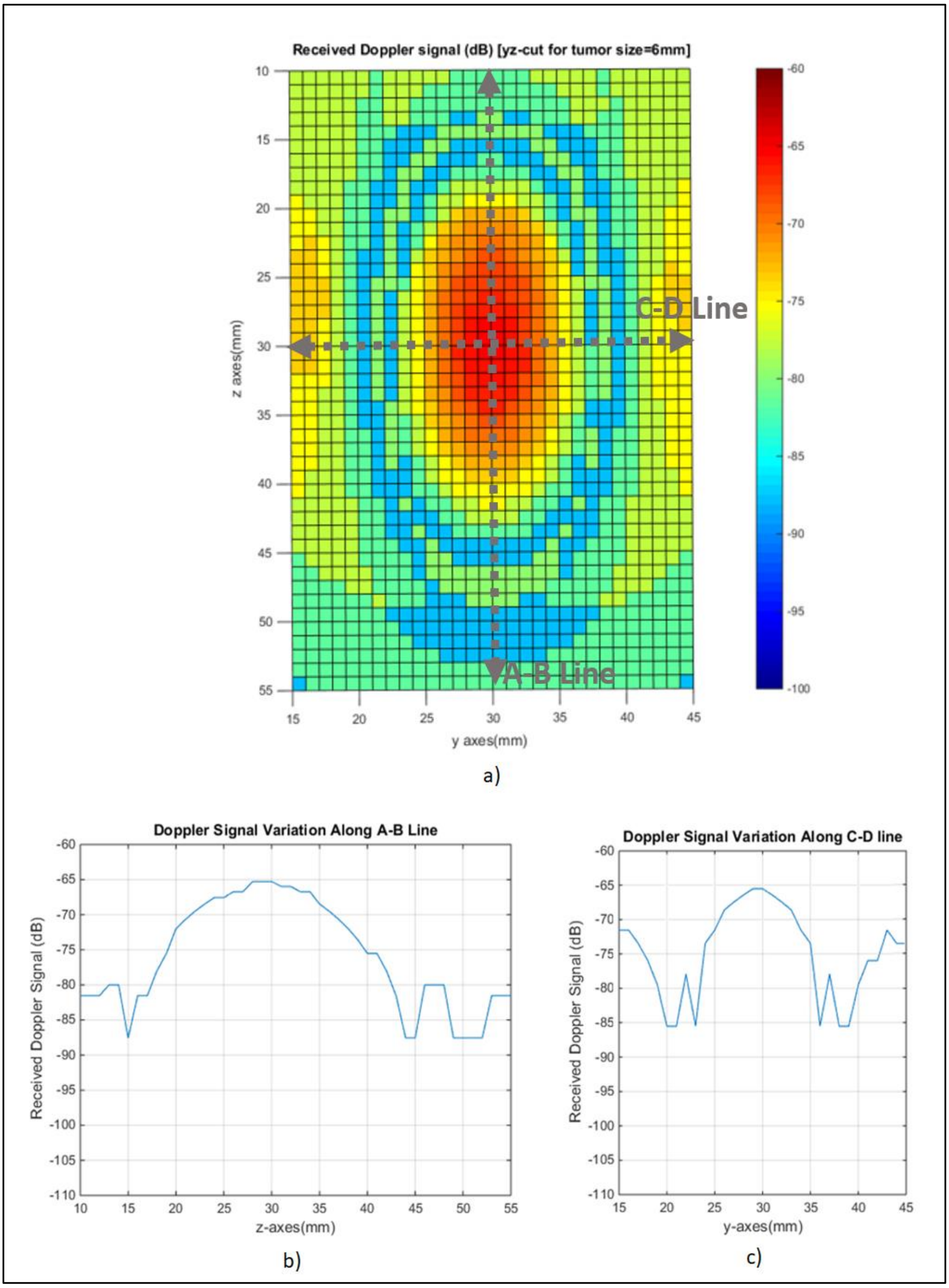

a)

b)

c)

Figure 3.18. The distribution of the normalized received Doppler signal from a 6 mm cubic tumor a) 2D yz view b) variation along A-B line c) variation along C-D line.

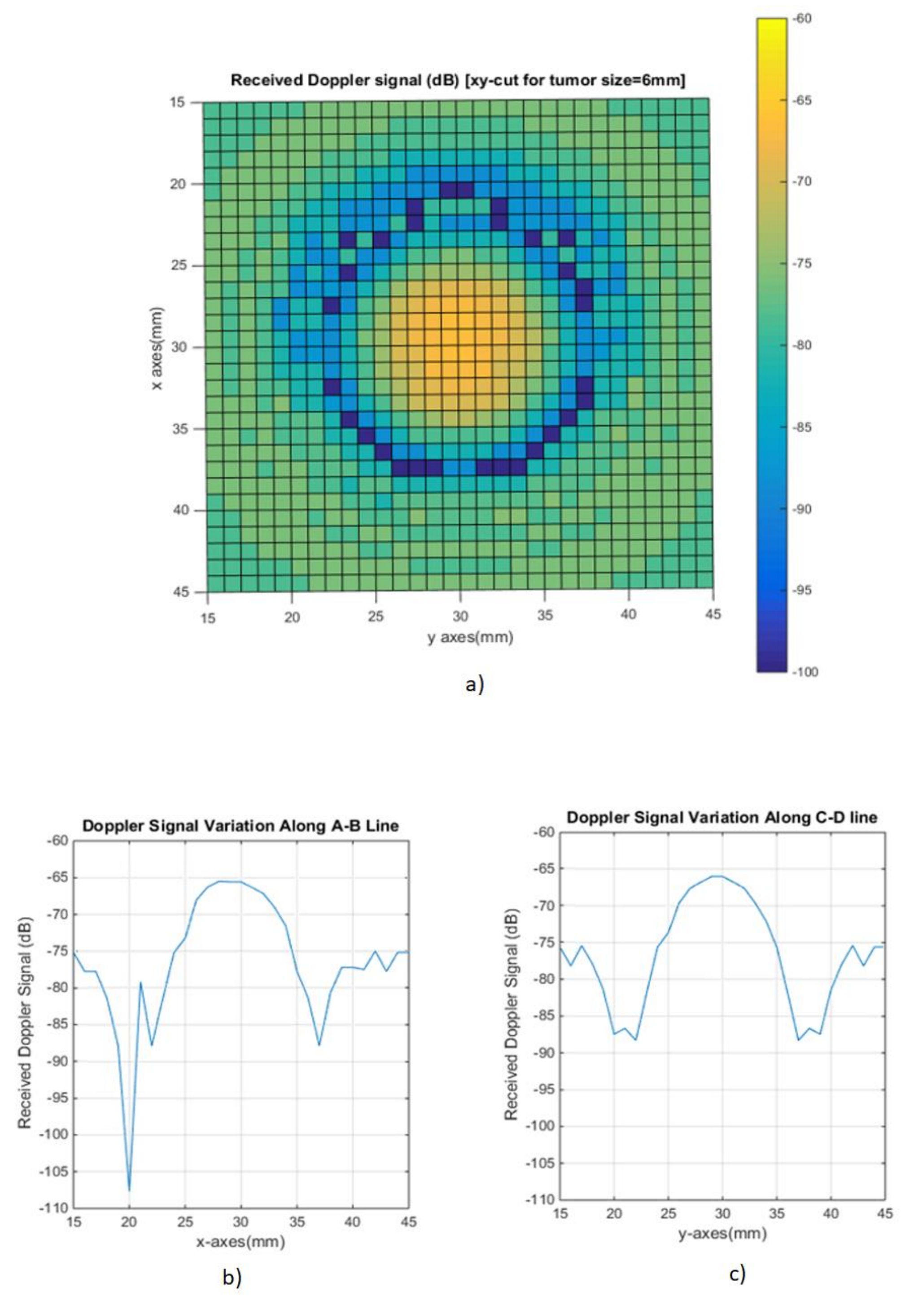

a)

b)

c)

Figure 3.19. The distribution of the normalized received Doppler signal from a 6 mm cubic tumor a) 2D xy view b) variation along A-B line c) variation along C-D line.

3.7 Conclusion

Previously, the simulation method for solving the forward EM problem of HMMDI was implemented via the FDTD [50]. In the previous chapter, the effect of the vibration of neighboring tissues was analyzed with FDTD code. However, the simulation time elapsed for each tumor position was approximately 122 minutes on a computer with Intel Xeon E5-2696 V4 processor. Analyzing for different vibration frequencies or different tumor sizes become impractical via performing simulations with same the FDTD code. In this study, an alternative simulation method, based on DDA was implemented since the DDA method provides a general solution, handling scattering from arbitrary geometry deformed due to vibration.

The received Doppler signal is calculated both with the proposed method and the FDTD method. Comparing the simulation results of the proposed DDA based methods with FDTD, 3-stage DDA based simulation results showed a high agreement with FDTD with error less than 0.27 dB, whereas the error between 1-stage DDA based method and FDTD is 1.37 dB. The 3-stage DDA and 1-stage DDA based methods decreased the simulation time by a factor of 146 and 398 respectively, compared to the FDTD method. Fast EM simulations enabled us to investigate the HMMDI imaging as a function of tumor sizes. In 2D simulations, it was observed that the image of the tumor has strong correlation with the displacement map. The Lateral resolution of HMMDI is better than axial resolution. In the 3D scan, it was shown that the received Doppler signal level increases for small tumors that are within the half power beamwidth of the acoustic intensity. On the other hand, regardless of the size, when focus of the FUS probe moves away from the edge of the tumor the rate of decrease in the Doppler signal as a function of distance shows similar behavior.

CHAPTER 4

THE EFFECT OF CONTRASTS IN ELECTRICAL AND MECHANICAL PROPERTIES BETWEEN BREAST TISSUES ON HMMDI

4.1 Introduction

The image construction from a HMMDI scan is performed via collecting the received the Doppler signal while raster scanning of the FUS probe over the breast. Since HMMDI is a hybrid method employing both ultrasound excitation and microwave imaging, the received Doppler signal level strongly depends on electrical properties as well as the maximum displacement of the vibrating tissue. The elasticity of vibrating tissue, the frequency of mechanical excitation, and the acoustic force applied to the tissue are the main parameters affecting the maximum signal level.

Contrasts in the dielectric and elastic properties between the tumor and the surrounding normal breast tissue enhance the level of the received Doppler signal. On the other hand, the same amount of increase in contrast in either of the dielectric or elastic properties of the tissue may not yield the same effect on the Doppler signal level since they are different mechanisms. Moreover, the vibration frequency determines the region of the. A study is needed to investigate the effect of increasing contrast in one property (either of elastic or dielectric properties) of tumor on the Doppler signal level while keeping other property fixed as a function of vibration frequency. Implementation of DDA based simulation tool allowed us to study the effect of contrasts as a function of vibration frequency and tumor position. The contrast mechanisms are investigated for three dielectric and three elastic contrasts values. The contribution of unintended vibrations of the neighboring tissues on the received Doppler signal level as a function of vibration frequency and contrast in electrical and mechanical properties is also analyzed.

4.2 The Simulation Model

In order to study the effect of contrasts on HMMDI, the simulation model in chapter 3.3 is also utilized in this section. In the simulations, breast tissue is assumed to be a medium of adipose tissue, as such the relative permittivity and conductivity of the breast tissue at 4.5 GHz are ε_R=23, σ=3.5 S/m [18] and Young's modulus is set 3.8 kPa [31,32]. The incident field inside the breast tissue was calculated only once via FDTD method.

Using the developed simulation 3- stage DDA based tool in Chapter 3, the effect of contrasts in the dielectric or elastic properties between the inclusion and the normal breast tissue is investigated in this Chapter. Both dielectric and elastic properties of the inclusion is parametrically swept whereas those properties of the breast tissue are kept constant throughout the simulations. The contrast between the dielectric properties of inclusion and breast tissue (CD) is defined as the ratio of relative dielectric permittivity of the inclusion to that of the breast tissue. In a similar manner, the contrast between elastic properties of inclusion and breast tissue (CE) is defined as the ratio of the Young's modulus of the inclusion to that of the breast tissue.

The effect of dielectric properties of inclusion is analyzed as a function of vibration frequency while keeping CE at 1.5, assuming low elasticity contrast case [27]. The relation between the refractive index *m* and CD can be expressed as;

$$m = \sqrt{\frac{\varepsilon_{tumor}}{\varepsilon_{breast\_tissue}}} = \sqrt{CD} \tag{4.1}$$

The effect of CD on the Doppler signal level is analyzed for three different values of CD: 1.17, 2.6 and 3.75 representing the typical ratios of complex permittivity of tumor to that of low adipose-content, medium adipose-content and high adipose-content breast tissues [15-19], respectively. In order to comply with the convergence criteria for the DDA solution ($|m-1| \leq 1$) [62], the maximum value of CD is limited to 3.75. Similarly, the effect of CE was analyzed as a function of vibration frequency, while keeping CD at 1.17. The effect of CE on the Doppler signal level is analyzed for three different values of CE (1.5, 2.5 and 5), representing low and moderate contrast cases [22-28]. The simulations are repeated for vibration frequencies from 15 Hz to 95 Hz with 5 Hz steps.

The position of the FUS probe is fixed and the position of the tumor is scanned horizontally along the A-B line, and vertically along the C-D line as shown in Fig. 3.5b. The inclusion is scanned linearly with 1 mm steps in the axial and lateral planes (orthogonal planes) with respect to the focus of the FUS probe. The scan lines intersect at the focus of the FUS probe. At each scan point, the dielectric and elastic parameters of the inclusion and the vibration frequency are varied in the simulation model to analyze the resolution of HMMDI as a function of different contrasts in both dielectric and elastic properties as well as vibration frequencies. In these simulations, CD values were 1.17, 2.5 or 3.75, and CE values are 1.5, 2.5 or 5.

4.3 The Simulation Results

In Fig. 4.1a, the effect of CD value on the Doppler signal level is shown as a function of vibration frequency. The signal level is maximum between 25 Hz-45 Hz frequencies, and decreased for lower and higher vibration frequencies. In Fig. 4.1b, the change in the received Doppler signal level is plotted when increasing CD from 1.17 to 2.6 and 3.75 while keeping CE as 1.5. As the CD is changed from 1.17 to 2.6, the received Doppler signal level increases by almost 3.4 dB for all vibration frequencies except 95 Hz. Similarly, changing CD from 1.17 to 3.75 yields around 5.1 dB increase in received Doppler signal level for vibration frequencies up to 90 Hz. For vibration frequency as 95 Hz, the change in received Doppler signal level slightly decreases.

In Fig. 4.2a, the variation of Doppler signal level as function of vibration frequency is shown for three different CE values of the tumor, while keeping CD as 1.17. As CE is increased (via increasing Young’s modulus of tumor), the received Doppler signal level tends to decrease. For a given CE contrast ratio, received signal level increases changing vibration frequency from 15 Hz to 30 Hz, makes a plateau between 30 Hz and 45 Hz and tends to decrease for vibration frequencies higher than 45 Hz. However, the received signal level decreases further when vibration frequency exceeds 80 Hz. In Fig. 4.2b, the difference in the received Doppler signal level due to increasing CE from 1.5 to 2.5 and 5 are given. When CE is changed from 1.5 to 2.5 the received Doppler signal level decreases around 0.5 dB and the difference increases to 0.7 dB for vibration frequency 90 Hz and 1.2 dB for 95 Hz. On the other hand, as CE is increased from 1.5 to 5, Doppler signal level decreases more than 0.75 dB. For higher CE, the decrease rate in the Doppler signal is higher as the vibration frequency increases and the difference increases to 2.65 dB for vibration frequency 95 Hz.

In Fig. 4.3 and Fig. 4.4, the ROD for three different axial tumor positions, 5 mm (Fig 4.3a), 8 mm (Fig 4.3b) and 10 mm (Fig 4.4) with respect to the focus of the FUS probe are plotted as a function of vibration frequency. In these figures, the results of different contrast ratios CD and CE are given in the same plot. In these figures, the curve color (black, blue or red) is related to CD and type of line (solid, dashed or dotted on solid line) is related to CE.

The ROD basically increases via either moving tumor away from the focus of the FUS probe or via increasing the vibration frequency. However, increasing vibration frequency has more dominant effect on the ROD than moving the tumor away. For instance, for a 15 Hz vibration frequency, maximum ROD is 7.8 dB when the tumor is moved along z axis 10 mm away from the focus of the FUS probe. On the other hand, similar ROD is observed at only 5 mm away from focus of FUS transducer via increasing the vibration frequency to 95 Hz. More than 20 dB ROD can be achieved with 90Hz vibration frequency when the tumor is distanced 8 mm away from the focal region.

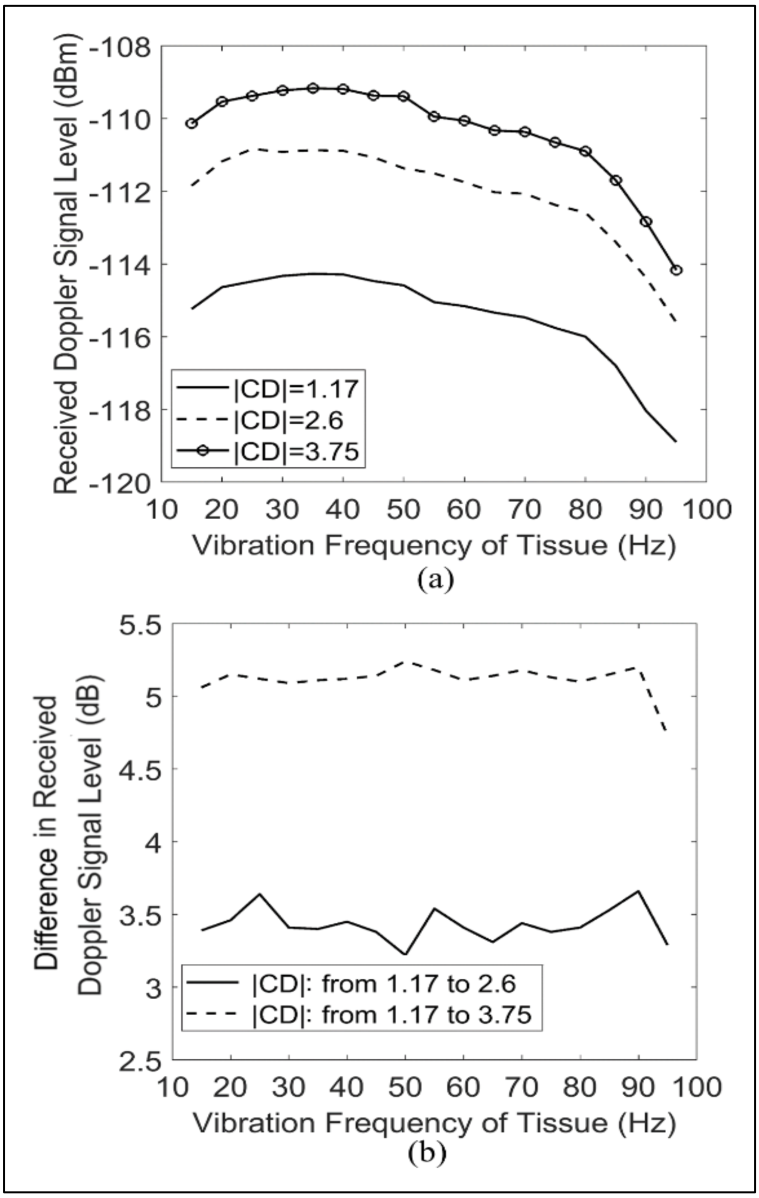

Figure 4.1 Received Doppler signal level as a function of vibration frequency for various CD values (when the tumor is at the focus of the FUS probe) a) Altering the CD of a cubic tumor with 3 mm edge length while keeping CE value fixed as 1.5 b) The difference in the received Doppler signal level when increasing CD from 1.17 to 2.6 and 3.75 while keeping CE as 1.5.

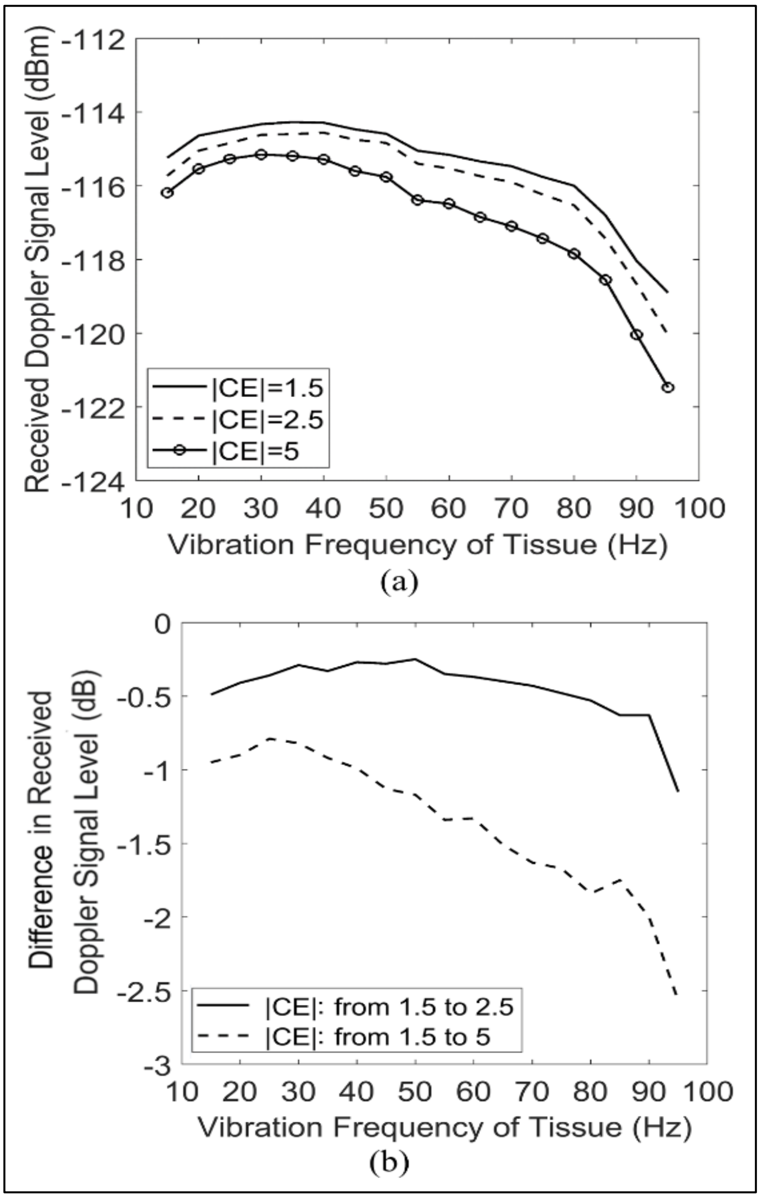

Figure 4.2. Received Doppler signal level as function of vibration frequency for various CE values (when tumor is at focus of the FUS probe) a) Altering the CE of a cubic tumor with 3 mm edge length while keeping CD value fixed as 1.17 b) The change in the received Doppler signal level when increasing CE from 1.5 to 2.5 and 5 while keeping CD as 1.17

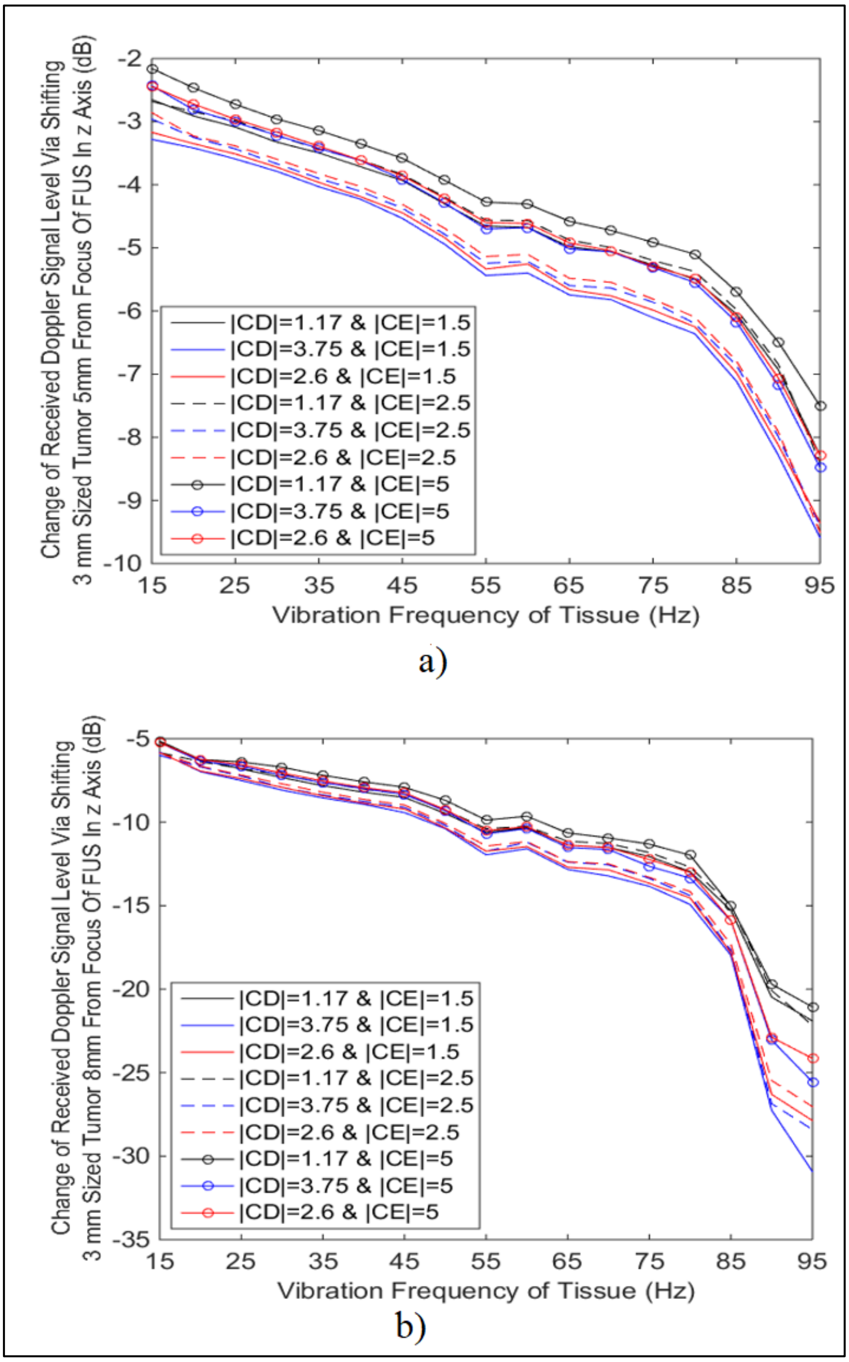

Figure 4.3 The ROD as function of vibration frequency for a 3 mm cubic tumor that located at a) 5 mm and b) 8 mm away from focus of FUS transducer along z axis. The ROD variation is presented for different CD and CE values.

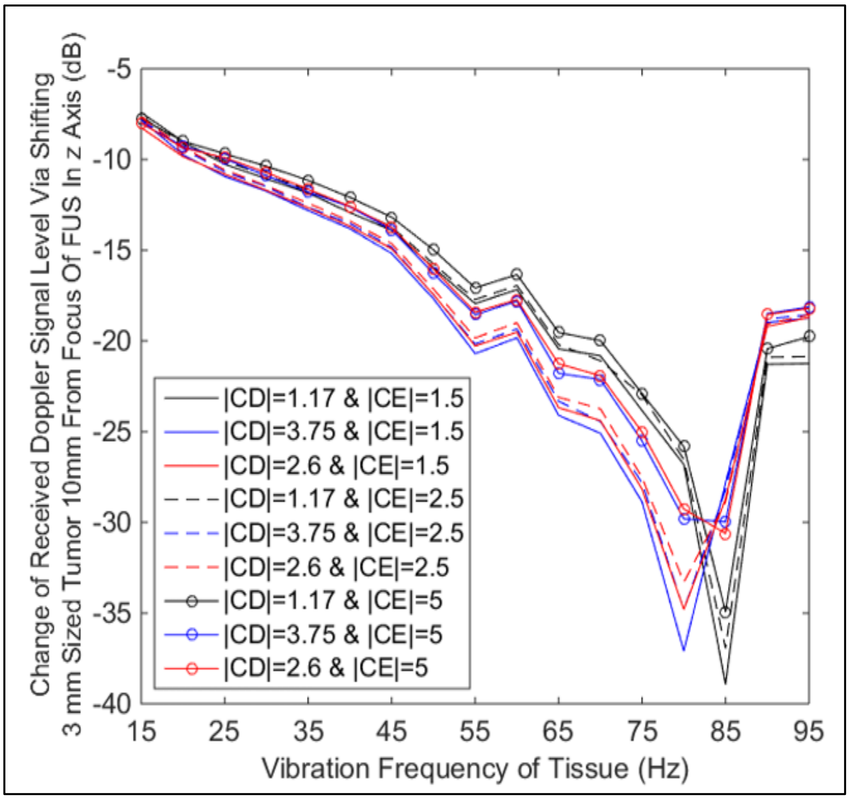

Figure 4.4 The ROD as function of vibration frequency for a 3mm tumor that is located at 10 mm away from focus of FUS transducer along z axis. The ROD variation is presented for different CD and CE values.

The contrast in the dielectric and elastic properties between the tumor and breast tissue also affects ROD; ROD is smallest when CD is minimum (1.17) and CE is maximum (5) and is highest when CD is maximum (3.75) and CE is minimum (1.5). For low CD values, at most 1.1 dB decrease in ROD is observed for all values of CE. However, for higher CD values, the variation on CE has more dominant effect on ROD, especially for higher vibration frequencies.

In Figure 4.5, ROD for three different lateral tumor positions, 3 mm (Fig, 4.5a), and 5 mm (Fig, 4.5b) with respect to the focus of FUS transducer are plotted as a function of vibration frequency. The ROD values in this axis are higher compared to that of

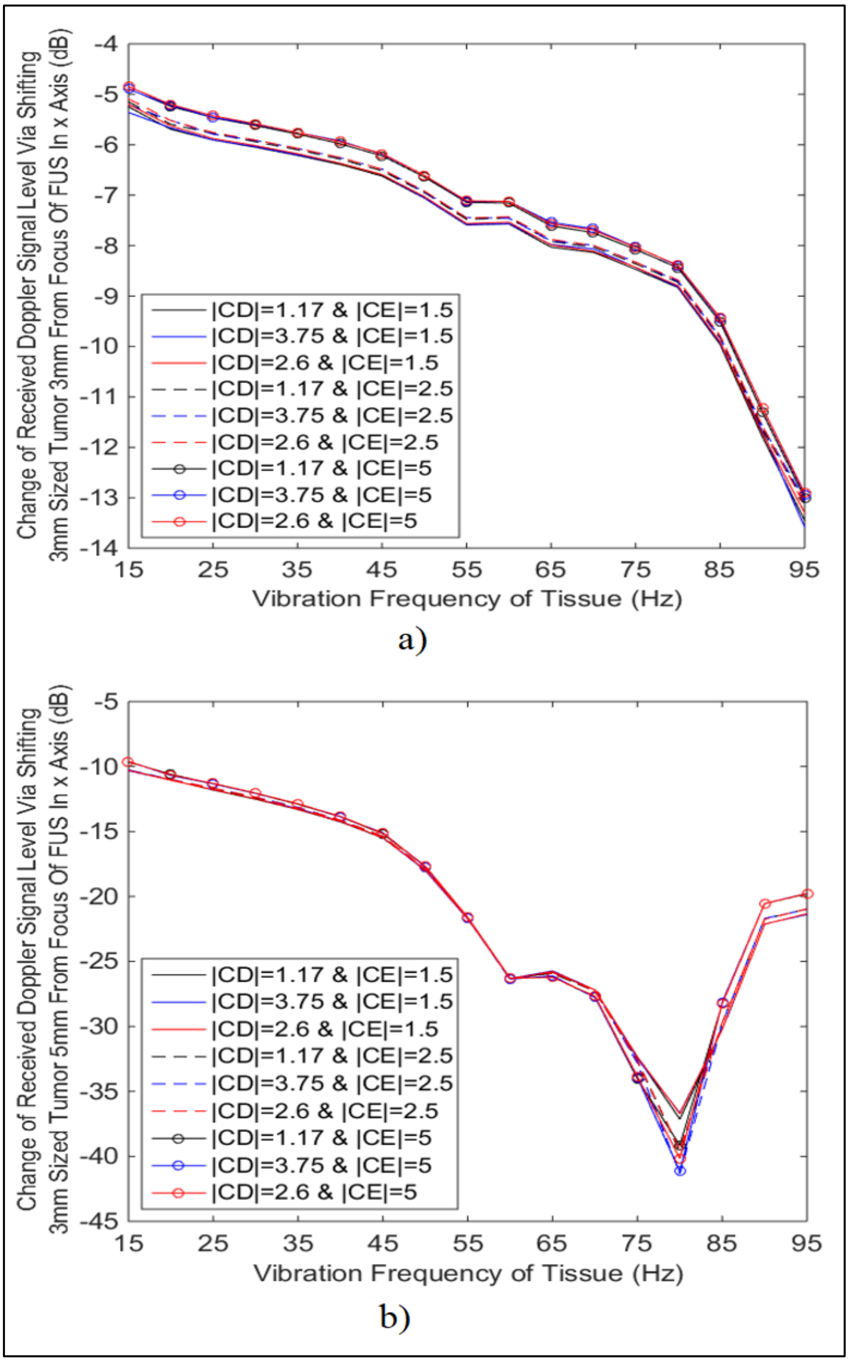

a)

b)

Figure 4.5 The ROD as function of vibration frequency for a 3mm tumor that is moved a) 3 mm, b) 5 mm away from focus of FUS transducer along x axis. ROD variation is plot for different CD and CE values.

axial axis as a result of the elliptic FUS beam shape. FUS beamwidth in lateral axis is much smaller than beamwidth in axial axis [49]. Moving the tumor only 3 mm away in lateral axis from the focus yields more than 5 dB ROD for 15 Hz vibration frequency. The ROD increases with a higher rate as vibration frequency increases. In Fig. 4.3, it is observed that CE has more dominant effect on ROD than CD variation, since for fixed values of CE, different CD ratios yield similar ROD characteristics.

4.4 Conclusion

Fast EM simulations enabled us to investigate the Doppler signal variation as a function of tumor position for different dielectric and elastic contrast values, as well as different vibration frequencies. In this chapter, the effect of contrast in the dielectric and elastic properties between tumor and surrounding breast tissue is analyzed as a function of vibration frequency.

It is observed that the maximum vibration amplitude at the focal region increases with decreasing vibration frequency, which consequently increases the received Doppler signal [49]. On the other hand, if vibration frequency is decreased, the volume of vibrating region increases, which may cause vibration of the neighboring tissues around the focal region deteriorating the resolution and introducing image artifacts [52].

During the scanning of the tumor along the lateral and axial axes, the received Doppler signal is maximum when the tumor is at the focus of the ultrasound probe. The decrease in the Doppler signal level is higher in the lateral scan than in the axial scan, which is a result of larger beamwidth of the FUS probe in the axial direction compared to the lateral beamwidth. This is related to the DRW which was defined in [50] as the width where half maximum of displacement occurs. As the vibration frequency increases, the DRW decreases as a result of decreasing vibration amplitude. Sweeping the tumor away from focal region, the received Doppler signal level drops to a very low level at a certain position. After slightly moving the tumor away from that position, Doppler signal increases rapidly and a local maximum is observed. Further moving the tumor away yields decrease of Doppler signal with a high rate.

The effect of dielectric and elastic constant on the maximum received Doppler signal was studied via altering contrast in either one of dielectric or elastic properties of tumor while keeping the other property at a constant value. When CE is kept constant, by increasing CD from 1.17 to 2.6, the received Doppler signal increased by almost 3.4 dB for all vibration frequencies except 95 Hz, and by further increasing CD from 1.17 to 3.75, the received Doppler signal increased by almost 5.1 dB for all vibration frequencies except 95 Hz. For 95 Hz vibration frequency, the rise in the Doppler signal level via increasing contrast level is slightly lower than other vibration frequencies. This is due to decrease in DRW with respect to increasing vibration frequency [50]. When tumor physically is larger than DRW, the Doppler signal is received only from (partial) vibrating region of tumor. It can be concluded that the dielectric contrast has a linear effect on HMMDI level since the difference on the curves in Fig. 4.1 over vibration frequency is almost constant provided that DRW is larger than tumor size. On the other hand, the variation of Doppler signal as a function of vibration frequency is not linear for different CE values (while keeping CD constant). The received Doppler signal level is maximum for vibration frequencies ranging from 25 Hz to 45 Hz, and as vibration frequency increases above 45 Hz received Doppler signal level decreases and when vibration frequency exceeds 80 Hz, the Doppler signal level decreases with higher rate. Rate of decrease in Doppler signal depends on both vibration frequency, DRW and CE. Because the stiffness of the tumor is higher than normal breast tissues, one can discriminate the tumors via comparison of subsequent scanning; one scan with high vibration frequency and other scan with low vibration frequency.

For vibration frequencies below 25 Hz, the received Doppler signal also tends to decrease even though DRW gets larger for lower vibration frequency. Received Doppler stems from the shape deformations of tumor due to ARF at maximum and minimum displacement instants. However, distribution of ARF over a small tumor at the focus is almost constant over the small tumor volume. ARF only shifts the tumor as a whole by a constant offset without a shape deformation. As a result, the inter distances between dipoles does not change significantly at maximum and minimum displacement instants. The maximum displacement of tumor is on the order of microns, and shifting whole tumor by a small offset does not yield a significant phase modulation. However, the shape deformations on tumor yields higher phase difference between dipoles modeling tumor in DDA method.

For a tumor size of 3 mm, increasing CD via altering dielectric constant of tumor, yields nearly constant (offset) increase in the Doppler signal over a wide vibration frequency range. Moreover, the increase in Doppler signal level is around 3.4 dB when increasing CD from 1.17 to 2.6. Conversely, increasing CE only yielded a decrease in the received Doppler signal level since stiffer tissues vibrates less. Even if CE is changed from 1.5 to 5, the decrease in Doppler signal level is at most 2.65 dB. On the other hand, the effect of changing CE did not show a constant decrease in Doppler signal level for all vibration frequencies, because tissue displacements are nonlinear function of vibration frequency and elastic properties of the tissue.

It was observed that when either of CD or CE is increased by same amount, the effect of increasing CD is more dominant on the signal level than increasing CE. Another observation is that the change in the received Doppler signal due to varying CD is independent of vibration frequency up to 90 Hz. However, the effect of CE is increases when increasing vibration frequency further from 40 Hz. Based on these observations, when the whole breast is subsequently scanned twice with different vibration frequencies in each scan, we can discriminate the stiffer tissues.

The contribution of vibration of neighboring tissues on the received Doppler signal level was studied via sweeping the tumor away from the focal region along axial and lateral axis. From Fig.4.3 –Fig. 4.5, it is observed that the main parameter affecting the Doppler signal level from neighboring tumor is the vibration frequency. The vibration frequency determines the DRW and wide DRW results in receiving high Doppler signal level from tumors away from the focal region. As a result, image resolution of HMMDI deteriorates. For example, for 15 Hz vibration frequency even if tumor is displaced 10 mm away from the focal region, the received Doppler signal level only decrease by 7.8 dB. However, for 95 Hz vibration frequency, when tumor is displaced 5 mm away from focal region, received Doppler signal decreases more than 7 dB. Although, increasing vibration frequency enhances the image resolution of HMMDI due to less displacement of the neighboring tissues, the received Doppler signal from distant tissues tends to increase. As seen from Fig. 4.4 and Fig. 4.5, even if the position of the tumor where minimum received Doppler is achieved approaches to focal region, the Doppler signal increases for further sweeping away the tumor. The local maximum level of Doppler signal also increases as the vibration of frequency increases as a side lobe. However, these sidelobe levels are more than 20 dB below the maximum signal level and becomes a problem when SNR decreases due to lower signal level at higher vibration frequencies.

Another observation is that displacing tumor 5 mm away from focal region along lateral axis (x direction) yields more than 10 dB decrease in received Doppler signal. On the other hand, moving tumor same amount of distance along axial axis (z direction) yields less than 10 dB decrease in received Doppler signal level even for high vibration frequencies. This is because DRW in lateral direction is much smaller than DRW in axial direction [50].

While sweeping the tumor in axial (z) direction, increasing CD and decreasing CE decrease the contribution of neighboring tumors 5 mm away from focal region to Doppler signal more than 1 dB. The effect of increasing the CE becomes more dominant for tumor at least 8 mm away from focal region when vibration frequency increases.

CHAPTER 5

ENCHANCING RECEIVED DOPPLER SIGNAL LEVELS IN HMMDI VIA MAIN SIGNAL CANCELLATION CIRCUIT

5.1 Introduction

One of the main limitations of the HMMDI is the inevitable phase noise of the microwave signal source. A spread in the spectrum is observed around the transmitted microwave frequency. The effect of phase noise becomes prominent at the Doppler frequency $\omega_m \pm \Delta\omega$ ($\Delta\omega \ll \omega_m$) since it is at close proximity to the transmitted microwave frequency, ω_m. The Doppler component of the received signal is away from the main transmitted microwave signal (order of GHz's) by only an amount of the frequency of vibration (order of Hz's) , $\Delta\omega$. Moreover, the level of the main transmitted signal is much larger than the level Doppler signal. If the transmitted signal has high phase noise, the Doppler signal component may not be extracted from the spectrum. The main signal to the Doppler signal level can be defined as a figure of merit for HMMDI. On the other hand, the experimental studies showed that the Doppler signal is detectable if the vibration frequency is between 10-35 Hz, because the maximum displacement by the FUS Probe excitation is larger for lower vibration frequencies.

Another limitation is the increase of the main signal level at the receiving antenna due to the direct coupling of transmitted signal to receiving antenna. Owing to the coupling between antennas, the Doppler signal is suppressed by the phase noise of coupled signal from the transmitter antenna. Suffered from phase noise, the SNR is generally low at the Doppler frequency component [52]. In previous experimental studies [49], [52], in order to decrease the direct coupling of transmitted signal to receiver antenna, a lossy medium was utilized between the antennas via placing a falcon tube filled with water. Since the dielectric constant of water is higher than that of oil, the direct signal coupling is reduced by 5-7 dB [52]. However, the distance between the antennas, limits the volume that can be filled with water. As the distance between the transmitting and receiving antennas are increased more than 16 mm, the received Doppler signal level decreases drastically [49], [52].

In this study, it is aimed to enhance the sensitivity of the HMMDI system by eliminating the coupled signal from the transmitting to the receiving antenna. In order to increase the SNR level of the system, a signal cancellation circuit is implemented, similar to the reflected power cancellers in monostatic CW radars [88], [89]. Breast phantoms with hard inclusions are imaged using the HMMDI system, with and without the signal cancellation circuit. The method is explained in Section 5.2 and the measurement results are provided in Section 5.3.

5.2 Main Signal Cancellation Circuit

In order to overcome the limitations due to phase noise of the microwave source and the direct coupling between the antennas, a Main Signal Cancellation (MSC) circuit is implemented in the HMMDI experimental set-up. This circuit suppresses the main frequency component, ω_m which couples to the receiving antenna (R_x), independent of the type of medium (lossy or not) between the antennas and the distance between the antennas.

The schematic of the MSC circuit is presented in Fig. 5.1. The microwave source of the transmitting antenna (T_x) is first, given input to a directional coupler so that the power is transmitted to the T_x antenna with minimal loss in RF power. Because of the RF transmission path loss between the T_x and R_x antenna, the main signal level at the received antenna is, typically 35-45 dB lower than the power level at the input of the T_x antenna. In the sampled port, a signal level that is 30 dB below the transmitted signal is achieved and this signal is given to the input of the MSC circuit. Even if the RF signal in the sampled port is 30 dB lower than the power transmitted to the antenna, its level is still comparable to the level of RF signal at the receiving

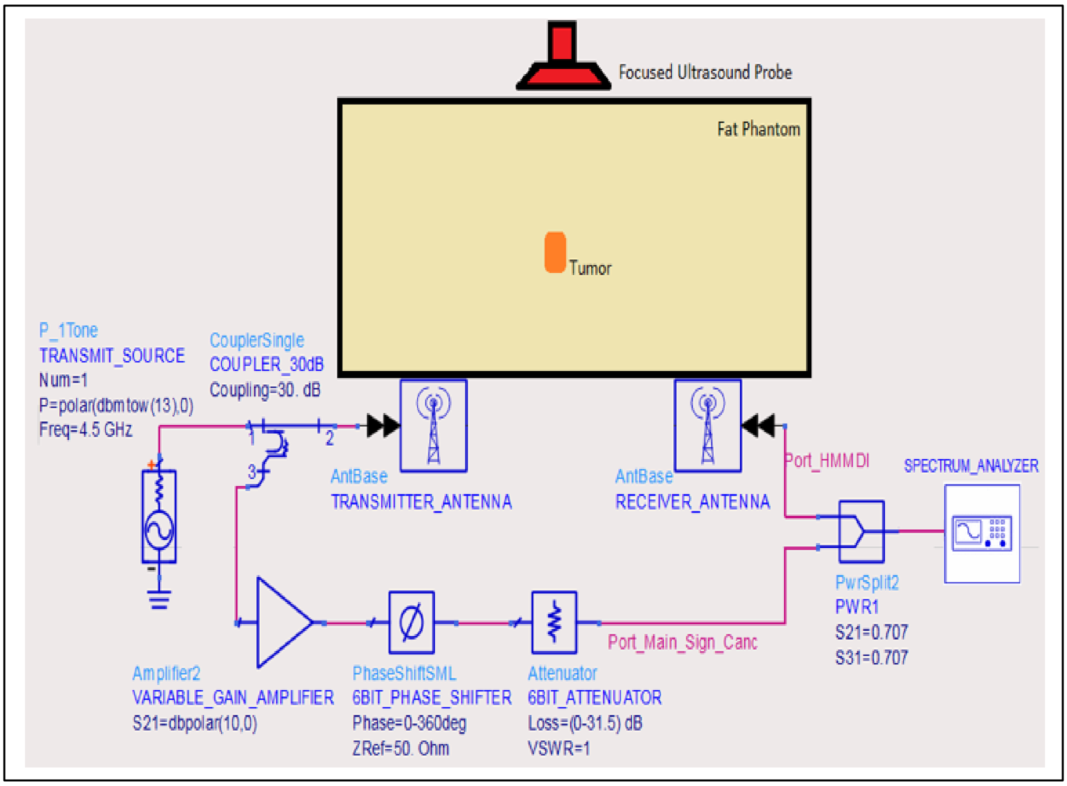
Focused Ultrasound Probe
Fat Phantom
Tumor
P_1Tone
TRANSMIT_SOURCE
Num=1
P=polar(dbmtow(13),0)
Freq=4.5 GHz
CouplerSingle
COUPLER_30dB
Coupling=30. dB
1
2
3
AntBase
TRANSMITTER_ANTENNA
AntBase
RECEIVER_ANTENNA
Port_HMMDI
SPECTRUM_ANALYZER
PwrSplit2
PWR1
S21=0.707
S31=0.707
Port_Main_Sign_Canc
Amplifier2
VARIABLE_GAIN_AMPLIFIER
S21=dbpolar(10,0)
PhaseShiftSML
6BIT_PHASE_SHIFTER
Phase=0-360deg
ZRef=50. Ohm
Attenuator
6BIT_ATTENUATOR
Loss=(0-31.5) dB
VSWR=1

Figure 5.1. Schematic of the improved HMMDI experimental set-up: main signal cancellation circuit is utilized.

antenna. In the MSC circuitry, the level of the signal in the sampled port (Port_Main_Sign_Canc) is adjusted to the level of the coupled (from Tx to Rx antenna) main signal component (Port_HMMDI) by utilizing a 6-bit digital step attenuator (with 31.5 dB maximum) and a variable gain amplifier. For instance, if the level of the signal in sampled port (Port_Main_Sign_Canc) is much higher than the power level in the receiving antenna, the attenuation of the 6-bit attenuator is increased. After signal level equalization between the sampled port and output of the receiving antenna, the phase of the sampled port is adjusted to get an opposite phase signal with respect to the coupled signal at the receiving antenna. In the next step, the receiving and the cancelling signals are combined using a two-way 0° Wilkinson divider/combiner. As a result, two signals with same amplitude but with reverse polarity tend to cancel each other, increasing the SNR of the received signal at the Doppler frequency. The MSC circuit is simulated in ADS© EM simulator in order to investigate the effect of the phase difference between the signals with same amplitude. The performance of the MSC circuit as a function of the phase difference at the ports of the Wilkinson divider is given in Fig 5.2 and Fig. 5.3. The main signal is at 4 GHz and the Doppler signal is 30 Hz away from the main signal in the frequency spectrum. In the simulations, the phase noise of the microwave source signal is omitted. When the phase difference of the signals between the two ports of the Wilkinson divider is 90 degrees, the net main signal level is 29 dBm. As the phase difference is set to 180 degrees the main signal is cancelled by 50 dB. At this point, the main signal level is comparable to that of the Doppler signal. However, if the phase between two signals are 179 degrees, cancellation reduces to 38 dB and when the phase difference is 176 degrees cancellation ratio becomes 33.8 dB.

The main signal cancellation network is designed on a PCB (Fig. 5.4). A variable gain RF block, a 6-bit level controlled digital attenuator, and a 6-bit phase shifter are utilized in this design. The network can operate in the 3.5-6 GHz frequency range in order to comply with the operation frequency of the HMMDI setup. However, there are some physical non idealities of the components. For instance, the phase shifter is 6-bit and the phase resolution of the system is 5.625º. Moreover, the phase shifter exhibits a phase error as function of operating frequency. For instance, when adjusted for 90º, the actual phase shift is around 91º around 3.5 GHz, and 92.5º at 6 GHz. Similarly, the 6-bit digital attenuator has 0.5 dB minimum attenuation step and its attenuation level changes as a function of frequency.

5.2.1 Measurement Set-Up

The performance of the MSC circuit was tested using an oil-in gelatin dispersion type breast fat phantom with hard inclusions. In the experimental set-up two separate

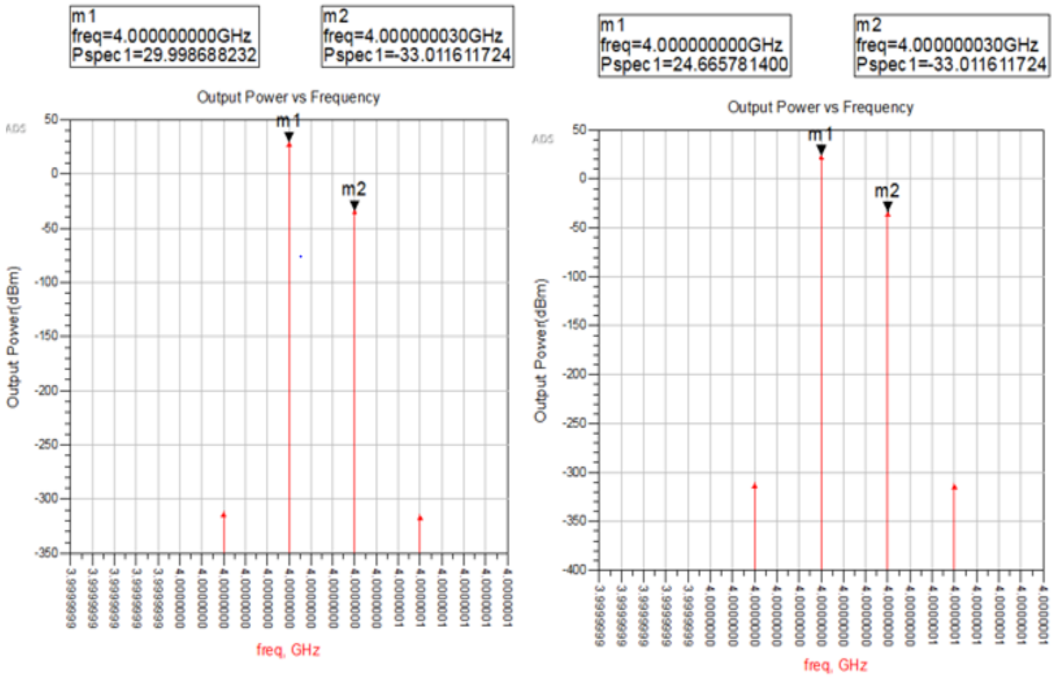

a) Phase: 90 Degrees

b) Phase: 135 Degrees

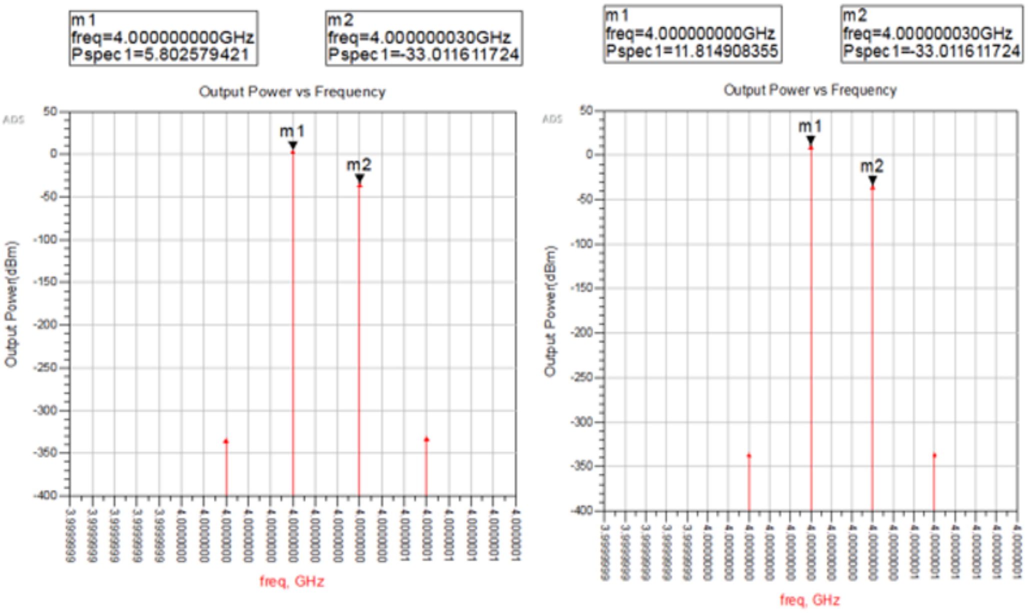

c) Phase:160 Degrees

d) Phase: 170 Degrees

Figure 5.2. Simulation results for the spectrum of the received signal at combined output of Wilkinson divider when the phase difference between the ports of the divider is a) 90 degrees b) 135 degrees c) 160 degrees d) 170 degrees

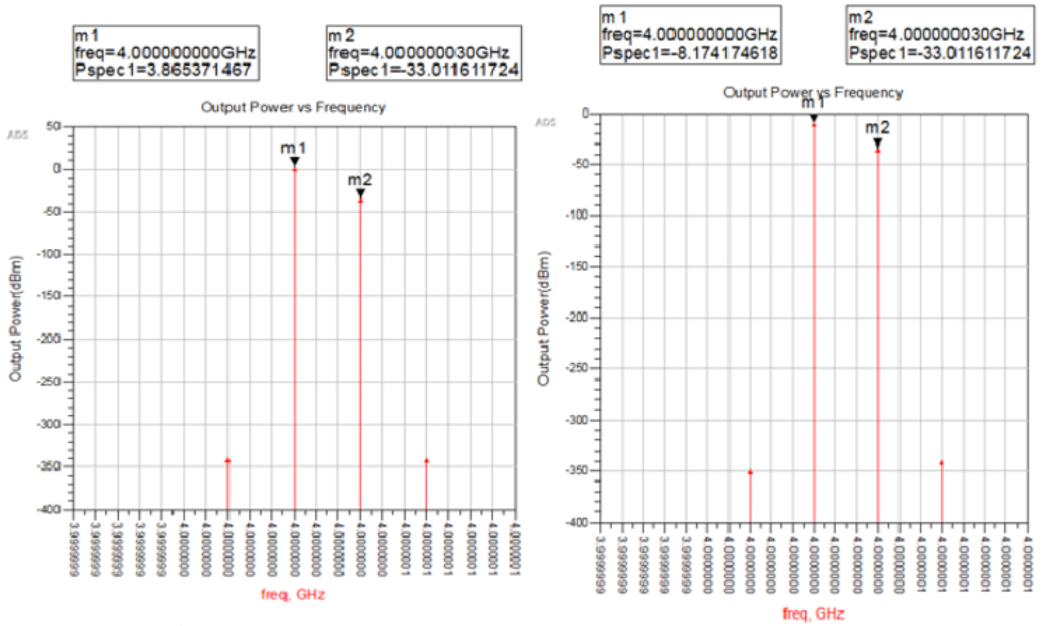

a) Phase: 176 Degrees

b) Phase: 179 Degrees

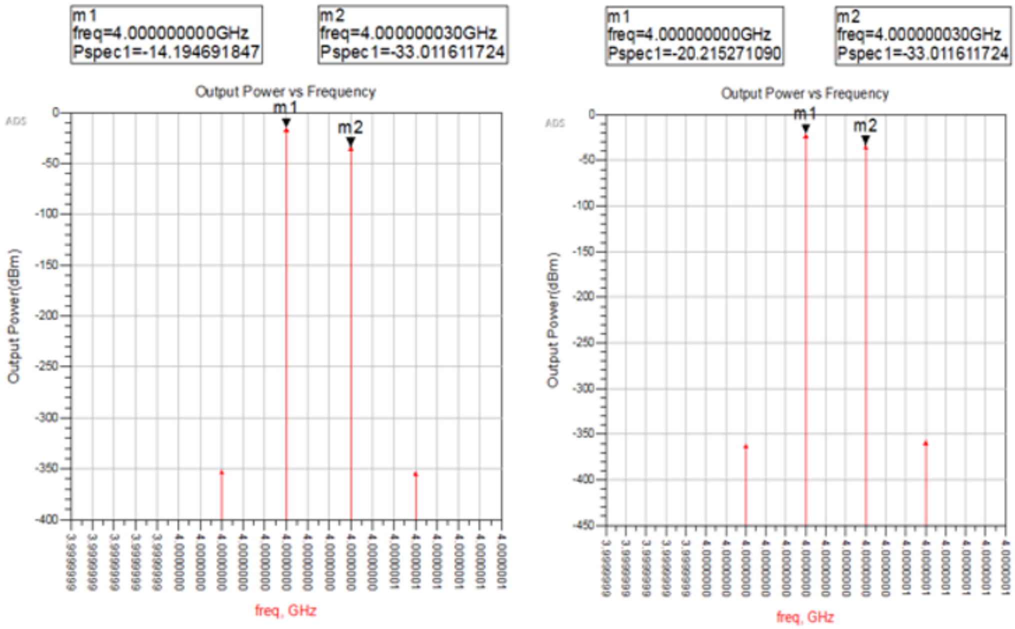

c) Phase: 179.5 Degrees

d) Phase: 179.75 Degrees

Figure 5.3. Simulation results for the spectrum of the received signal at combined output of Wilkinson divider when the phase difference between the ports of the divider is a) 176 degrees b) 179 degrees c) 179.5 degrees d) 179.75 degrees

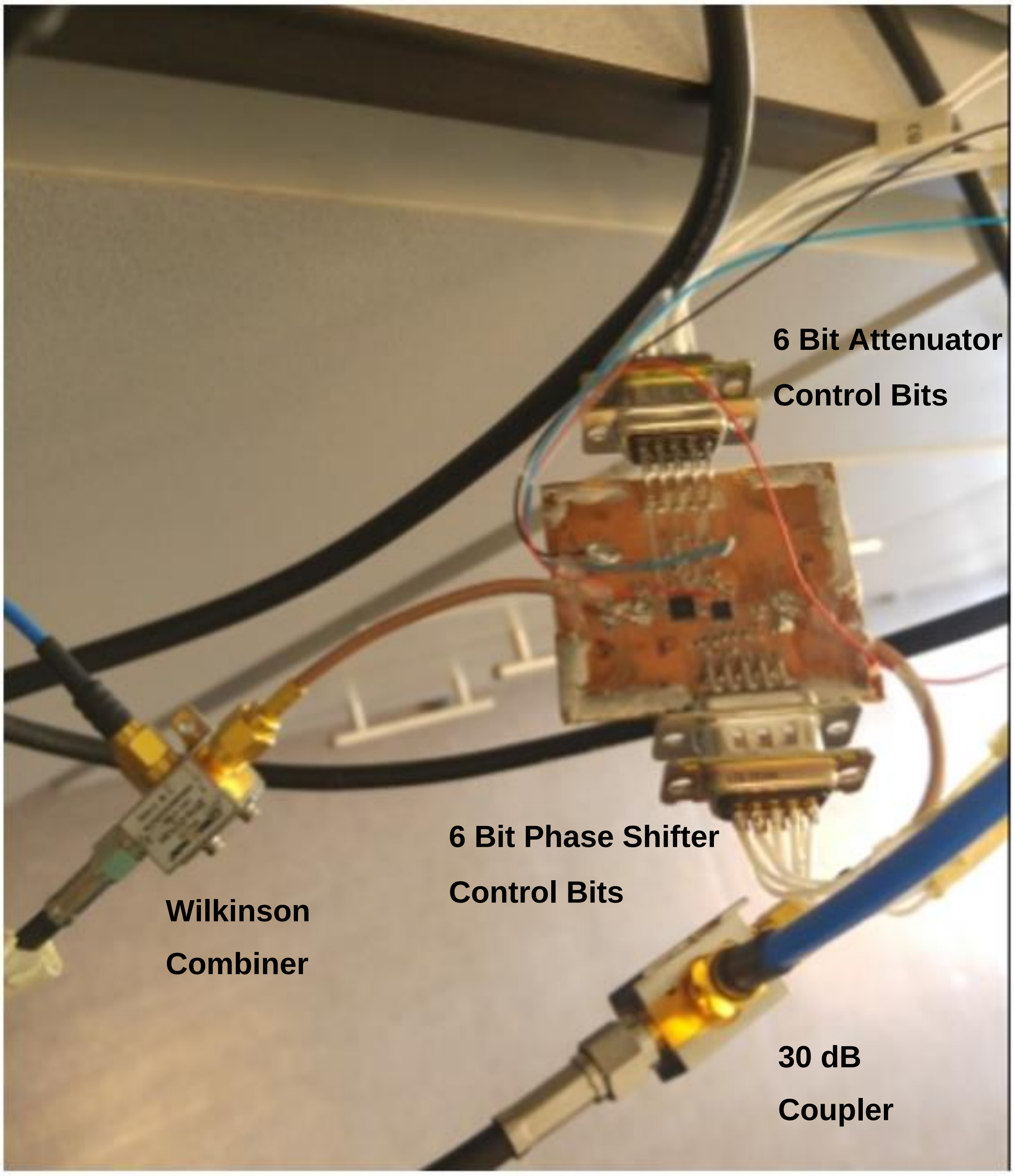
6 Bit Attenuator
Control Bits
6 Bit Phase Shifter
Control Bits
Wilkinson
Combiner
30 dB
Coupler

Figure 5.4. Implementation of MSC circuit on PCB; The 6 bit digital controlled phase shifter and attenuator are controlled with TTL signals. The transmitted RF signal is sampled via 30 dB coupler and the output of the MSC circuit is combined with the output of the receiving antenna.

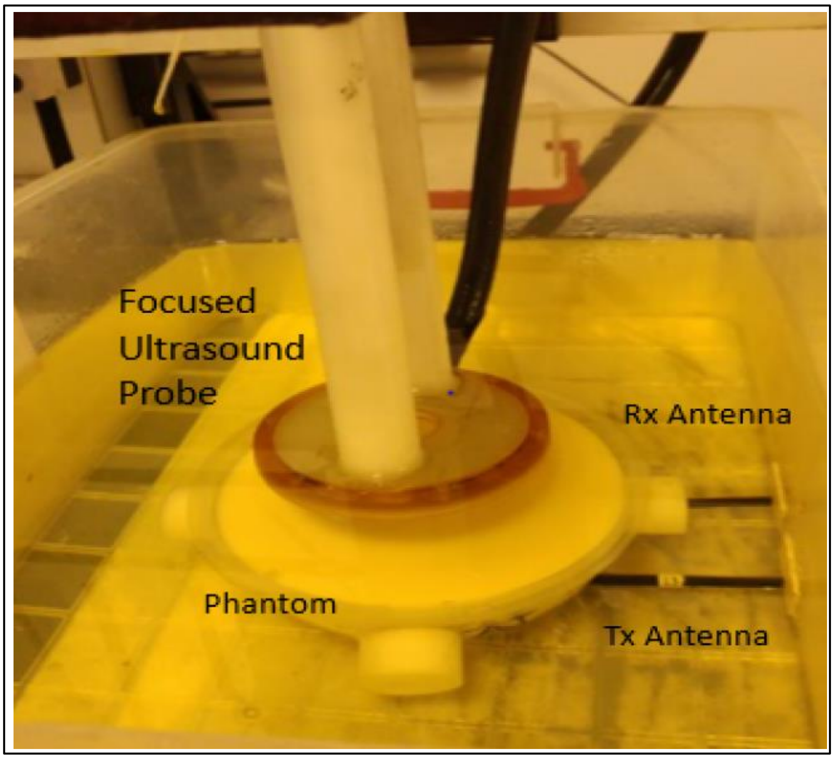

Figure 5.5. Experimental HMMDI set-up. The FUS probe is scanned over the breast phantom. The focus of the FUS probe coincides the center of the breast phantom.

dielectric-filled (sun flower oil) open ended waveguides with 23 mm x 15 mm aperture size are used as antennas to transmit and receive the microwave signals (Figure 5.5).

The antennas are placed below the phantom container in the H-plane orientation. The CW microwave signal is generated using an Agilent E8257D analog signal generator. The center frequency of the transmitted microwave signal (ω_m) was 4.5 GHz, the amplitude of microwave signal is set to +13 dBm. The received signal is displayed using a Signal Analyzer (N9072A, Keysight, CA). A focused ultrasound transducer with 63.2 mm radius of curvature and 64 mm diameter (H-102, Sonic Concepts, CA) is fed with an amplitude modulated signal at its third harmonic frequency (3.32 MHz) to induce 30 Hz vibrations at the focal point ($\Delta\omega$ =30 Hz).

The focus of the FUS transducer is aligned at the center of the larger tumor inclusion in the vertical axis. The HMMDI scanning set-up in shown in Fig. 5.5

5.2.2 Breast Phantom Construction

The phantom materials are developed based on the recipe described in [89] and similar to the procedure in previous studies [52]. The composition of one-liter realistic phantom is given in Table 5.1. In the experiments, two type of phantoms are utilized. In the first model, a cylindrical homogeneous tumor phantom of size 16 mm (diameter) x 9 mm (height) is placed at the center of 30 mm height x 11 cm diameter breast fat phantom (Fig 5.6a). In the second model, two cylindrical homogeneous tumor phantoms of size 15 mm (diameter) x 9 mm (height) and 7 mm (diameter) x 9 mm (height) with about 20 mm separation measured from their edges are placed on a 30 mm height x 11 cm diameter breast fat phantom (Fig. 5.6b). Then another 30 mm height breast fat phantom layer is poured inside the phantom container in liquid phase and left to solidify in room temperature for one week. The measured electrical and elastic parameters of the developed homogeneous fat and tumor phantoms are given in Table 5.2. Electrical parameters were measured at 4.5 GHz frequency using a coaxial probe, and Young’s modulus was obtained with static compression measurements [91].

5.3 Experimental Results

5.3.1 1D (Line) Scan Results

In order to test the performance of the MSC circuit we repeated the line scan in [52]. In a previous study [52], the tumor of size 16 mm x 9 mm could not been imaged with HMMDI for 30 Hz vibration frequency due to coupling. In order to be

Table 5.1 Compositions of one liter of fat and tumor phantom [90]. Abbreviations:, p-tol: p-toluic acid, n-prop: npropanol, forml.:formaldehyde, surf.:Surfactant , Ker: Kerosene

Tissue Type	*p-tol (gr)*	*n-prop (mL)*	*Oil (mL)*	*Ker (mL)*	*Water (mL)*	*Forml (mL)*	*Gelatin (gr)*	*Surf (mL)*
Fat	167	8.3	330	330	158	1.67	28.6	140
Tumor	800	39.6	49.5	49.5	753.5	7.9	135	10.1

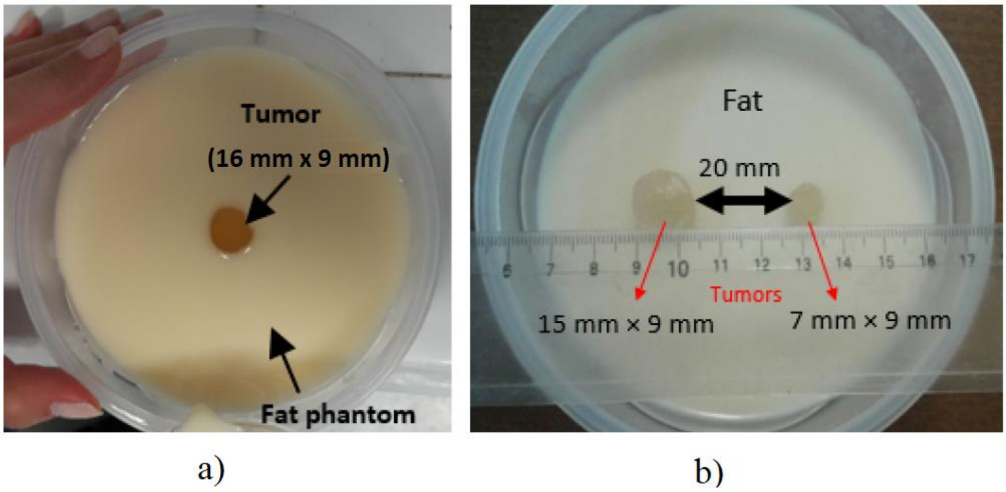
Tumor
(16 mm x 9 mm)
Fat phantom
Fat
20 mm
6
7
8
9
10
11
12
13
14
15
16
17
Tumors
15 mm × 9 mm
7 mm × 9 mm

a)

b)

Figure 5.6. The breast phantoms tested in HMMDI setup a) one cylindrical homogeneous tumor phantom of size 16 mm (diameter) x 9 mm (height) is placed at the center of 30 mm height x 11 cm diameter breast fat phantom b) two cylindrical homogeneous tumor phantoms of size 15 mm (diameter) x 9 mm (height) and 7 mm (diameter) x 9 mm (height) with about 20 mm separation measured from their edges are placed on a 30 mm height x 11 cm diameter breast fat phantom

Table 5.2 Measured electrical and elastic parameters of the developed phantoms [52]

Tissue Type	*Relative Dielectric Constant (ε_R)*	*Conductivity (S/m)*	*Young's Modulus (kPa)*
Fat	4.48	0.21	4.32
Tumor	52.7	4.91	42

consistent with the experiment, 1D scan with is carried out with same parameters in [52]. Initially, the performance of the MSC circuit is tested for one point: the focus of the FUS probe positioned to the center of the tumor and the level of the received signal at the spectrum analyzer is observed in the presence and absence of the MSC. As shown in Fig. 5.7, when the MSC circuit integrated to HMMDI setup, the main signal is suppressed by approximately 20 dB and in the spectrum analyzer the Doppler signal becomes visible.

The 1D scan is performed on a 60 mm line with 2 mm steps at which the tumor is present at the midpoint of the line. At each position of the FUS probe, 8 vibration pulses were transmitted with 1 Hz pulse repetition frequency and 100 ms pulse width. Spectrum analyzer parameters were; span 200 Hz, resolution bandwidth: 6.8 Hz, sweep time: 270 ms. The results of the 1D line scan along the x-axis for a cylindrical tumor inside a homogeneous fat phantom with and without main signal cancellation network is shown in Fig 5.8. For the case that MSC is not utilized (Fig. 5.8a), the image is very noisy with 10 dB ripples and the presence of the tumor (the diameter of tumor is represented with orange colored arrow) cannot be resolved in the figure. The Doppler signal is not visible due to direct coupling between the antennas and the phase noise of the microwave signal generator.

In Fig. 5.8b, it can be seen that the tumor is detectable from the HMMDI 1D line scan along the x-axis. It is observed that the level of the Doppler signal dropped from

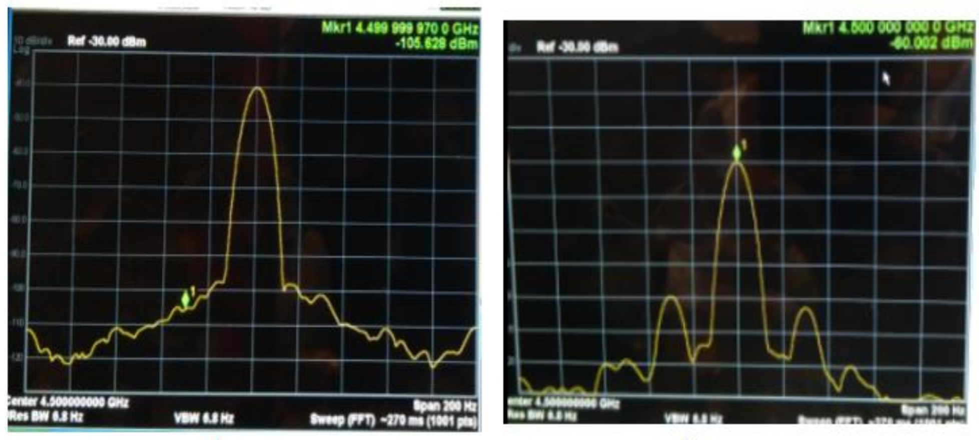

a) b)

Figure 5.7. The spectrum of the received signal at the spectrum analyzer a) without MSC circuit and b) with MSC circuit. With the utilization of MSC circuit, the main signal is suppressed by approximately 20 dB and in the spectrum analyzer the Doppler signal become visible.

-103 dBm (without MSC circuit) to -114 dBm (when MSC circuit is utilized), because at the Doppler frequency both Doppler signal and the phase noise component exists and the received level in the spectrum analyzer at that frequency is sum of both signals. The MSC circuit enabled cancellation of the main signal component, hence, its phase noise component is reduced and Doppler signal become more visible. Even if the level of the signal at Doppler frequency decreases, the SNR is increased.

The performance of the MSC circuit is tested in detail with the second phantom which contains two tumors. The FUS probe is placed over the large tumor and the spectrum of the received signal is observed for four different cases;

Case I: The MSC circuit is not utilized. The microwave signal is transmitted switching the FUS transducer off.

Case II: The MSC circuit is not utilized. The microwave signal is transmitted switching the FUS transducer on.

Case III: The MSC circuit is utilized. The microwave signal is transmitted switching the FUS transducer off.

Case IV: The MSC circuit is utilized. The microwave signal is transmitted switching the FUS transducer on.

The spectrum of the received signals for cases I to IV are presented in Fig. 5.9 and Fig. 5.10, respectively. The amplitude levels of the main signal and the Doppler signal are tabulated in Table II. Comparing the signal levels at ω_m for cases I and III, it is observed that the main signal is suppressed by 33.43 dB, which includes both the insertion loss of the MSC circuit and the effect of signal subtraction. As the insertion loss of the MSC circuit is 0.2 dB, the effective suppression rate is 33.23. dB. For the cases I and III, the signal level at the Doppler frequency $(\omega_m - \Delta\omega)$ shows the phase noise level of the transmitted signal coupled to the receiving antenna. SNR can be calculated from the difference between the signal levels at the Doppler frequency for the cases when the FUS transducer is on and off. Without the MSC circuit (case I and II), SNR is 6.66 dB. Using the MSC circuit (case III and IV), SNR increases to 23.59 dB showing an improvement of 16.93 dB.

5.3.1 2D Scan results

The lateral 2D image of second phantom (containing two tumors) is obtained with a spectrum analyzer both with and without main signal cancellation network with same experimental settings as in the 1D scan (Fig. 5.11). The resultant image is shown in Fig. 5.12. When the scan is performed without the MSC circuit, the received Doppler signal is buried under the phase noise in all positions of the FUS probe and the tumors could not be detected (Fig. 5.12a). When The MSC circuit applied to the HMMDI setup, even though the position of the larger tumor phantom is shifted in the image,

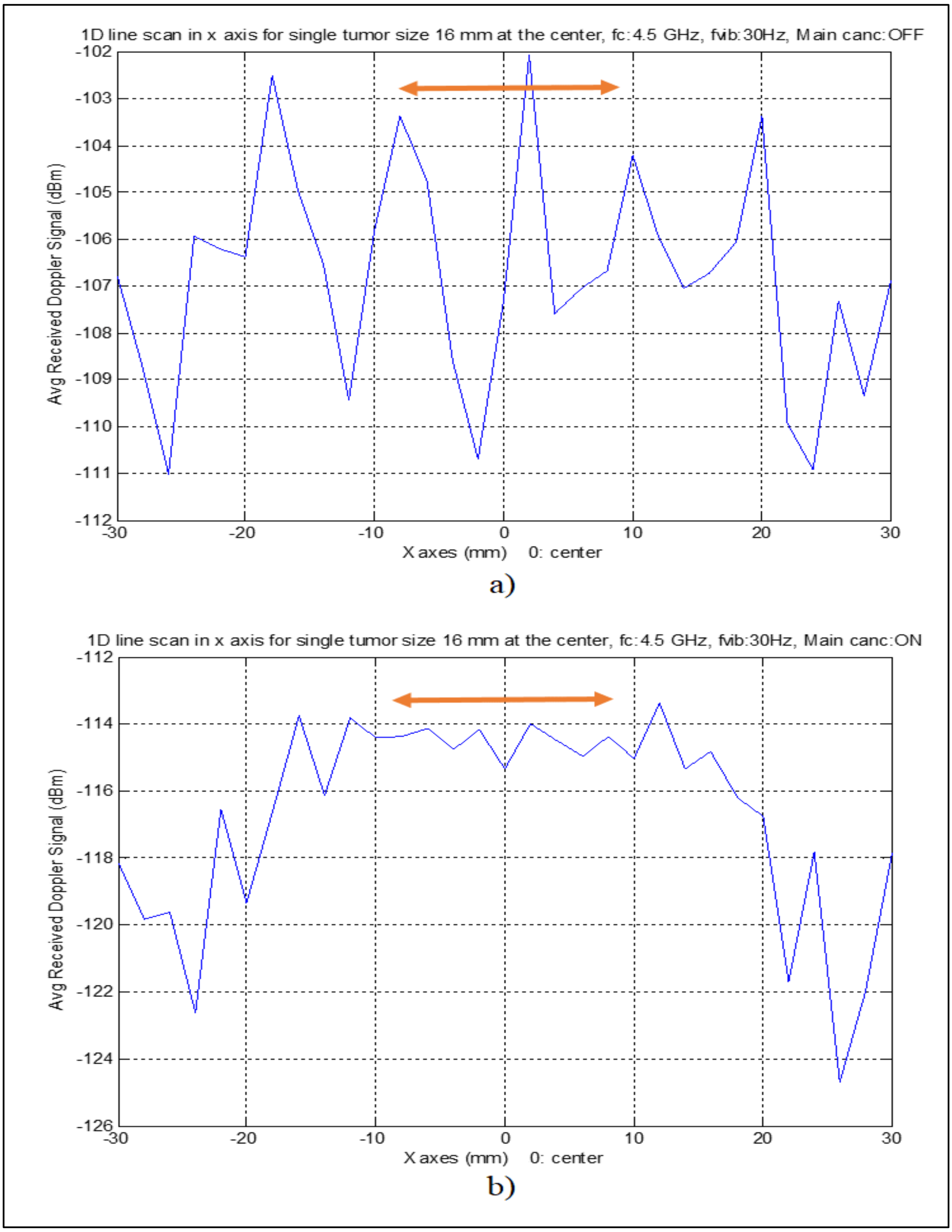

Figure 5.8. 1D line scan in x axis for cylindrical tumor inside a homogeneous fat phantom a) without MSC circuit and b) with MSC circuit. The arrow represents the tumor.

Table 5.3 The amplitude levels of the main signal and the Doppler signal for Cases I to IV

	Signal level at ω_m (dBm)	Signal level at $\omega_m - \Delta\omega$ (dBm)
Case-I	-36.261	-101.918
Case-II	-36.539	-95.261
Case-III	-69.693	-129.449
Case-IV	-70.239	-105.859

the inclusions can be distinguished (Fig. 5.12b). The Doppler signal level is larger around the center of the phantom. The reason of this may be the lower vibration amplitude at the tumor center due to relatively large volume of this inclusion.

In order to see the effect of the tumor placement, the phantom was rotated by 30 degrees in the axial direction from its center and the scan was repeated (Fig. 5.13). The effect of the rotation can be seen in Fig. 5.14. The rotation of the small inclusion is more pronounced than the rotation of the large inclusion.

5.4 Conclusion

Previous experimental studies on the HMMDI method suffered from phase noise of the transmitter and the high direct coupling between antennas [49], [52]. Imaging was limited to certain microwave and vibration frequencies. In this study, a main signal cancellation circuit was designed and implemented to eliminate the effect of phase noise and decrease the level of the coupled transmit signal and increase the SNR of Doppler signal component. The MSC circuit yielded more than 30 dB suppression of the coupled transmit signal, resulting in a highly improved SNR (>15

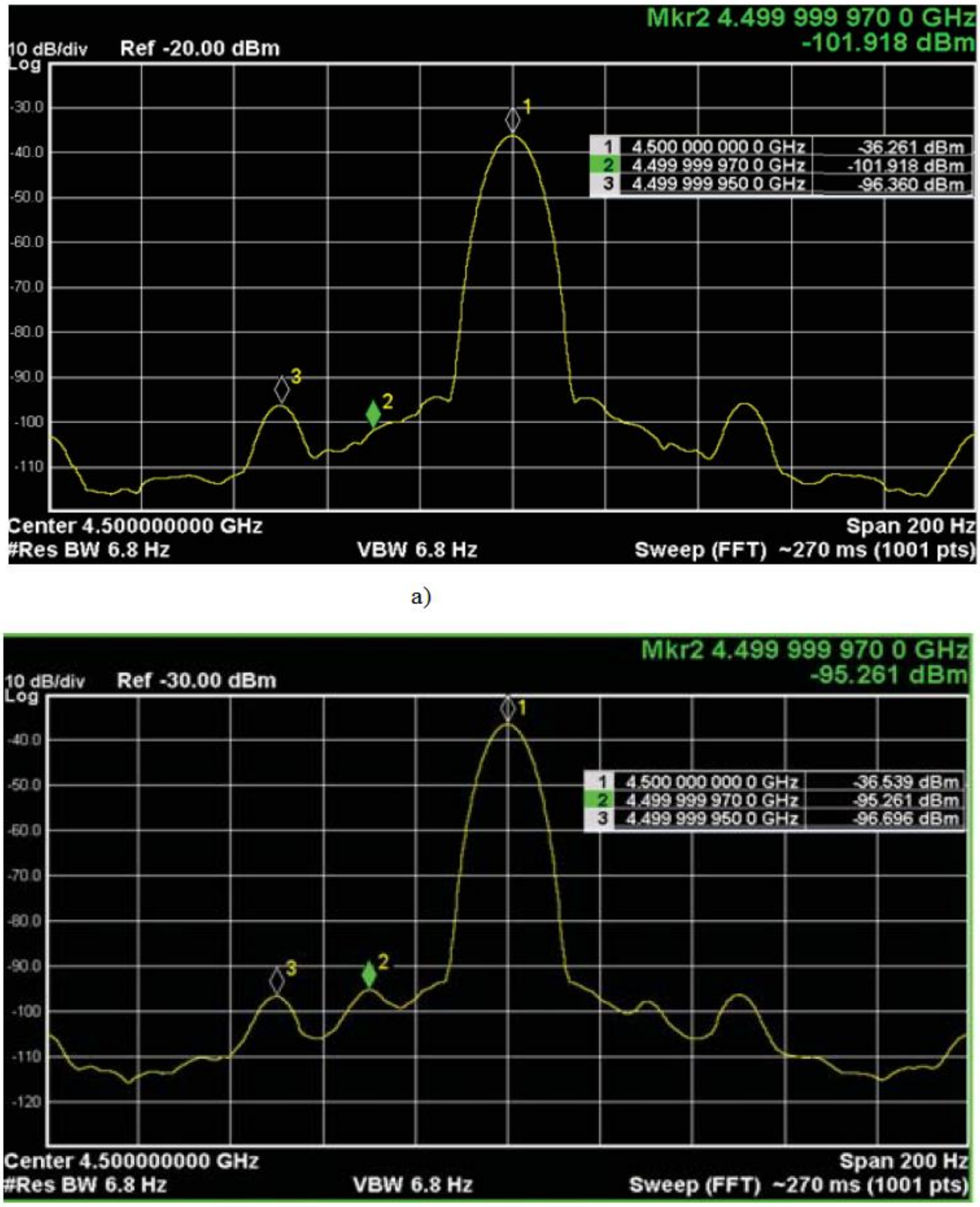

1	4.500 000 000 0 GHz	-36.261 dBm
2	4.499 999 970 0 GHz	-101.918 dBm
3	4.499 999 950 0 GHz	-96.360 dBm

a)

1	4.500 000 000 0 GHz	-36.539 dBm
2	4.499 999 970 0 GHz	-95.261 dBm
3	4.499 999 950 0 GHz	-96.696 dBm

b)

Figure 5.9. The spectrum of the received signal without main signal cancellation circuit: a) FUS transducer is OFF, b) FUS transducer is ON. ωm=4.5 GHz, $\Delta\omega$=30 Hz. Marker 1, 2, and 3 are located at the main signal frequency ωm, Doppler signal frequency $\omega m - \Delta\omega$ and the 50 Hz line frequency, respectively.

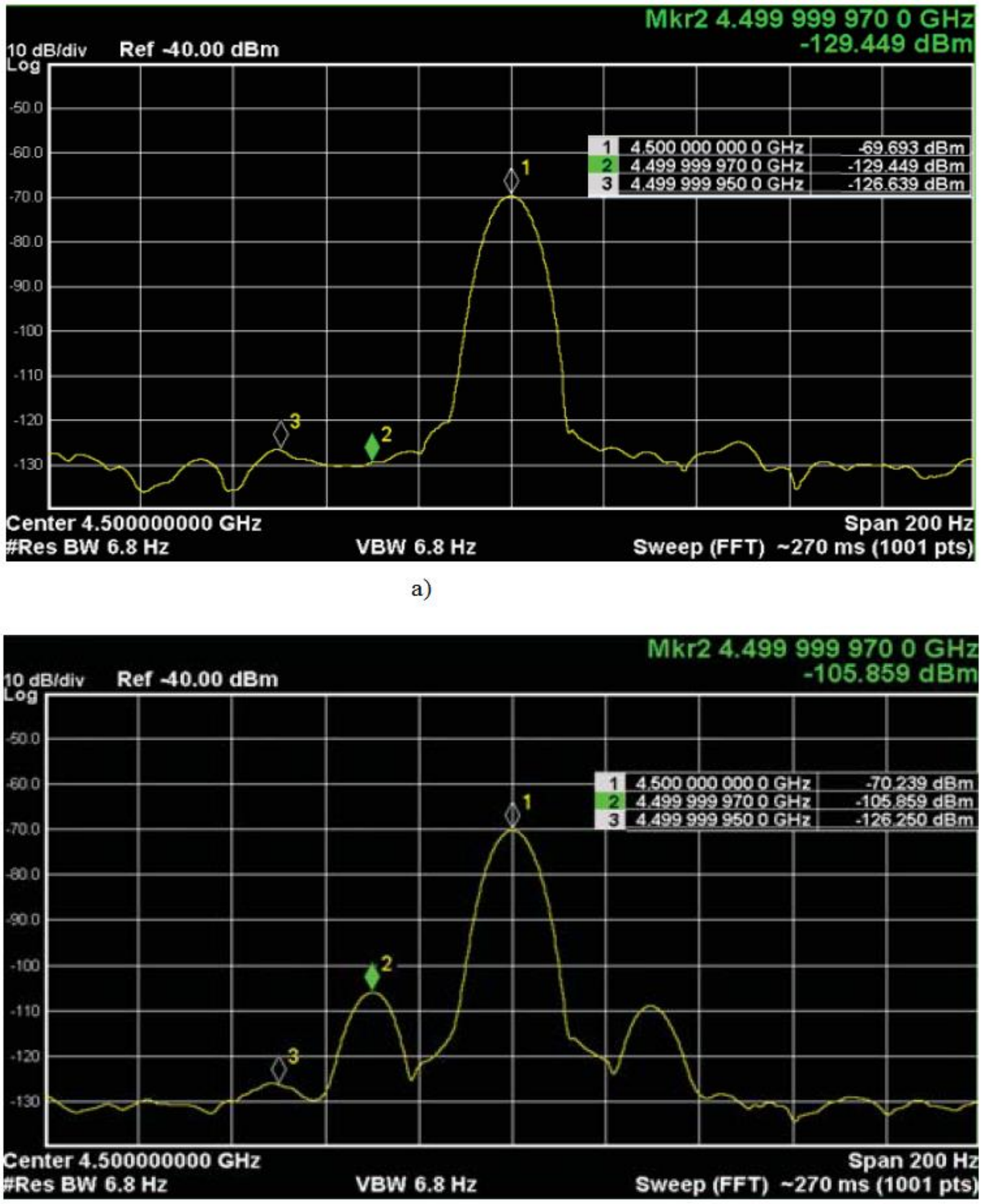

a)

b)

Figure 5.10. The spectrum of the received signal with main signal cancellation circuit: a) FUS transducer is OFF, b) FUS transducer is ON. ωm=4.5 GHz, $\Delta\omega$=30 Hz. Marker 1, 2, and 3 are located at the main signal frequency ωm, Doppler signal frequency $\omega m - \Delta\omega$ and the 50 Hz line frequency, respectively.

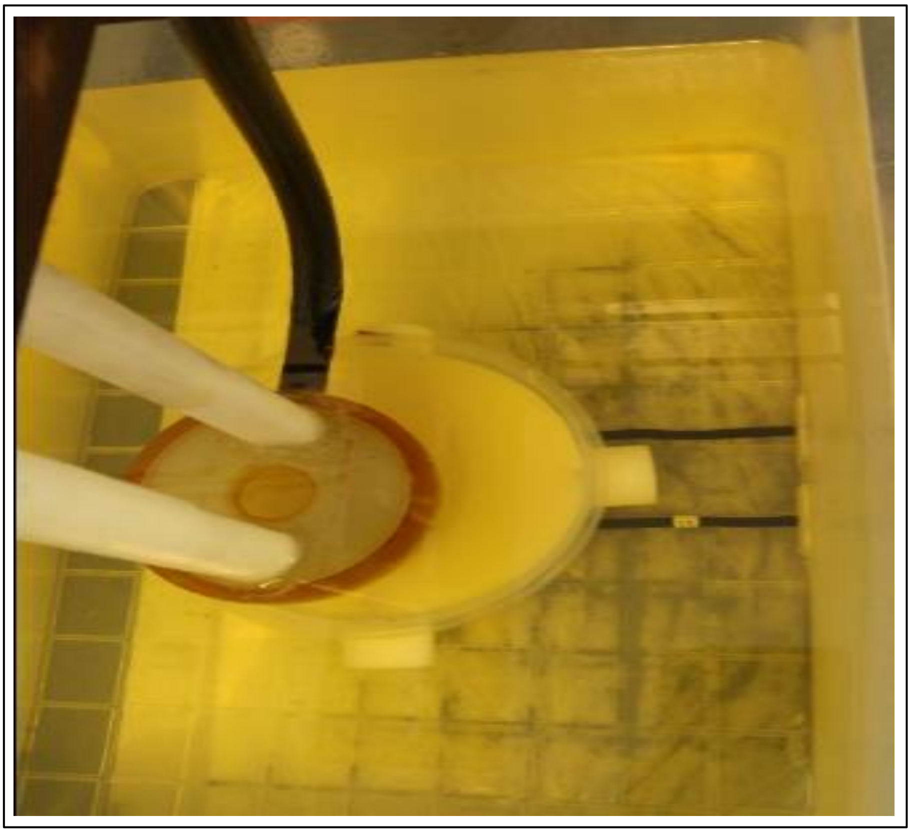

Figure 5.11. Experimental 2D scan of the breast phantom containing two cylindrical homogeneous tumor phantoms of size 15 mm (diameter) x 9 mm (height) and 7 mm (diameter) x 9 mm (height) with about 20 mm separation measured from their edges are placed on a 30 mm height x 11 cm diameter breast fat phantom

dB) of the Doppler component. Breast phantoms containing one and two hard inclusions inside a breast fat phantom, which were initially buried inside the phase noise of the coupled signal, were detected in the HMMDI images. Implementation of MSC circuit enabled the use of any microwave frequency for the HMMDI experiments.

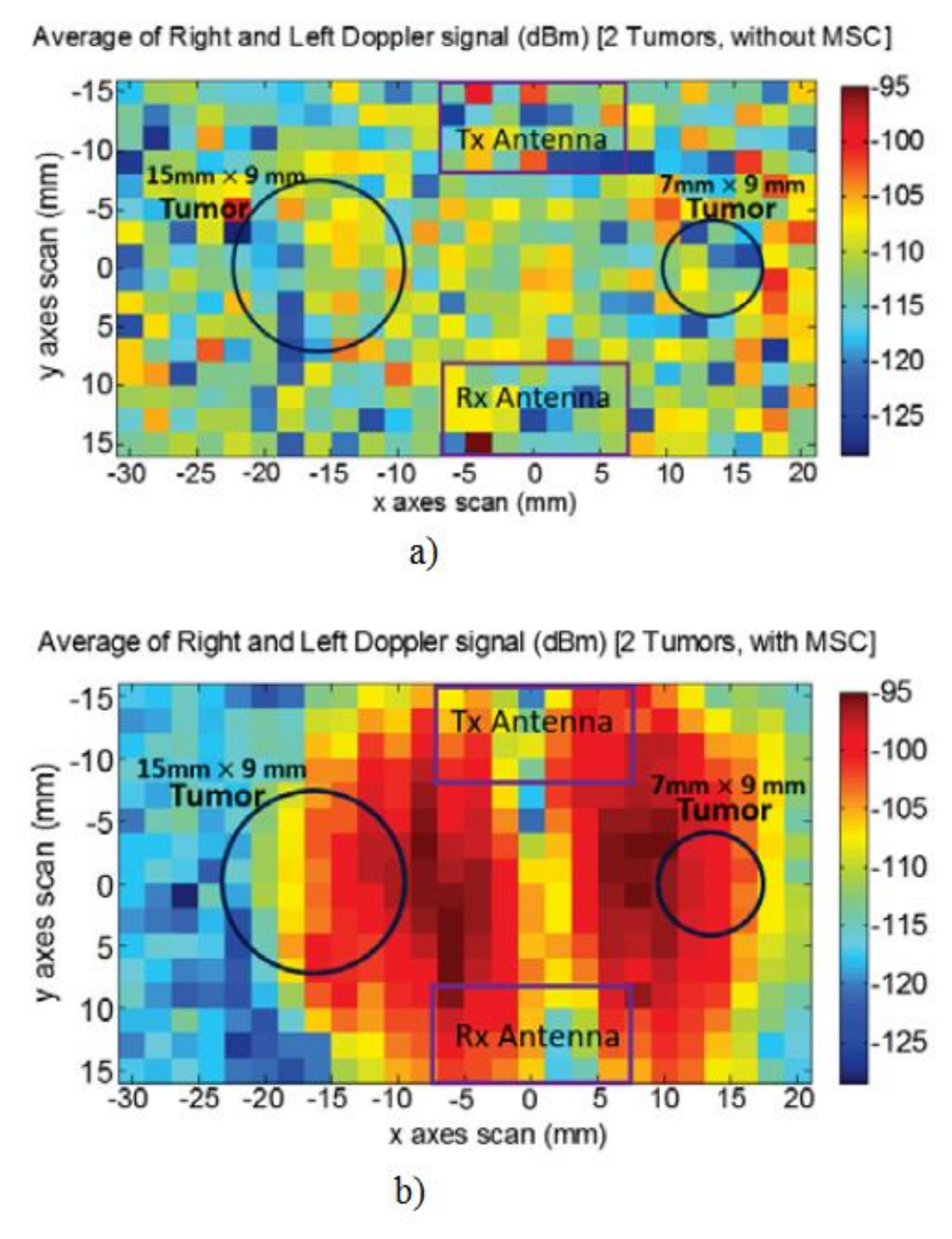

Figure 5.12. 2D imaging of the breast phantom with main signal cancellation circuit for ωm = 4.5 GHz and $\Delta\omega$ =30 Hz. Placement of the antennas and the tumor phantoms are shown on the plot.

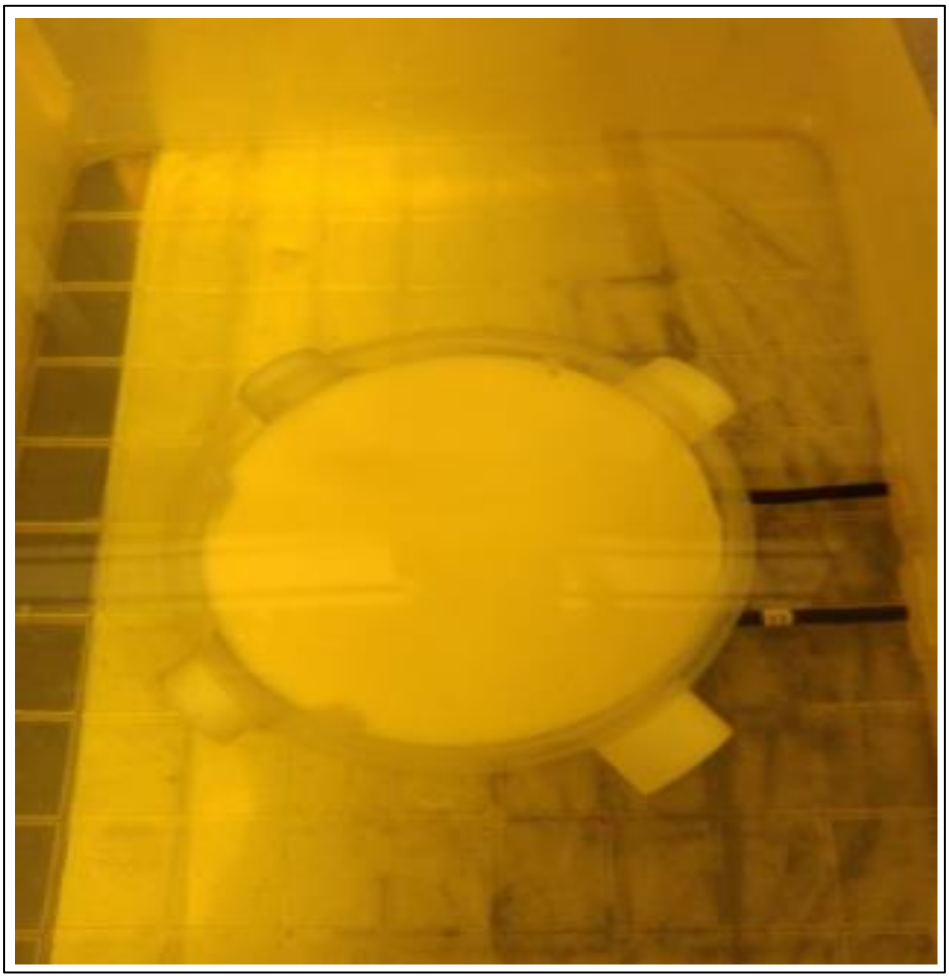

Figure 5.13. Experimental 2D scan of the breast phantom in shown in Fig 5.11 rotated by 30 degrees

There were some limitations of the utilized circuitry in this study. The phase shifter and the attenuator were 6-bit, limiting the phase resolution to 5.625°, and attenuation resolution to 0.5 dB. Moreover, due to physical non idealities, the phase shifter can yield phase error as function of the operating frequency. The circuit can be improved using higher resolution digital or analog phase shifters and attenuators. As the amplitude and phase of the coupled main signal component depend on the dielectric

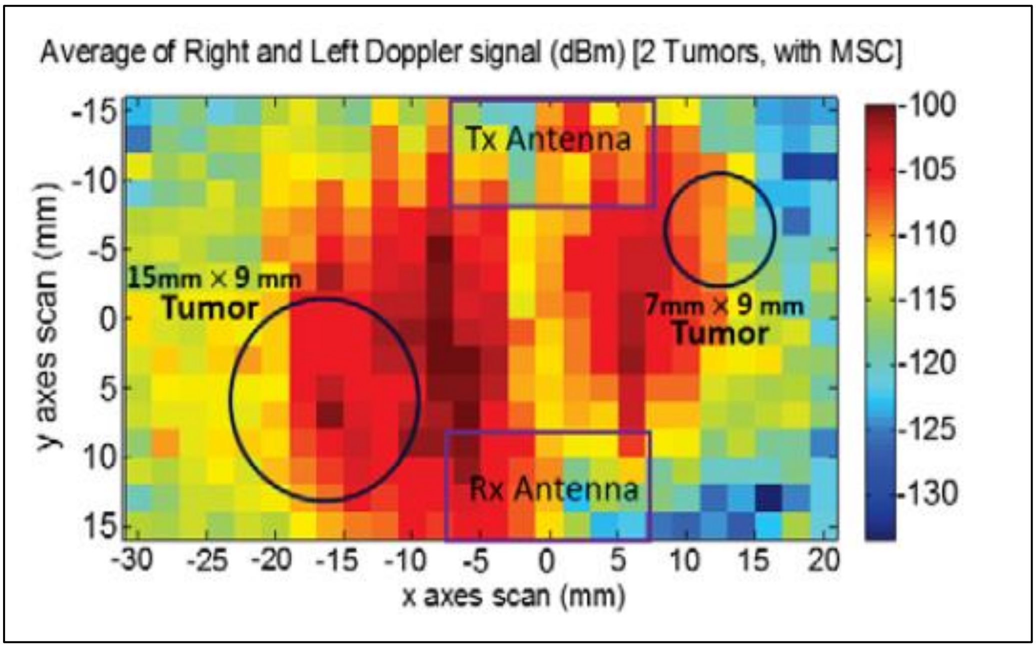

Figure 5.14. 2D HMMDI image of the fat phantom rotated by 30◦ in axial direction with HMMDI with main signal cancellation circuit for ωm = 4.5 GHz and $\Delta\omega$ =30 Hz.

distribution of the medium, the phase shifter and the attenuator should be adjusted each time the object is changed. This can be quickly done prior to a raster scan.

CHAPTER 6

CONCLUSION AND FUTURE WORK

Microwave imaging methods suffers from low dielectric contrast between the breast tissues while detecting the malign tissue inside a low adipose (fibro-glandular) tissue [92]. On the other hand, the HMMDI method succeeded in detection of tumor inside a fibro glandular tissue in phantom experiments by making use of the mechanical properties of the tissues as well as their dielectric properties [50]. Since HMMDI is a hybrid method, the received Doppler signal level depends on the vibration frequency, and dielectric and elastic properties of the tissues. Even though, the level of Doppler signal is higher for low vibration frequencies, due to large vibration volume at low vibration frequencies, the HMMDI image of tumors can appear larger than their original sizes.

The simulation of HMMDI was implemented as sequential FDTD simulations for acoustic, mechanical and electromagnetic problems of HMMDI [49]. The electromagnetic simulation is based on the volume equivalence principle; as a result, the simulation is repeated for original and equivalent models. Doppler signal is calculated from three consecutive electromagnetic simulations for time instants at i) maximum displacement ii) minimum displacement and iii) no displacement.

In this study, the effect of unintended vibrations of the neighboring tissues at low frequencies was studied with the FDTD code implemented in [50] for a tumor inside a fat phantom. The position of the FUS probe and antennas were fixed and the position of tumor was over staggered grids on principle 3D planes. However, the simulation time elapsed for a single tumor position was 122 minutes, as a result, in the simulation the large grid step size was chosen. The grid step sizes in lateral and axial axes were such as 3 mm and 5 mm, respectively. In the lateral (xy) plane, 10 dB decrease in the received Doppler signal can be observed within a circle of 3 mm radius around the focus. These results show that resolutions on the order of millimeters can be achieved with the HMMDI method while detecting a tumor in a high adipose (fat) breast tissue.

Considering the elapsed time for the simulation of the forward EM problem of HMMDI via FDTD code, FDTD based simulation was impractical to study the effect of contrasts in dielectric and elastic properties of the tumor for different positions. In the realms of this study, a fast EM simulation method based on the DDA was implemented. Since the DDA method can handle scattering problems from arbitrarily shaped geometries, it also is suitable for computing the scattered electric fields from vibrating (shape deformed) objects The simulation results of both FDTD and proposed method were compared. The results were in high agreement. The DDA based method decreased the simulation time by a factor of 146 compared to the FDTD method. Fast EM simulations enabled us to investigate the HMMDI imaging as a function of tumor sizes. The HMMDI scan simulation of a tumor in a homogeneous breast model was carried out for different tumor sizes; 27 mm^3 and 216 mm^3. The maximum level of received Doppler signal was higher for the 27mm^3 case. However, the rate of decrease of the Doppler signal, as focus of the FUS probe moves away from the edges of the tumor, showed similar behaviors.

Fast EM simulations enabled the investigation of the Doppler signal variation as a function of tumor position for different dielectric and elastic contrast values, as well as different vibration frequencies. The simulation results show that the received Doppler signal level was maximum for vibration frequencies between 25 Hz to 45 Hz. The received signal level decreased with frequency beyond 45 Hz vibration frequency. Rate of decrease in the Doppler signal depended on both vibration frequency and elasticity contrast. These results suggest that it may be possible to decide on relative elasticity of a stiff inclusion inside normal breast tissue using a multi-frequency scan. We also observed that when either of dielectric or elastic contrast was changed by the same amount, the effect of dielectric contrast was more prominent compared to elastic contrast.

The results also show that below 25 Hz, the received Doppler signal decreases with decreasing frequency, although maximum displacement gets higher. The reason of this can be hypothesized as follows: In the low frequency regime, the acoustic radiation force vibrates the whole inclusion without any shape deformation and only position shift is observed. As a result, the inter-element distances between dipoles does not change significantly at maximum and minimum displacement instants. On the other hand, as frequency increases, the DRW gets smaller enabling the shape deformations on the inclusion. These deformations result in higher phase difference on the scattered signal between the maximum and minimum displacement instants, compared to the case of vibration with no shape deformation.

These results suggest that there are three regimes for the level of the received HMMDI signal as a function of vibration frequency: i) Full vibration with no shape deformation, ii) full vibration with shape deformation, and iii) partial vibration. In the first regime, the signal increases up to some vibration frequency point depending on the size of the inclusion with respect to the DRW of the acoustic radiation force. In the second regime, the signal decreases with frequency because of the lower displacement amplitude. In the third regime, the signal level decreases with a higher rate than the one in the second regime. As the transition frequencies between the regimes depend on the size of the inclusion, it may be possible to estimate inclusion size using these transition points.

Increasing the dielectric and elastic contrast changes the HMMDI signal level. When the (tumor) inclusion was 50% stiffer than normal breast tissue, the received Doppler signal increased by about 3.5 dB and 5.1 dB when their dielectric contrast was increased from 1.17 to 2.6 and 3.75, respectively. A nearly constant difference was observed for all vibration frequencies. On the other hand, change in the elasticity contrast (for constant dielectric contrast) varied as a function of vibration frequency, suggesting the use of received signal behavior as a function of frequency for elasticity contrast estimation.

In the HMMDI method, displacements away from the focal region due to shear wave propagation may contribute to the received Doppler signal level as clutter. This effect was observed experimentally as image artifacts [52] especially for relatively low vibration frequencies (<35 Hz), where shear wavelength and DRW are relatively large. The contribution of the vibration of neighboring tissues on the received Doppler signal level was analyzed by sweeping the inclusion away from the focal region along axial and lateral axes. In Chapter 4, it is observed that the main parameter affecting the level of clutter from neighboring tissues is the vibration frequency. DRW depends on the vibration frequency, and wide DRW results deteriorated image resolution. For example, at 15 Hz vibration frequency, if the inclusion is displaced by 8 mm away from the focal region axially, the received Doppler signal level decrease by 5 dB. On the other hand, the signal decrease is about 20 dB at 85 Hz.

For the axial and lateral scans, the received signal level decreased with increasing dielectric contrast, or with decreasing elastic contrast. The effect of elastic contrast was more dominant compared to the dielectric contrast. Sidelobes were observed in the received signal level as the inclusion was scanned. The position of the sidelobe moves closer to the focus as vibration frequency increases, suggesting that this effect is caused by the shear wave propagation in the medium.

In the previous experimental studies on the HMMDI method, imaging was limited to certain microwave and vibration frequencies due to low SNR caused by the phase noise of the transmitter and the high direct coupling between antennas [52]. In this study, a main signal cancellation circuit was designed and implemented to eliminate the effect of phase noise, decrease the level of the coupled transmit signal, and increase the SNR of Doppler signal component. The MSC circuit enhanced the SNR more than 15 dB by the virtue of suppression of the coupled transmit signal more than 30 dB. Breast phantoms containing one and two hard inclusions inside a breast fat phantom, which could not be imaged in the previous experimental studies due to low SNR [52], were detected in the HMMDI images with the MSC circuit. Hence, implementation of MSC circuit enabled the use of any microwave frequency for the HMMDI experiments.

The performance of HMMDI image can be further ameliorated with the future studies such as:

- The advantage of the fast convergence of DDA may fail depending on the shape of the tumor. A new numerical method can be investigated for enhancing the convergence of DDA algorithm for solving porous or multi-tumor detection in a homogeneous breast tissue.
- The behavior of elastic contrast between tumor and breast phantom as a function of vibration frequency is non-linear. The effect of elastic contrast as function of vibration frequency can be studied for different tumor sizes as well.
- The axial half-power acoustic intensity beam-width of the FUS Probe determines the resolution of the HMMDI image. An alternative FUS Probe or ultrasound transducer array can be implemented for better axial resolution.
- The DRW can be studied for different tumor sizes
- The receiving antenna can be replaced with phased array antennas so that the beam of the receiver antenna array can be steered to specific regions
- The performance of the main signal cancellation circuit on the HMMDI can be investigated with time domain measurements. With the time domain set-up of HMMDI, less number of averaging is adequate for Doppler signal detection

A new reconstruction algorithm can be developed via utilizing the level of the Doppler signal for various vibration frequencies.

REFERENCES

1) G. World Health Organisation, "Breast Cancer Fact Sheet " http://globocan.iarc.fr/Pages/fact_sheets_cancer.aspx. 2019 *[Accessed on : May.12, 2021]*

2) S. J. Nass, I. E. Henderson, LC. Lashof, "Mammography and Beyond: Developing Technologies for the Early Detection of Breast Cancer", *National Research Council*, 2001

3) E. C. Fear and M. A. Stuchly, “Microwave detection of breast cancer,” *IEEE Trans. Microw. Theory Techn.,* vol. 48, no. 11, pp. 1854–1863, Nov. 2000.

4) E. J. Bond, X. Li, S. C. Hagness, and B. D. Van Veen, “Microwave imaging via space-time beamforming for early detection of breast cancer,” *IEEE Trans. Antennas Propag.*, vol. 51, no. 8, pp. 1690–1705, Aug. 2003.

5) P. M. Meaney et al., “Initial clinical experience with microwave breast imaging in women with normal mammography,” *Acad. Radiol.*, vol. 14,no. 2, pp. 207–218, 2007.

6) C. Yu et al., “Active microwave imaging II: 3-D system prototype and image reconstruction from experimental data,” *IEEE Trans. Microw. Theory Techn*., vol. 56, no. 4, pp. 991-1000, April 2008

7) N. K. Nikolova, “Microwave near-field imaging of human tissue and its applications to breast cancer detection,” *IEEE Microw. Mag.*, vol. 12,no. 7, pp. 78–94, Dec. 2011.

8) T. M. Grzegorczyk et al., “Fast 3-d tomographic microwave imaging for breast cancer detection,” *IEEE Trans. Med. Imag*., vol. 31, no. 8, pp. 1584–1592, Aug. 2012.

9) E. C. Fear, J. Bourqui, C. Curtis, D. Mew, B. Docktor, and C. Romano, “Microwave breast imaging with a monostatic radar-based system: A study of application to patients*,” IEEE Trans. Microw. Theory Techn*., vol. 61, no. 5, pp. 2119–2128, May 2013.

10) T. U. Gürbüz, B. Aslanyürek, A. Yapar, H. ¸ Sahintürk, and I. Akduman, “A nonlinear microwave breast cancer imaging approach through realistic body–breast modeling,” *IEEE Trans. Antennas Propag.,* vol. 62,no. 5, pp. 2596–2605, May 2014.

11) T. J. Colgan, S. C. Hagness and B. D. Van Veen, "A 3-D Level Set Method for Microwave Breast Imaging," in *IEEE Transactions on Biomedical Engineering*, vol. 62, no. 10, pp. 2526-2534, Oct. 2015.

12) R. O. Mays, N. Behdad and S. C. Hagness, "Array Sensitivity for Model-Based Microwave Breast Imaging," in *IEEE Transactions on Antennas and Propagation*, vol. 65, no. 6, pp. 2958-2965, June 2017.

13) F. Yang et al., “A large-scale clinical trial of radar-based microwave breast imaging for asian women: Phase I,” in *Proc. IEEE Int. Symp. Antennas Propag. USNC/URSI Nat. Radio Sci. Meeting,* Jul. 2017, pp. 781–783.

14) S. Di Meo, et al, “Experimental Validation of the Dielectric Permittivity of Breast Cancer Tissues up to 50 GHz,” IEEE MTT-S International Microwave Workshop Series-Advanced Materials and Processes *(IMWS-AMP 2017),* Pavia, Italy, Sept. 20-22, 2017

15) A. Martellosio, et al, “Dielectric Properties Characterization from 0.5 to 50 GHz of Breast Cancer Tissues,” *IEEE Trans. Microw. Theory Techn*., Vol. 65, No. 3, pp. 998-1011, March 2017

16) S. Di Meo, et al, “Dielectric properties of breast tissues: Experimental results up to 50 GHz,” 12th European Conference on Antennas and Propagation *(EuCAP 2018),* London, UK, April 9-13, 2018

17) M. Lazebnik et al., “A large-scale study of the ultrawideband microwave dielectric properties of normal, benign and malignant breast tissues obtained from cancer surgeries,” *Phys. Med. Biol.,* vol. 52, no. 20, pp. 6093–6115, 2007.

18) M. Lazebnik et al., “A large-scale study of the ultrawideband microwave dielectric properties of normal breast tissue obtained from reduction surgeries,” *Phys. Med. Biol*., vol. 52, no. 20, pp. 2637–2656, 2007.

19) S. Di Meo, G. Matrone, and M. Pasian, “Experimental Validation on Tissue-Mimicking Phantoms of Millimeter-Wave Imaging for Breast Cancer Detection”, *Appl. Sci.*,vol. 11, pp. 432, 2021

20) S. Di Meo, et al, “Correlation Between Dielectric Properties and Women Age for Breast Cancer Detection at 30 GHz,” *2018 IEEE International Microwave Biomedical Conference (IMBioC),* Philadelphia, PA, USA, June 14-15, 2018

21) J. I. Lopez et al., “In situ force mapping of mammary gland transformation” *Integr Biol.*; vol.9, no.3, pp. 910-21, Sep. 2011

22) A. P. Sarvazyan, O. V. Rudenko, S. D. Swanson, J. B. Fowlkes, and S. Y. Emelianov, “Shear wave elasticity imaging: A new ultrasonic technology of medical diagnostics,” *Ultrasound Med. Biol.*, vol. 24, no. 9, pp. 1419–1435, Nov. 1998.

23) M. Fatemi and J. F. Greenleaf, “Vibro-acoustography: An imaging modality based on ultrasound-stimulated acoustic emission,” *Proc. Nat.Acad. Sci. USA*, vol. 96, no. 12, pp. 6603–6608, 1999.

24) E. E. Konofagou and K. Hynynen, “Localized harmonic motion imaging: Theory, simulations and experiments,” *Ultrasound Med. Biol.*, vol. 29,no. 10, pp. 1405–1413, Oct. 2003.

25) J. Vappou, C. Maleke, and E. E. Konofagou, “Quantitative viscoelastic parameters measured by harmonic motion imaging,” *Phys. Med. Biol.*,vol. 54, no. 11, pp. 3579–3595, Jun. 2009.

26) L. Wang, “Acoustic Radiation Force Based Ultrasound Elasticity Imaging for Biomedical Applications.” *Sensors (Basel, Switzerland)*, vol. 18,7 2252. 12 Jul. 2018,

27) J. Buijs, H. Hansen, R. Lopata, C. M. Corte “ Predicting target displacements using ultrasound elastography and finite element modeling”, *IEEE Trans Biomed Eng.*, vol. 58, no. 11, pp.3143–3155, 2011

28) N.G. Ramião et al “Biomechanical properties of breast tissue, a state-of-the-art review”. *Biomech Model Mechanobiol*. Vol.15, no.5, pp.1307-1323, Oct. 2016

29) T. Krouskop et al, “Elastic moduli of breast and prostate tissues under compression”, *Ultrasound Imaging*, vol. 20, pp. 260–274,1998

30) P. S. Wellman, R. D. Howe, E. Dalton, and K. A. Kern, “Breast Tissue Stiffness in Compression is Correlated to Histological Diagnosis,” pp. 1–15, 1999

31) A. Samani et al, “An inverse problem solution for measuring the elastic modulus of intact ex vivo breast tissue tumors,” *Physics in Med. and Biol.*, Vol. 52, No.5, pp. 1247-60, April 2007.

32) A. Sarvazyan, et al, "Biophysical bases of elasticity imaging," *Acoustical Imaging*, vol. 21, pp.223-241, 1995..

33) T. Matsumura T, T. Umemoto, Y. Fujihara, E. Ueno, M Yamakawa, T. Shiina, T. Mitake “Measurement of elastic property of breast tissue for elasticity imaging”, *in: Proceedings of IEEE Ultrasonic Symposium*, pp 1451–1454, 2009

34) T. Umemoto, et al, “Ex Vivo and In Vivo Assessment of the Non-linearity of Elasticity Properties of Breast Tissues for Quantitative Strain Elastography,” *Ultrasound in Medicine and Biology*, vol.40, no. 8, pp. 1755-68, Aug., 2014.

35) S. Kruse et al, “Tissue characterization using magnetic resonance elastography: preliminary results”, *Phys Med Bio*l., vol.45, pp.1579–1590, 2000

36) R. Sinkus et al, “Viscoelastic shear properties of in vivo breast lesions measured by MR elastography”, *Magn Reson Imaging*, vol 23, pp. 159–165, 2005

37) A. L. McKnight et al, “MR elastography of breast cancer: preliminary results” *Am J Roentgenol* , vol. 178, pp.1411–1417, 2002

38) Lawrence A, Muthupillai R, Rossman P, Smith J, Manduca A, Ehman R “Magnetic resonance elastography of the breast: preliminary experience.” In: Proceedings of the international society for magnetic resonance in medicine. *International Society for Magnetic Resonance in Medicine (ISMRM’98)*, Sydney, Australia, 1998

39) J. Cheng et al. “Non compressive MR elastography of breasts”. Proceedings of the international society for magnetic resonance in medicine. *International Society for Magnetic Resonance in Medicine (ISMRM’13)*,, Salt Lake City, USA,2013

40) T. Xydeas et al, “Magnetic resonance elastography of the breast.” *Invest Radiol.*, vol. 40, pp.412–420, 2005

41) A.Srivastava et al “Determination of elastic properties of resected human breast tissue samples using optical coherence tomographic elastography”, *Strain*, vol. 47, pp.75–87, 2011

42) J. Lorenzen et al, “Menstrual-cycle dependence of breast parenchyma elasticity: estimation with magnetic resonance elastography of breast tissue during the menstrual cycle.” *Invest Radiol.*, vol.38, no:4, pp. 236–240, 2003

43) A. Abbosh, “Early breast cancer detection using hybrid imaging modality,” in Proc. *IEEE Antennas Propag. Soc. Int. Symp., Charleston,* SC,USA, pp. 1–4, Jun. 2009

44) M. Zhao, J. D. Shea, S. C. Hagness, D. W. van der Weide, B. D. Van Veen, and T. Varghese, “Numerical study of microwave scattering in breast tissue via coupled dielectric and elastic contrasts*,” IEEE Antennas Wireless Propag. Lett.*, vol. 7, pp. 247–250, 2008.

45) D. E. Lawrence and K. Sarabandi, “Acoustic and electromagnetic wave interaction: Analytical formulation for acousto-electromagnetic scattering behavior of a dielectric cylinder,” *IEEE Trans. Antennas Propag.*, vol. 49, no. 10, pp. 1382–1392, Oct. 2001.

46) K. Sarabandi and D. E. Lawrence, “Acoustic and electromagnetic wave interaction: Estimation of Doppler spectrum from an acoustically vibrated metallic circular cylinder,” *IEEE Trans. Antennas Propag.*, vol. 51, no. 7, pp. 1499–1507, Jul. 2003.

47) A. M. Buerkle and K. Sarabandi, “Analysis of acousto-electromagnetic wave interaction using sheet boundary conditions and the finite difference time-domain method,” *IEEE Trans. Antennas Propag.*, vol. 55, no. 7, pp. 1991–1998, Jul. 2007.

48) C. B. Top and N. Gencer, “Harmonic Motion Microwave Doppler Imaging : A Simulation Study Using a Simple Breast Model,” *IEEE Trans. Med. Imag.*, vol.33, no.2, pp.290-300, Feb. 2014

49) Can Barış Top, "Harmonic Motion Microwave Doppler Imaging," *PhD Thesis*, Sep. 2013, METU

50) C. B. Top, A.K. Tafreshi, N. Gencer, "Microwave Sensing of Acoustically Induced Local Harmonic Motion: Experimental and Simulation Studies on Breast Tumor Detection," *IEEE Trans.on Microw. Theory and Techn.*, vol. 64, no. 11, pp. 3974-3986, Nov. 2016.

51) Top, C. B., Tafreshi, A. K., Gencer, N., "Harmonic Motion Microwave Doppler Imaging Method for Breast Tumor Detection, " *Engineering in Medicine and Biology Society (EMBC),* 36th Annual International Conference of the IEEE, 2014

52) Azadeh Kamali Tafreshi, "Design and Realization of a Hybrid Medical Imaging System: Harmonic Motion Microwave Doppler Imaging" *PhD Thesis*, Feb. 2016, METU

53) E. M. Purcell and C. R. Pennypacker, "Scattering and adsorption of light by nonspherical dielectric grains," *Astrophys. Jour*, vol. 186, pp. 705–714, Dec. 1973

54) M. A. Yurkin et al. "Accuracy of the discrete dipole approximation for simulation of optical properties of gold nanoparticles," *Jour. of Nanophoton*., vol. 4, no. 1, pp. 1-15, Feb. 2010

55) K. R. Nightingale et al., "On The Feasibility Of Remote Palpation Using Acoustic Radiation Force." *Journ. of the Acous. Soc. of Amer*., vol. 110, no:1, p. 625-634, 2001

56) M. Fatemi and J.F. Greenleaf, "Vibro-Acoustography: An ·Imaging Modality Based On Ultrasound-Stimulated Acoustic Emission". *Proceedings of the National Academy of Sciences of the United States of America*,. vol.96, no:12, pp: 6603-6608, 1999

57) Food Drug Admin., HIFU simulator [Online]. Available: https://www.fda.gov/about-fda/cdrh-offices/hitu-simulator *[Accessed on : July.12, 2021*]

58) J. Virieux, "P-SV wave propagation in heterogeneous media: velocity-stress finite-difference method", *Geophysics*, vol. 51, pp. 889-901,1986

59) K.Yomogida and J. T. Etgen "3-D wave propagation in the Los Angeles Basin for the Whittier-Narrows earthquake," *Bull Seism. Soc. Am.* vol. 83, pp:1325-1344, 1993

60) J. G. Maloney and G. S. Smith, "The efficient modeling of thin material sheets in the finite-difference time-domain (FDTD) method," *IEEE Trans. on Antennas and Propagation,* vol. 40, no: 3, pp, 323-330, 1990.

61) Fikret Tatar, "Three Dimensional Finite Difference Time Domain Simulations On Harmonic Motion Microwave Doppler Imaging Method Using Realistic Tissue Models" *Ms. Thesis*, Sep. 2019

62) B. T. Draine and P. J. Flatau, "Discrete-dipole approximation for scattering calculations", *Journ. of Opt. Soc. Amer*., vol. 11, pp: 1491–1499, 1994

63) S. Hosseinzadegan, A. Fhager, M. Persson and P. M. Meaney, "Application of Two-Dimensional Discrete Dipole Approximation in Simulating Electric

Field of a Microwave Breast Imaging System," *IEEE Journal of Electromagnetics, RF and Microwaves in Medicine and Biology*, vol. 3, no. 2, pp. 80-87, June 2019.

64) S. Hosseinzadegan, A. Fhager, M. Persson, and P. Meaney, "A Discrete Dipole Approximation Solver Based on the COCG-FFT Algorithm and Its Application to Microwave Breast Imaging," *Int. Journ. of Antennas and Propagation*, vol. 2019, Article ID 9014969, 12 pages, 2019.

65) T. C. Bowman, A. Hassan, and M. El-Shenawee, M. "Imaging 2D Breast Cancer Tumor Margin at Terahertz Frequency using Numerical Field Data based on DDSCAT," *Applied Computational Electromagnetics Society Journal*, vol.28, pp:1017-1024, 2013

66) J. McDonald, A. Golden, S.G.Jennings, "OpenDDA: a novel highperformance computational framework for the discrete dipole approximation," *Int Journ.of High Perform Comput* Appl vol.2, pp:42–61, 2013

67) V. L.Y. Loke and M. P. Menguc, "Surface waves and atomic force microscope probe-particle near-field coupling: discrete dipole approximation with surface interaction" *J Opt Soc Am A* ,vol. 27, pp: 2293–2303, 2010

68) M. A Yurkin, and A. G. Hoekstra "The discrete-dipole-approximation code ADDA: Capabilities and known limitations", *Journal of Quantitative Spectroscopy and Radiative Transfer*. 112. 10.1016/j.jqsrt.2011.01.031, 2011

69) E. M. Purcell, C. R. Pennypacker, "Scattering and adsorption of light by nonspherical dielectric grains," *Astrophys J*, vol.186, pp:705–714,1973

70) M. A Yurkin, and A. G. Hoekstra, "The discrete dipole approximation: an overview and recent developments," *J Quant Spectrosc Radiat Transfer* vol.106, pp:558–589, 2007

71) S. Koc, W.C. Chew, "Multilevel fast multipole algorithm for the discrete dipole approximation," *J Electrom Wav Appl*ic , vol.15, pp:1447-1468, 2001

72) J.D. Jackson. "Classical electrodynamics". 3rd ed.. New York: *Wiley*, 1998

73) B. T. Draine and J. Goodman, "Beyond Clausius-Mossotti - Wave propagation on a polarizable point lattice and the discrete dipole approximation," *Astrophy. Jour.*, vol. 405, no. 2, pp.685-697, Mar. 1993

74) R. Barrett, M. Berry, T. F. Chan, J. Demmel , J. Donato, J. Dongarra, V. Eijkhout, R. Pozo, H. A van der Vorst, “Templates for the Solution of Linear Systems: Building Blocks for Iterative Methods”. *SIAM*, 1994.

75) M. A. Yurkin, V. P. Maltsev, A. G. Hoekstra, “The discrete dipole approximation for simulation of light scattering by particles much larger than the wavelength,” *Journ. of Quant Spectrosc Radiat Transf*, doi: 10.1016/j.jqsrt.2007.01.33, 2007

76) Z. H. Fan, D. X. Wang, R.S Chen, E. K. N. Yung, “The application of iterative solvers in discrete dipole approximation method for computing electromagnetic scattering, “*Microwave Opt Tech Lett* vol.48, pp:1741-1746, 2006

77) S. L. Zhang, “GPBi-CG: Generalized product-type methods based on Bi-CG for solving nonsymmetric linear systems”. *SIAM J Sci Comp* vol.18, pp: 537-551, 1997

78) J. I. Goodman , B. T. Draine, P. J. Flatau, “Application of fast-Fourier-transform techniques to the discrete-dipole approximation,” *Opt Lett*, vol.16, pp:1198-1200, 1991

79) B. E. Barrowes, F. L. Teixeira “Fast algorithm for matrix-vector multiply of asymmetric multilevel block-Toeplitz matrices in 3-D scattering,” *Microwave Opt Tech Lett*; vol.31, pp:28-32, 2001

80) J. Rahola, “Solution of dense systems of linear equations in the discrete-dipole approximation,” *SIAM J Sci Comp* ,vol. 17, pp : 78-89, 1996

81) K. Lumme and J.Rahola, “Light-scattering by porous dust particles in the discrete-dipole approximation,” *Astrophys J*; vol.425, pp:653-667, 1994

82) R. T. Compton, Jr., “The admittance of aperture antenna radiating into a lossy media” Ohio State Univ., Antenna Lab., Columbus, OH,1964

83) A. W. Guy, "Electromagnetic Fields and Relative Heating Patterns Due to a Rectangular Aperture Source in Direct Contact with Bilayered Biological Tissue," in *IEEE Transactions on Microwave Theory and Techniques*, vol. 19, no. 2, pp. 214-223, February 1971

84) N. Azman and S. Hamid, “Determining the Time of Flight and Speed of Sound on Different types of Edible Oil” in IOP Conf. Ser.: Mat. Sci. and Eng., 2017, no. 260.

85) R. Chanamai and D. McClements, “Ultrasonic attenuation of edible oils” *Jour. of the Amer. Oil Chem. Soc.*, vol. 75, no. 10, pp. 1447-1448, Oct. 1998

86) A. L. Scherzinger et al., “Assessment of ultrasonic computed tomography in symptomatic breast patients by discriminant analysis,” *Ultrasound Med. Biol.,* vol. 15, pp. 21–28, 1989.

87) A. García-Manso et al.,“Study of the Effect of Breast Tissue Density on Detection of Masses in Mammograms,” *Comp. and Math. Methods in Med.,* vol. 2013, Article ID 213794, 10 pages, 2013.

88) F. O’Hara and G. Moore, “A high performance cw receiver using feedthru nulling,” *Microwave Journal*, vol. 6, no. 9, pp. 63–71, 1963.

89) A. G. S. Beasley, B. J. Reits, and B. As, “Solving the problems of a single antenna frequency modulated cw radar,” *in IEEE International Conference on Radar*, May 1990, pp. 391–395.

90) M. Lazebnik, E. L. Madsen, G. R. Frank, and S. C. Hagness, “Tissue mimicking phantom materials for narrowband and ultrawideband microwave applications,” *Physics in Medicine and Biology*, vol. 50, no. 18, pp. 4245_4258, 2005.

91) E. L. Madsen, G. R. Frank, T. A. Krouskop, T. Varghese, F. Kallel, and J. Ophir, “Tissue-mimicking oil-in-gelatin dispersions for use in heterogeneous elastography phantoms,” *Ultrasonic Imaging*, vol. 25, no. 1, pp. 17-38, 2003

92) D. O’Loughlin, M. O’Halloran, B. M. Moloney, M. Glavin, E. Jones and M. A. Elahi, "Microwave Breast Imaging: Clinical Advances and Remaining Challenges," in *IEEE Transactions on Biomedical Engineering*, vol. 65, no. 11, pp. 2580-2590, Nov. 2018,

CURRICULUM VITAE

PERSONAL INFORMATION

Surname, Name: İrgin, Ümit
Nationality: Turkish (TC)
Date and Place of Birth: 2 July 1985, Kayseri
Phone: +90 312 592 6000
email: e134204@metu.edu.tr

EDUCATION

Degree	**Institution**	**Year of Graduation**
MS	METU Electrical – Electronics Engineering	2009
BS	METU Electrical – Electronics Engineering	2006
High School	Mersin Science High School	2002

WORK EXPERIENCE

Year	**Place**	**Enrollment**
2006-Present	ASELSAN	RF Design Engineer

PUBLICATIONS

Journals

1. U. Irgin, C. B. Top and N. Gençer, "The Effect of Contrasts in Electrical and Mechanical Properties between Breast Tissues on Harmonic Motion Microwave Doppler Imaging Signal," in *IEEE Journal of Electromagnetics, RF and Microwaves in Medicine and Biology*, (Early Access) doi: 10.1109/JERM.2021.3075343.
2. U. Irgin, C. B. Top and N. Gençer, " A Fast Simulation Scheme for the Harmonic Motion Microwave Doppler Imaging Method," in *IEEE Transactions on Microwave Theory and Techniques (Submitted)*

Conference Papers

1. U. İrgin, C. B. Top, A. K. Tafreshi and N. G. Gençer, "Received signal in harmonic motion microwave doppler imaging as a function of tumor position in a 3D scheme," *2017 11th International Symposium on Medical Information and Communication Technology (ISMICT)*, 2017, pp. 86-90, doi: 10.1109/ISMICT.2017.7891774.

2. Ü. İrgin, C. B. Top, D. A. Soydan and N. G. Gençer, "Enhancing the sensitivity of Harmonic Motion Microwave Doppler Imaging using main signal cancellation circuit," *12th European Conference on Antennas and Propagation (EuCAP 2018)*, 2018, pp. 1-5, doi: 10.1049/cp.2018.0503.

3. D. A. Soydan, Ü. İrgin, C. B. Top and N. G. Gençer, "An Improved Receiver for Harmonic Motion Microwave Doppler Imaging," *2020 14th European Conference on Antennas and Propagation (EuCAP)*, 2020, pp. 1-5, doi: 10.23919/EuCAP48036.2020.9136027.

4. A. K. Tafreshi, C. B. Top, U. Irgin, N. G. Gencer, "Harmonic Motion Microwave Doppler Imaging Using scanning Antennas," BioEM 2016, Bioelectromagnetics Society and the European BioElectromagnetics Association,Ghent, Belgium, 2016

GRANTS AND AWARDS

1. **2017:** Best Student Paper Award, in *2017 11th International Symposium on Medical Information and Communication Technology (ISMICT)*, Lisboa, PORTUGAL, 2017

2. **2017**: Best Student Poster Presentation Award, METU EEE, GRADSTAR 2017

3. **2018-2021**: Research Grant and Scholarship: "Enhancement of a System Sensitivity, Reliability and Safety for Harmonic Motion Microwave Doppler Imaging," 117E246 The Scientific and Technological Research Council of Turkey (TÜBİTAK).

4. **2014-2016**: Research Grant and Scholarship: "Development of a Prototype System for Harmonic Motion Microwave Doppler Imaging," 114E036,

Cost Action TD1301, The Scientific and Technological Research Council of Turkey (TÜBİTAK).

5. **2018:** ITC Conference Grant for EuCAP’18, COST Action BM 1309

6. **2016:** ESoA- EurAPP Course fee and accommodation grant for “Microwave Imaging Techniques course”, 6-10 Oct 2016, Taormina, ITALY

7. **2008**: METU Course Performance Award, METU GSNAS (CGPA: 4.00/4.00)